

**ON-CHIP PHENOTYPIC SCREENING AND
CHARACTERIZATION OF C. ELEGANS ENABLED BY
MICROFLUIDICS AND IMAGE ANALYSIS METHODS**

A Dissertation

Presented to

The Academic Faculty

by

Ivan de Carlos Cáceres Mendieta

In Partial Fulfillment

of the Requirements for the Degree

Doctor of Philosophy in the

School of Bioengineering

Georgia Institute of Technology

December 2013

COPYRIGHT 2013 BY IVAN DE CARLOS CÁCERES MENDIETA

**ON-CHIP PHENOTYPIC SCREENING AND
CHARACTERIZATION OF C. ELEGANS ENABLED BY
MICROFLUIDICS AND IMAGE ANALYSIS METHODS**

Approved by:

Dr. Hang Lu, Advisor
School of Chemical & Biomolecular
Engineering
Georgia Institute of Technology

Dr. Xiaoping Hu
School of Biomedical Engineering
Georgia Institute of Technology

Dr. Oliver Brand
School of Electrical and Computer
Engineering
Georgia Institute of Technology

Dr. Todd Strelman
School of Biology
Georgia Institute of Technology

Dr. Robert Butera
School of Electrical and Computer
Engineering
Georgia Institute of Technology

Date Approved: August 20, 2013

To my family. Sin ustedes, no soy nada.

ACKNOWLEDGEMENTS

I'd like to acknowledge my Principal Investigator, Dr. Hang Lu for molding me into a better scientist. The road wasn't an easy one, but I couldn't have made it to this point without her guidance. I know I haven't always been the best graduate student, but despite everything, she stuck by my side and gave me the opportunity to succeed within her lab. I would also like to acknowledge my committee members for their insightful comments and feedback throughout my many years at Georgia Tech, and maybe most of all, for having patience with me.

I have had too much help than I can give credit for while a graduate student. Without my family and friends (both in ATL and TX), I wouldn't have survived the madness that is known as pursuing my PhD. I thank you all immensely. It has been a long journey these past seven years, but with you all by my side I finally have reached the end of what seemed not too long ago, like a never ending tunnel. I love you all more than I can describe in words and share my accomplishment with you. I could not have done this on my own, thank you.

TABLE OF CONTENTS

ACKNOWLEDGEMENTS	IV
LIST OF TABLES.....	IX
LIST OF FIGURES	X
LIST OF SYMBOLS AND ABBREVIATIONS.....	XII
SUMMARY.....	XIII
CHAPTER 1 INTRODUCTION	1
1.1 Thesis objectives.....	1
CHAPTER 2 LITERATURE REVIEW	3
2.1 The model organism <i>C. elegans</i>	3
2.1.1 Standard genetics screening methods of <i>C. elegans</i>	4
2.1.2 <i>C. elegans</i> as a model for neurodegeneration	5
2.2 Microfluidics.....	5
2.2.1 Soft lithography as a tool for biomedical research	6
2.2.2 Microfluidics and <i>C. elegans</i>	7
2.3 Image analysis for biomedical applications.....	8
2.3.1 Segmentation methods.....	9
2.3.2 Morphological processing.....	10
2.3.3 Image analysis and <i>C. elegans</i>	11
CHAPTER 3 LATERALLY ORIENTING <i>C. ELEGANS</i> USING GEOMETRY AT MICROSCALE FOR HIGH-THROUGHPUT VISUAL SCREENS IN NEURODEGENERATION AND NEURONAL DEVELOPMENT STUDIES	13
3.1 Introduction.....	13
3.2 Materials and Methods.....	14
3.2.1 Microfluidic device fabrication and operation.....	14
3.2.2 Orientation Analysis	16
3.2.3 <i>C. elegans</i> culture, mutagenesis, and phenotype scoring.....	17
3.2.4 <i>C. elegans</i> mock screen and egg-laying assay	18
3.3 Results.....	19
3.3.1 Sample loading orientation and device characterization	19

3.3.2	Identification of neurodegenerative and neurodevelopmental mutants using curved channel microfluidic devices.....	22
3.3.3	Phenotype characterization of mutant animals	25
3.4	Discussion.....	29
CHAPTER 4 AUTOMATED SCREENING OF <i>C. ELEGANS</i> NEURODEGENERATION MUTANTS ENABLED BY MICROFLUIDICS AND IMAGE ANALYSIS ALGORITHMS		
4.1	Introduction.....	34
4.2	Materials and methods	36
4.2.1	Microfluidic device fabrication and operation.....	36
4.2.2	<i>C. elegans</i> culture, mutagenesis, and phenotype scoring.....	36
4.2.3	Automated system operation.....	37
4.3	Results and discussion	39
4.3.1	Microfluidic device performance.....	39
4.3.2	Manual screen for suppressor mutants.....	41
4.3.3	Software design and validation.....	43
4.3.4	Automated screen for suppressors of <i>smn-1</i> mutation.....	48
4.4	Conclusions.....	52
CHAPTER 5 HIGH THROUGHPUT CHARACTERIZATION OF SPHERICAL OBJECTS USING MODIFIED GRANULOMETRY ALGORITHM FOR RAPID CHARACTERIZATION OF <i>C. ELEGANS</i> LIPIDS.....		
5.1	Introduction.....	53
5.2	Materials and Methods.....	55
5.2.1	<i>C. elegans</i> culture, mutagenesis, imaging, and manual lipid characterization	55
5.2.2	Synthetic image creation and software validation	56
5.2.3	Analysis of nematode lipid distribution.....	57
5.3	Results and Discussion	61
5.3.1	Software Estimation of Object Population Percentage and Size Validated Using Synthetic and Bead Images	61
5.3.2	Software Characterization of Wild-Type and Lipid Metabolism Mutant Populations Mimics Known Distributions.....	66
5.3.3	Software Method Capable of Characterizing Low Resolution Images for Characterization of Wild-Type and Lipid Mutant Populations.....	71

5.4	Conclusions.....	75
CHAPTER 6 AUTOMATED CHARACTERIZATION OF NEURODEGENATIVE AND NEURODEVELOPMENT DEFECT MUTATIONS IN <i>C. ELEGANS</i> 76		
6.1	Introduction.....	76
6.2	Materials and Methods.....	78
6.2.1	Microfluidic device fabrication, design, and operation	78
6.2.2	<i>C. elegans</i> strains, culture, mutagenesis, and imaging	79
6.2.3	Probability model used for PQR characterization and analysis.....	79
6.2.4	Intensity profile peak detection for classification of neurodegenerative phenotypes	82
6.3	Results and Discussion	82
6.3.1	Microfluidic devices used for manual genetic screening.....	82
6.3.2	Manual screen to find mutants expressing neurodegeneration and neural developmental defects.....	85
6.3.3	Algorithm to detect and characterize neurodegenerative and neural development mutants	88
6.3.4	Software validation using known phenotypes of isolated alleles	93
6.4	Conclusions.....	96
CHAPTER 7 CONCLUSIONS AND FUTURE DIRECTIONS..... 98		
7.1	Research significance.....	98
7.2	Future directions	101
APPENDIX.....105		
A.1.	Laterally Orienting <i>C. Elegans</i> Using Geometry At Microscale For High-Throughput Visual Screens In Neurodegeneration And Neuronal Development Studies	105
A.2.	Automated Screening Of <i>C. Elegans</i> Neurodegeneration Mutants Enabled By Microfluidics And Image Analysis Algorithms.....	106
A.2.1.	Motor neuron segmentation	106
A.2.2.	Automated system operation.....	107
A.2.3.	Neuron distribution for alleles isolated from same F1 population	110
A.3.	High throughput characterization of spherical objects using modified granulometry algorithm for rapid characterization of <i>C. elegans</i> lipids.....	114

A.3.1.	Specialized software method for epi-flourescent data	114
A.4.	Automated characterization of neurodegenative and neurodevelopment defect mutations in <i>C. elegans</i>	115
A.4.1.	Image preprocessing, worm body detection, neuron segmentation, and cell body isolation.....	115
A.4.2.	Connectivity model used for joining PQR segments.....	117
A.4.3.	Deleting invalid objects	117
A.4.4.	Reassigning current evaluation points and dendrite process selection	118
A.4.5.	Estimating probability of connection.....	118
A.4.6.	Calculating angle probability of connection	119
REFERENCES	120

LIST OF TABLES

Table 1. Summary of software analysis of single-size population bead experiments.	66
Table 2. Number of D-type motor neurons detected for all alleles.	113

LIST OF FIGURES

Figure 1. Microfluidic device to passively orient <i>C. elegans</i> for visual screening	16
Figure 2. Effect of curved channel on animal orientation.	20
Figure 3. Morphology of wild-type and defective D-type motor neuron commissures. ..	25
Figure 4. Adult phenotype characterization.....	26
Figure 5. L1 phenotype characterization.	27
Figure 6. Cell specific characterization for L1 animals.....	28
Figure 7. Single layer microfluidic device.....	40
Figure 8. Suppressor of <i>smn-1</i> phenotype from manual pilot screen.	42
Figure 9. On-chip image analysis for system automation.....	44
Figure 10. Application of mean-filter to remove false positives.	47
Figure 11. Average number of D-type motor neurons per allele.....	49
Figure 12. Characterization of isolated alleles.....	51
Figure 13. Granulometry process on example image.	59
Figure 14. Size analysis of synthetic images.	62
Figure 15. Effect of object proximity and intensity variation on software results.	63
Figure 16. Size analysis of fluorescent beads.	64
Figure 17. Software analysis of single-size population bead experiments. Sum of all image results instead of mean shown for this figure.....	65
Figure 18. Lipid analysis of <i>C. elegans</i> images.....	68
Figure 19. Intensity analysis of single lipids for wild-type and <i>atln-1</i> mutant populations.	70
Figure 20. Software analysis of lipid size for epi-flourescent data.....	73
Figure 21. Devices used for manual genetic screening and nematode age compatibility.	83
Figure 22. Movement of animals in curved and straight channel devices.....	85
Figure 23. Example phenotypes of mutants isolated from pilot screen.....	86

Figure 24. Penetrance of specific defects for isolated alleles.	87
Figure 25. Software characterization of PQR neuron.	92
Figure 26. Qualitative accuracy examples.	94
Figure 27. Proportion of adult animals in a population with at least one incidence of each independent defect (%).	105
Figure 28. Proportion of L1 animals in a population with at least one incidence of each independent defect (%).	106
Figure 29. Penetrance of defects per cell in L1 populations with at least one incidence of each independent defect (%).	106
Figure 30. System level diagram of operation.	109
Figure 31. Histogram for alleles <i>a183</i> , <i>a184</i> , and <i>a185</i>	110
Figure 32. Histogram for alleles <i>a186</i> , <i>a187</i> , and <i>a188</i>	111
Figure 33. Histogram for alleles <i>a190</i> and <i>a192</i>	112
Figure 34. Histogram for alleles <i>a199</i> , <i>a200</i> , and <i>a201</i>	113

LIST OF SYMBOLS AND ABBREVIATIONS

<i>C. elegans</i>	<i>Caenorhabditis elegans</i>
GFP	Green fluorescent protein
ND	Neurodegeneration
PDMS	Polydimethylsiloxane

SUMMARY

Since its introduction in 1960's, the model organism *Caenorhabditis elegans* has played a crucial role towards scientific discoveries because of its relatively simple anatomy, conserved biological mechanisms, and mapped genome. The organism also has a rapid generation time and produces a large number of isogenic progeny, making *C. elegans* an excellent system for conducting forward genetic screens. Conventional screening methods, however, are labor intensive and introduce potential experimental bias; typically, large-scale screens can take months to years. Thus, automated screening and characterization platforms can provide an opportunity to overcome this bottleneck.

The objective of this thesis is to develop tools to perform rapid phenotypical characterization of *C. elegans* to enable automated genetic screening systems. To achieve this goal, I developed methods to increase throughput of worm handling using microfluidic devices and demonstrate software modules to phenotype unknown mutants using quantitative and morphological image analysis methods. This thesis work is divided into four major projects, each of which is summarized below.

First, I design a simple and robust method for passively orienting worms into lateral body positions in microfluidic devices. Recently, microfluidic devices have been used for high-throughput genetic screens, replacing traditional methods of manually handling *C. elegans*. However, the orientation of nematodes within microfluidic devices is random and often not conducive to inspection, hindering visual analysis and overall throughput. I developed this design in order to facilitate inspection of morphological features with specific dorso-ventral alignments. Using this technique, I demonstrate the ability to position animals into lateral orientations with up to 84% efficiency, compared to 21% using existing methods. Additionally, I show the isolation of six mutants with neuronal development or neurodegenerative defects, validating that the technology can be used for on-chip analysis and high-throughput visual screens.

Second, I engineer an automated system capable of performing genetic suppressor screens on *C. elegans* using the microfluidic design from the previous project in combination with custom image analysis software. I use this system to search for genes involved with spinal muscular atrophy (SMA), a degenerative disorder that selectively deteriorates motor neurons due to a deficiency of survival motor neuron protein (SMN). SMA is the leading genetic cause of death in infants and is difficult to study in complex biological systems such as humans; however, *C. elegans* can be used to study the specific mechanisms underlying this disease through the *smn-1* gene, a homologue of SMN. In this project, I demonstrate the utility of the designed system by isolating 21 alleles that significantly suppress motor neuron degeneration at a screening rate of approximately 300 worms per hour. Furthermore, the system is modular and easily adaptable, providing a means to saturate screens not only implicated in the *smn-1* pathway, but also for genes involved in neurodegeneration in general.

Third, I expand on previous computational methods of analyzing circular cell bodies in low densities by using a modified granulometry algorithm to rapidly characterize large quantities of lipid droplets. A common problem in medical imaging is characterizing dense quantities of biological structures using standard segmentation techniques due to variations in object size, large amounts of occlusion, and non-uniform image intensity. The granulometry algorithm, introduced in the 1960's, can be used to characterize dense images without the need to segment the image. This is performed by using a series of morphological processing operations to filter objects of various sizes. To validate the technique, we study *C. elegans* lipid distributions under various conditions. Lipid storage is widely studied in *C. elegans* since many genes and proteins involved in fat storage, transport, and metabolism are highly conserved in vertebrate systems. Using this method, I demonstrate the ability to recreate lipid distribution trends seen in published studies, showcasing the ability of our algorithm to produce results comparable to manual analysis. Our method improves upon throughput of manual characterization of

lipid droplets, decreasing time requirements by 1000 fold, and eliminates the need to create 3D reconstructions from multi-focal plane image acquisition. Additionally, we demonstrate the ability to perform rapid computational analysis on low fidelity images acquired from epi-fluorescent microscopy systems, enabling real-time on-chip screening of for lipid mutations on comparatively inexpensive imaging systems.

Lastly, I present a method to correct for poor binarization of intensity-based segmentation techniques applied to neuronal processes using a probabilistic connectivity model. Using this model, I simultaneously enable a peak intensity method for the classification of neurodegenerative phenotypes. *C. elegans* is commonly studied in neurodegeneration and neural developmental research due to the number of available neuropathology mutants and highly conserved neural developmental cues and neurotransmitter systems. Using the connectivity model to facilitate analysis of the tail sensory neuron PQR, I demonstrate an accuracy up to 80% for correctly identifying the neuron, joining incorrectly segmented and fragmented process segments when necessary. Additionally, I show a classification accuracy of 75% for neurodegenerative phenotypes when connectivity model returns faultless results. Run time for model and classification methods combined average approximately 10 seconds, and like our previous work, enables the potential to perform automated screens when combined microfluidic technology.

In this thesis, I integrate microfluidic chip and computer vision technologies to rapidly characterize both small and large quantities of spherical objects in addition to curved structures, enabling the rapid analysis of a multitude of phenotypes commonly seen in biology. This work is significant because it increases current capabilities of screening small animals with morphological phenotypes by enhancing throughput and reducing human bias. Genes or gene functions that can be discovered using these methods can further elucidate mechanisms relevant to neural development, degeneration,

maintenance, and function; these discoveries in turn can facilitate discoveries of potential therapeutic strategies for human diseases.

CHAPTER 1 INTRODUCTION

The work presented in this dissertation aims to provide tools, analysis methods, and an automated system to aid scientists performs genetic screens by removing bottlenecks in current practices and technologies. To accomplish this goal, techniques from various fields such as biology, neuroscience, genetics, image processing, and system integration are applied in concert to create novel solutions to long-standing and existing problems with low throughput studies requiring manual operations and analysis. The focus of this work involves designing technology for, but not limited to, the comparatively simple organism *Caenorhabditis elegans*, widely used as a model to study various biological processes and diseases. I present four methods to characterize and investigate *C. elegans*, increasing throughput and improving inspection by using microfluidic chips in combination with image analysis methods. Using these methods, I demonstrate the ability to perform high throughput quantitative screening and classification of mutant phenotypes, enabling the construction of a system for performing automated genetic screens. This technology facilitates the study of the genetic and molecular causes related to pathologies such as neurodegeneration and obesity.

1.1 Thesis objectives

Aim 1. Design microfluidic device to simplify genetic screens performed on *C.*

elegans: Recently, scientists and engineers have demonstrated microfluidic systems capable of automated sorting and performing computer assisted genetic screens of *C. elegans*. However, animal loading within such devices is random, inhibiting inspection of biological features of interest along the ventral and dorsal body length, a body surface normally seen during animal locomotion and standard inspection methods. Additionally, current devices used for automated sorting are often highly complex, requiring separate cooling systems or complex device structures for animal immobilization. To alleviate these issues, I designed a microfluidic device for performing automated phenotypic

screens that passively orient animals within microfluidic channels; furthermore, the design uses a comparatively simple partial immobilization method to facilitate phenotype inspection and analysis. The microfluidic chip is constructed from polydimethylsiloxane (PDMS) using the well-established soft lithography process and positions animals into lateral orientations by using a curved channel that promotes nematode self-positioning. The device simultaneously partially immobilizes nematodes by constricting their movement within an imaging chamber without the use of anesthetics.

Aim 2. Develop software modules to phenotype unknown mutants using quantitative and morphological image analysis methods: Animals inspected in this work were examined by custom image-analysis software created in MATLAB®. Software utilizes basic feature-detection methods and tunable parameters, making methods flexible to not only investigate mutants specific to this project, but other strains of the nematode for future studies as well. Worm phenotype is determined by quantitatively analyzing expression patterns of fluorescent neurons or lipid droplets and increases the throughput of manual screening methods by a minimum of 100 fold.

Aim 3. Perform automated screens to validate developed technology: An automated screen was conducted by chemically mutagenizing a population of animals and then introducing them into the microsystem. The system successfully identified mutants by investigating neurons expressing green fluorescence protein (GFP). Semi-automated pilot screens were also performed to validate the proposed technology and pave the way for future applications of automated genetic screens of fluorescent markers in *C. elegans*.

CHAPTER 2 LITERATURE REVIEW

This chapter introduces the model organism *C. elegans* and familiarizes the reader with the standard methods used in *C. elegans* research and why the organism is significantly studied in the field of neuroscience. The chapter also discusses the research area of microfluidics and how the technology has impacted biomedical and *C. elegans* research. Lastly, an overview of image processing as it relates to biomedical research is presented before discussing common segmentation and morphological image processing techniques. The chapter ends with a review of image processing methods that have facilitated *C. elegans* research. Information provided in this chapter is meant to familiarize the reader with the current methods and their limitations.

2.1 The model organism *C. elegans*

The soil nematode *C. elegans* is well-suited model organism for biological research because of its transparent nature (allowing *in-vivo* study of fluorescent markers), short generation time (three days), and ease of culture¹. The animal is commonly used in a wide range of studies including genomics, neuroscience, cell biology, aging, and development. While only comprised of 302 neurons, the nematode's simple and well characterized nervous system is surprisingly capable of a wide range of behavior including chemotaxis, thermotaxis, and learning²⁻⁴. The animal is also ideally suited for genetic studies because: (1) over 99 percent of organisms in wild-type populations are self-fertilizing hermaphrodites, (2) *C. elegans* was the first multicellular organism to have its complete genome sequenced, (3) RNA interference (RNAi) can be used to knockdown specific genes in the animal, and (4) many mechanisms between the nematode and humans are highly conserved with homologues available for approximately 60 to 80 percent of human genes^{1,5-7}.

Since its introduction by Sydney Brenner, *C. elegans* has been involved in many key discoveries in the field of biomedical research. The Nobel Prize in physiology and

medicine was awarded both in 2002 and 2006 to scientists who used *C. elegans* for discoveries concerning organ development and programmed cell death and for gene silencing using RNAi respectively. The Nobel Prize in chemistry was also awarded in 2008 to scientists who developed GFP in the nematode. The animal has even been used to elucidate several genes involved in diseases such as Alzheimer's, type II diabetes, obesity, and depression, providing novel targets or methods to study therapeutic treatment for such ailments¹. With applications in cell biology, drug discovery, neuroscience, and genetics, there is no doubt that many key findings using *C. elegans* as a tool for discovery remain to be seen.

2.1.1 Standard genetics screening methods of *C. elegans*

C. elegans is ideally suited for genetic studies because of its mapped genome and large number of human disease gene homologues. In addition, the animal's ability to produce approximately 200 progeny provides the opportunity to perform large scale screening on a multicellular organism (as opposed to yeast) and within a short period of time (three days versus weeks and months for flies and mouse models respectively)⁸. With RNAi libraries containing targets for over 16 thousand of the 19 thousand genes in the worm, the potential impact of large scale screening of the nematode is clear⁸.

Despite the potential, standard practices for screening *C. elegans* are time-consuming and low-throughput^{9,10}. First, individual animals are picked from an agar plate and placed onto a microscope slide. The slide is usually prepared with an anesthetic such as sodium azide to immobilize the animal. When slide preparation is complete, worms are analyzed, identified, and then rescued and isolated onto a new plate. This entire process is then repeated for hours on end, for several days. Performing this manual process in a normal clonal screen provides a throughput of approximately ten haploid genomes per hour for an experienced scientist. At this rate of examination, saturating a

genetic screen, requiring the inspection of thousands of haploid genomes, would involve months, if not years, of labor intensive inspection.

2.1.2 *C. elegans* as a model for neurodegeneration

Knowledge of the molecular mechanisms underlying neurodegeneration and neuronal development are critical for advancing the treatment of neurological pathologies; however, these processes in general are not fully understood. *C. elegans* presents an exquisite opportunity to elucidate some of these pathways despite its low level of evolutionary complexity. This is because of the high level of conserved mechanisms between the nematode and vertebrates. For example, similar to that of mammals, the development of the *C. elegans* nervous system is regulated by common guidance and polarity cues such as Netrin, Slt, Wnt, and Par protein complexes¹¹⁻¹⁵. Adding to the considerable number of conserved molecular pathways between worms and mammals are major neurotransmitter systems as well^{1,16}. Previous research has used *C. elegans* to study molecular mechanisms behind devastating neurodegenerative disorders such as Alzheimer's, Parkinson's, amyotrophic lateral sclerosis, and Huntington's disease^{1,16-19}. Furthermore, *C. elegans* have a mapped and comparatively simple nervous system of 302 neurons, unlike other model organisms that contain thousands to millions of neurons, greatly simplifying analysis of neuronal circuits²⁰. The nematode is also uniquely fit for neurodegeneration research because it is transparent, allowing for the inspection of fluorescently labeled neurons within a living multicellular organism at all stages of development^{1,16,21}.

2.2 Microfluidics

Microfluidics, the science and technology of manipulating fluids using channels and actuated components on the micrometer scale, is governed by changes to the fundamental physics of fluid mechanics as scale decreases from the macro to the micro scale. Generally for macroscopic fluids, convective mixing occurs when two fluids meet due to

dominant inertial forces; however, viscous forces are normally dominant for flow at micro scales. Therefore, microfluidic flows are laminar (never turbulent), and generally only mix through diffusion^{22,23}. This property can be exploited to route fluids and fluid contents in desired manners allowing for fluid and particle separation, manipulation, filtration, and controlled mixing using chaotic mixing methods²⁴. Flow can also be exploited for very well controlled mass and energy transfer to create distinct and separately controlled temperature regions and gradients within devices^{25,26}.

Another advantage of microfluidic technologies is the ability to integrate with electrical components and systems to provide automated platforms to perform experiments. For example, electronics are commonly used in combination with microfluidic devices to perform on-chip electrophoresis, temperature control of microenvironments, manipulation of droplets, and for flexible sensors²⁷⁻³¹. Additionally, integrating microfluidic platforms with camera and pneumatic valve systems enables automation of experiments³²⁻³⁴.

2.2.1 Soft lithography as a tool for biomedical research

The advent of soft lithography using polydimethylsiloxane (PDMS) was undoubtedly one of the major contributors responsible for the surge in development in the field of microfluidics. Coupled with techniques for creating pneumatically activated valves and on-chip mixers, complex microfluidic designs have been constructed allowing for the creation of complete microanalysis systems on a single chip, often referred to as lab-on-a-chip devices^{22,35}. One of the main reasons for this increase in microfluidic technology is attributed to the low-cost and rapid prototyping capabilities of PDMS, allowing for fabrication within days instead of weeks when compared to traditional microfabrication techniques³⁶. Fabrication using PDMS involves a micromolding processes where PDMS is cast over a silicon wafer patterned with photoresists (referred to as a master wafer) using standard photolithography. The master wafer is then allowed to cure and the

resulting PDMS mold is peeled off. At this point, the mold is then usually bonded to glass creating the base for the microfluidic device and completing the fabrication process³⁵⁻³⁷.

PDMS microfluidic devices are naturally suited for biomedical applications because of their small reagent volume, capability for parallelization, short reaction times, low cost, transparency, and adjustable surface biochemistry^{23,38}. While many of these advantages are inherent because of the small scale of these devices, it is the application of this technology to the life sciences discipline which makes it novel. For the reasons mentioned above, it is no surprise that soft lithography has been utilized in many different areas of biomedical research such as cell biology, proteomics, DNA manipulation, drug screening, bioanalysis, and multicellular organism manipulation^{22-24,38,39}. However, while microfluidics holds great promise for the fields of chemistry, biology, and medical research, it is still an emerging technology and mainly limited for use by experts in the field because associated equipment is complicated, requiring external pressure sources to control hardware or pumps for fluid injection²².

2.2.2 Microfluidics and *C. elegans*

In recent years, researchers have begun to use microfluidics for handling *C. elegans*, in order to facilitate animal manipulation and increase overall throughput of genetic and pharmacological screens^{32,40-43}. In addition to screening applications, microfluidic methods have significantly reduced the amount of time-consuming manual operations normally required for different *C. elegans* experimentations, such as imaging, laser-axotomy, synapse and cell-ablation, and long-term culture^{29,33,34,40,43-49}. Researchers have also designed and utilized microfluidic chips to investigate neuronal activity and behavior ranging from locomotion, to chemosensation, and even learning⁴⁹⁻⁵⁴.

One frequent challenge when examining *C. elegans* in microfluidic devices is immobilizing the animal during image capture or during laser operations. This is of particular importance when examining cellular or subcellular sized objects (organelles,

proteins, etc.) on multiple focal planes or performing laser surgeries, each of which requires seconds to perform. Currently, existing techniques used to immobilize animals involve using temperature to rapidly cool animals, compressive force or restrictive channels to prevent movement, carbon dioxide microenvironments to replace and reduce oxygen available, and biocompatible Pluronic polymers with reversible thermo-sensitive sol-gel transitions, capable of surrounding nematodes and preventing animal movement^{39,41,45,46,55-58}.

2.3 Image analysis for biomedical applications

Image analysis is a subfield of computer science concerned with extracting data from digital images using various processing algorithms. Used traditionally for applications in machine and computer vision such as facial, text, and object recognition, image analysis has begun to emerge in the past decade as a major player in complex processes in bioinformatics such as disease classification^{59,60}.

The main reason for this surge in applying image analysis methods to biomedical problems has been technological advances which have enabled acquisition of large datasets through techniques such as high-throughput screening, large scale assays, improved microscopy techniques, and the ability to fluorescently label various biological tissues or proteins⁶⁰⁻⁶⁴. Datasets are often too complex or too large in volume to study manually, requiring multimodal analysis or data reduction. As such, scientists are quickly becoming overwhelmed with data and image analysis can provide techniques to aid with many common problems. One of the major interests in image analysis is the possibility of using its methods to improve disease detection, allowing for early treatment while providing more objectivity to diagnosis. For example, image processing combined with machine learning algorithms have been used in mammographic screening, stroke diagnosis, and automatic classification of Alzheimer's disease⁶⁵⁻⁶⁷.

In addition to disease classification, image analysis techniques have also been used to create software packages specific for analyzing anatomical features for various model organisms in automated fashions. ZFIQ is software platform for cell quantification and neuron detection of zebrafish while StarryNite provides a method for automated cell lineage tracing during *C. elegans* embryogenesis⁶⁸⁻⁷⁰. CellProfiler is another software package available which was similarly created to identify and analyze cells, however, is not specific to any organism⁷¹.

2.3.1 Segmentation methods

One of the most basic of image processing techniques is the separation of objects of interest (foreground) from the background, or segmenting an image. This process can also be considered as establishing a threshold for the image, and assigning all pixels values at or above the threshold to be foreground, while the remaining pixels are converted to background. This process is used on a multitude of processing techniques from extracting text from documents, map processing, cell identification, medical imaging analysis, and almost any form of targeted object detection⁷²⁻⁷⁸. The result of this process is the binarization of an image, leaving background pixels with a uniform value (typically logical data type 0), and foreground pixels or objects of interest with a different uniform value (typically logical data type 1). While many segmenting techniques exist based on different image and object characteristics such as histogram shape, entropy, object attributes, and spatial based methods, the scope of this background will take into consideration only two subclasses of segmentation methods: Otsu and Niblack thresholding algorithms.

Otsu thresholding is a cluster-based method that automatically chooses a global threshold that minimizes the intraclass variance between background (black) and foreground (white) pixels⁷⁹. Since its introduction in 1979, the algorithm has been widely used and remains one of the most referenced thresholding methods⁷⁷. The Niblack

algorithm, on the contrary, uses an adaptive method which changes the threshold based on the mean and standard deviation of a local neighborhood of the image^{77,80,81}. This method is particularly adept to compensating for changes in illumination in the image and has spawned several variations of the algorithm which seek to improve segmentation by adapting the contribution of the standard deviation for especially noisy images^{77,80,82}.

2.3.2 Morphological processing

Morphological image processing refers to the practice of using structuring elements of different shapes and sizes to perform mathematical and relational operations on an image. The subfield has wide applications in the field of image processing and can be used for inspection, biomedical imaging, document processing, pattern recognition, metallurgy, microscopy, and robot vision^{83,84}. For the scope of this work, only a cursory overview of the basic operations of erosion, dilation, opening, closing, top-hat, and bottom-hat will be explained for grayscale images.

Grayscale erosion and dilation operations are equivalent to a moving minimum and maximum filter respectively, where the window is defined by the structuring element used for the operation^{83,84}. The resulting image is calculated by aligning the midpoint of the structuring element with the pixel of the original image being evaluated, and is repeated for each pixel in the image. The morphological opening operation is the dilation of the result of an erosion using the same structuring element, i.e.

$$I \circ \lambda = (I \ominus \lambda) \oplus \lambda \quad (1)$$

where \circ , \ominus , and \oplus are the morphological opening, erosion, and dilation operators, and I and λ represent the original image and the structuring element used respectively. Conversely, the morphological closing operation is the erosion of the result of a dilation using the same structuring element, or

$$I \bullet \lambda = (I \oplus \lambda) \ominus \lambda \quad (2)$$

where \bullet is the morphological closing operator. Similar in this relationship, are the top-hat and bottom-hat operations. The top-hat operation is the result of subtracting the morphological opening from the original image and is normally used as a preprocessing method to correct for uneven illumination or to estimate and remove background noise⁸⁴. Conversely, the bottom-hat operation is the result of subtracting the morphological closing from the original image and is often used as a means to enhance image contrast.

2.3.3 Image analysis and *C. elegans*

Image processing techniques have been utilized in *C. elegans* research for performing analysis of complex behaviors, neuron detection, characterization of expressed biomarkers, optogenetic stimulation, and cell lineage tracking^{32-34,40,46,70,85-90}. To study locomotion behavior, various laboratories have created and released software capable of tracking anywhere from a single animal to over 100 nematodes simultaneously⁸⁹. These methods use basic thresholding techniques to segment animals from background pixels to extract worm body shape and create a skeleton to quantify various attributes⁸⁹. Similarly, optogenetic stimulation combines real-time tracking of animals using similar thresholding and skeletonization methods, using results of the process to pinpoint specific stimulation areas using a micromirrors or modified projector systems^{85,90}. Other behavior analysis methods combine thresholding methods with the Hough transform to detect body circularity to perform behavior-based chemical screens⁸⁶. Principal component analysis and conversion of movie frames to covariance matrices has also been utilized to analyze worm thrashing behavior, circumventing the need for body segmentation, to correlate animal thrashing to motor neuron degeneration^{87,88}.

Previous work from the Lu laboratory has demonstrated the ability to perform automated phenotyping and laser ablation by using thresholding methods to detect fluorescently labeled neurons^{32,46}. More complex algorithms utilizing machine learning methods such as support vector machines have also been used to detect synapses and

perform an automated screen searching for mutants by comparing over 100 different image metrics³⁴. Other laboratories have also used comparatively simple thresholding methods to aid manual axotomies during drug screening to identify compounds that effect neuronal regeneration⁹¹.

Lastly, Bao *et al.* developed software methods to perform cell lineage tracking resulting in the software package StarryNite⁷⁰. StarryNite uses a combination of local maxima analysis to detect GFP-histone-labeled nuclei with a nearest neighbor and minimal movement algorithm to keep track of cells in 4D⁷⁰. In summary, many algorithms and methods for performing image analysis to characterize and quantify *C. elegans* research exist, yet no one specific method is capable of solving all research interests. While all algorithms are unique, current *C. elegans* image analysis techniques rely heavy on thresholding methods to segment objects and biological tissues of interest.

CHAPTER 3 LATERALLY ORIENTING *C. ELEGANS* USING GEOMETRY AT MICROSACLE FOR HIGH-THROUGHPUT VISUAL SCREENS IN NEURODEGENERATION AND NEURONAL DEVELOPMENT STUDIES

The following work in this chapter was performed in conjunction with Dr. Nicholas Valmas, in collaboration with Dr. Massimo Hilliard's laboratory at the University of Queensland, Australia.

3.1 Introduction

For many applications utilizing microfluidic chips, a specific nematode body orientation is required. For example, visual inspection of neurons and their processes requires animals to be oriented with these structures as close as possible to an imaging objective without visual obstruction by other tissues. Similarly, a specific body orientation facilitates inspections of neuronal features, such as neurite trajectories^{92,93}. The *C. elegans* D-type motor neurons perfectly exemplify this situation. This class of 19 GABAergic neurons is crucial to the normal coordinated locomotion of *C. elegans*, and can be highlighted in animals carrying the *juIs76* transgene, which expresses green fluorescent protein (GFP) under the control of the *unc-25* (a gene encoding glutamic acid decarboxylase) promoter¹⁰. When visualized with *juIs76*, the D-type motor neurons show discrete single process commissures that run between the ventral and dorsal nerve cords (VNC and DNC, respectively) for the entire animals' body¹. These commissures provide multiple opportunities to visualize phenotypic defects, when the animal is oriented in a precisely lateral position, and are ideal for studying neurodevelopmental and neurodegeneration abnormalities. While techniques to influence anterior versus posterior entry into microfluidic channels exist⁹⁴, no methods have yet been reported to bias lateral orientation.

Here we present a simple microfluidic device designed to passively orient *C. elegans* by exploiting a curved channel geometry. We conducted a pilot forward genetic screen for neurodevelopmental and neurodegeneration phenotypes and isolated six independent mutants, demonstrating that on-chip analysis and high-throughput visual examination can be performed using our design. We also show that our device can be used on animals without altering viability or reproductive capabilities. The advantages of using this system are threefold. First, our curved channel geometry orients animals passively, which makes the operation simple and robust, and facilitates high-throughput analysis of *C. elegans* strains requiring lateral orientation. Second, the curved design increases nematode body area within the microscope field of view, reducing the need to move the sample in order to inspect the entire worm body. Finally, the system is comparatively simple, potentially allowing non-experts to operate the device.

3.2 Materials and Methods

3.2.1 Microfluidic device fabrication and operation

We designed and fabricated a two-layer microfluidic device using polydimethylsiloxane (PDMS, Dow-Corning) and standard multi-layer soft lithography techniques³⁵. A loading chamber was designed to store nematodes in the device until they are sent to the imaging area (red dashed box in Figure 1A) to be analyzed and subsequently sorted through one of two exits. Nematode loading and sorting within the device was controlled through the actuation and use of partially-closed valves in conjunction with pressure-driven flow (Figure 1B, Figure 1C, and Figure 1D). To reduce imaging chamber distortion during analysis, control channels were filled with a 58% glycerol solution³³.

Device geometry was designed by selecting values similar to worm body dimensions. Channels within the imaging area are about the size of a gravid adult, 70 μm in width, while the standard arc length (L) between loading and imaging valves is 700

μm to help restrict animal movement. The arc length between the loading and imaging valves was modified to approximately 500 μm or 900 μm to accommodate for *dpy-4* and *lon-3* mutants whenever necessary. Standard radius of curvature (RoC) for the curve in the imaging area is 125 μm from the arc center to the outer edge of the channel to allow for a 20 μm increase or decrease, while still meeting mask printing space requirements. Lastly, flow channel height is approximately 75 μm , which is also slightly larger than the diameter of an adult nematode.

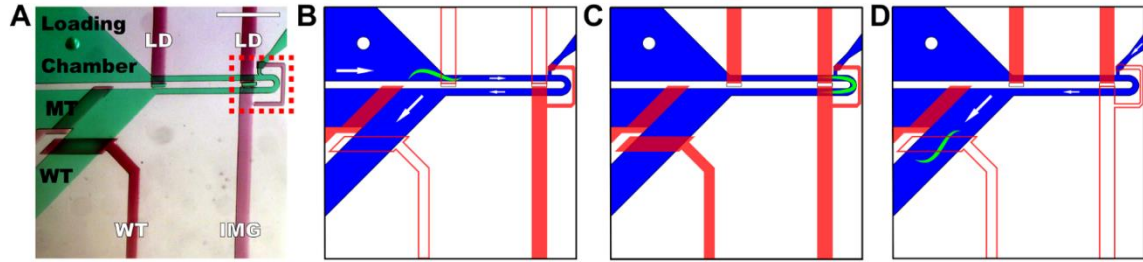


Figure 1. Microfluidic device to passively orient *C. elegans* for visual screening. (A) Device used for orienting, imaging, and sorting animals. Flow layer is shown in green with black text, valve control layer in red with white text. LD is loading valve, MT is channel for mutant output, and WT is channel (black) and valve (white) for wild-type output. IMG is imaging valve. Not labeled are the mutant valve (right of mutant channel) and flush channel (green area above red box). Input and flush channel fluid flow are controlled off-chip. Imaging area is indicated by red dashed box. Scale bar is 800 μm . (B) Device schematic of valve state during worm loading. Worm is driven into imaging area using positive input pressure to induce fluid flow. Loading valve is not actuated, allowing fluid flow. Imaging valve is actuated to prevent worm from exiting imaging area. Wild-type valve is not actuated to assist in worm loading and to provide an exit should an animal slip past the imaging valve. Mutant valve is actuated to prevent animals from entering mutant output. (C) Device schematic of valve state during analysis. All valves are actuated and input pressure is cut off halting fluid flow. (D) Device schematic of valve state during worm sorting. Example for wild-type sorting is shown. Worm is driven out of the imaging area by positive pressure from the flush channel. Loading valve is actuated to prevent any other animals from entering the imaging area. Imaging valve is not actuated to allow worm exit. Wild-type valve is not actuated to allow worm exit into wild-type output. Mutant valve is actuated to prevent animals from entering mutant output. Mutant and wild-type valve state is reversed when mutant sorting is performed. Fluid flow direction indicated by white arrows and is not proportional to size of arrow. Non-filled and filled red boxes indicate non-actuated and actuated valves respectively.

3.2.2 Orientation Analysis

C. elegans were analyzed in various microfluidic designs to test locomotory defects, body type differences, and the effect of the imaging area's RoC on lateral orientation. Animals were grown until gravid adults and then evaluated. Five-second videos were captured per animal and were visually analyzed to determine animal orientation.

For wild-type animals, videos were acquired at 32 frames per second using a CCD camera (Hamamatsu C9100-13), and were recorded using a 20 \times /0.5NA magnification

objective in fluorescence mode on a wide field upright compound microscope (Leica DM4500). Videos for *dpy-4 juIs76* and *lon-3 zDIs5* mutants were acquired at 26.1 frames per second using a CCD camera (Lumenera INFINITY3 1M) and were recorded using a 20×/0.4NA, and a 10×/0.25NA magnification objective respectively. Videos for these mutants were also recorded in fluorescence mode on a wide field inverted compound microscope (Leica DMI6000 B).

Animals carrying the *juIs76* transgene were scored as laterally oriented if GFP-labeled dorsal and ventral nerve cords could be clearly seen throughout the duration of the video. Conversely, animals were scored as not lateral if either nerve cord was obstructed at any point along the worm body due to a rotated body position within the microchannel. In animals carrying *zDIs5* transgene, since both ALM and PLM are bilaterally symmetric neurons, animals were scored as laterally oriented if only one neuronal process (either left or right) could be clearly seen throughout the duration of the video for the anterior and posterior body (ALM and PLM respectively). Conversely, if both the left and right processes for either ALM or PLM were seen in the same focal plane at any time during the video, animals were scored as not lateral. Expression of GFP in first and last quarters of the animal's body (head and tail) was ignored since the tapered nature of the worm makes both ALML/ALMR and PLML/PLMR processes visible in the same focal plane.

3.2.3 C. elegans culture, mutagenesis, and phenotype scoring

C. elegans strains used in these studies were *juIs76(Punc-25::GFP)*, *zDIs5(Pmec-4::GFP)*, CZ1931 *unc-71(ju156) juIs76(Punc-25::GFP)*, QH3736 *lon-3(e2175) zDIs5(Pmec-4::GFP)*, QH3833 *dpy-4(e1166) juIs76(Punc-25::GFP)*, and CX8600 *kyIs417(Podr-1::dsRed, Pgcy-36::GFP)*. All animals were grown between 20°C and 25°C using established culturing protocols^{95,96}. Mutagenesis was performed using standard

techniques and concentrations of the chemical mutagen ethyl methanesulfonate (Sigma Aldrich) to perform a pooled F2 screen on wild-type *juIs76* animals¹⁰.

F2 progeny were cultured for 2.5 to 3.5 days (dependent on cultivation temperature) and visually examined on-chip. Animals were isolated if they presented, any breaks or gaps in neuronal processes, misguided commissures, or any gross difference in neural morphology when compared to wild-type. Animals isolated for exhibiting phenotypic abnormalities were further examined on agarose pads using 5 mM sodium azide (Sigma Aldrich) or 0.01% tetramisole (Sigma Aldrich) as an anesthetic⁹⁷.

Adult animals three to four days old were analyzed for morphological defects in each commissure of 16 of the 19 D-type motor neurons. The VD1 neuron was omitted as its morphology is confounded by the RME neurons; in addition, the DD1 and VD2 commissures could not be accurately scored as they travel on the opposite side of the body (this was not the case in the *vd029* mutant, so all these cells were also scored). Larvae were analyzed early in the L1 stage, within six hours of hatching and prior to the development of the VD neurons, so that all six DD neurons could be individually scored.

Animals were visualized with 20×/0.5NA, and 40×/0.75NA magnification objectives on a wide field upright compound microscope (Zeiss Axio Imager Z1). Images were captured using a CCD camera (Photometrics CoolSNAP HQ2), and Z-stacks were manually flattened to a single plane in Adobe® Photoshop® CS3.

3.2.4 *C. elegans* mock screen and egg-laying assay

For the mock screen, M9 solution containing approximately 1,000 wild-type (*juIs76*) adult animals was prepared. Ten adult *lon-3* (*zdIs5*) mutants were then individually picked and placed into the solution. This population of animals was then sorted through our microfluidic device and then inspected under a dissecting microscope using high magnification to verify the phenotype of recovered animals. All animals were grown at 20°C.

To compare egg laying rates, animals were grown at 20°C until young adults and then separated into two populations. One population was then sorted through our microfluidic device. After 48 hours, progeny of the two populations were manually counted under a dissecting microscope at low magnification.

3.3 Results

3.3.1 Sample loading orientation and device characterization

The ability to consistently load animals into a specific orientation is often necessary for the visual detection of defects in genetic screens. The lateral body orientation of *C. elegans* is commonly seen in freely moving animals on an agar plate. This orientation is also the most useful for analyzing neuronal processes that travel along the antero-posterior axis, as well as processes that travel laterally across the worm body. In this work, we show that *C. elegans* preferentially adjust themselves into this lateral orientation as a result of the curved geometry of our device. We designed a microfluidic chip containing a novel curved microchannel, with a radius of curvature (RoC) of 125 μm , which laterally oriented animals with an efficiency of $84\pm 4\%$ (mean \pm standard error, $n = 76$) (Figure 1, Figure 2A–D). Comparatively, animals within straight channel devices, of similar channel width, orient laterally only $21\pm 3\%$ of instances ($n = 145$) and were otherwise rotated along the antero-posterior axis (Figure 2E and Figure 2F). Decreasing or increasing the RoC of the curved microchannel by 20 μm did not have a statistically significant effect on orientation efficiency ($p > 0.4$, chi-squared test), resulting in laterally oriented animals with frequencies of $74\pm 5\%$ ($n = 84$) and $82\pm 5\%$ ($n = 71$), respectively. Locomotory impaired animals (*unc-71*) similarly displayed a high efficiency of lateral orientation ($68\pm 5\%$, $n = 75$) within the device; in addition, animals with gross morphological defects, such as long (*lon-3*) or dumpy (*dpy-4*) mutants, also oriented laterally at a higher efficiency ($72\pm 5\%$, $n = 75$ for *lon-3* and $57\pm 6\%$, $n = 76$ for *dpy-4*). Therefore, we conclude that the gross morphology of animals will not considerably

impact the orientation efficiency of our device, making it suitable for operation with mutagenized populations.

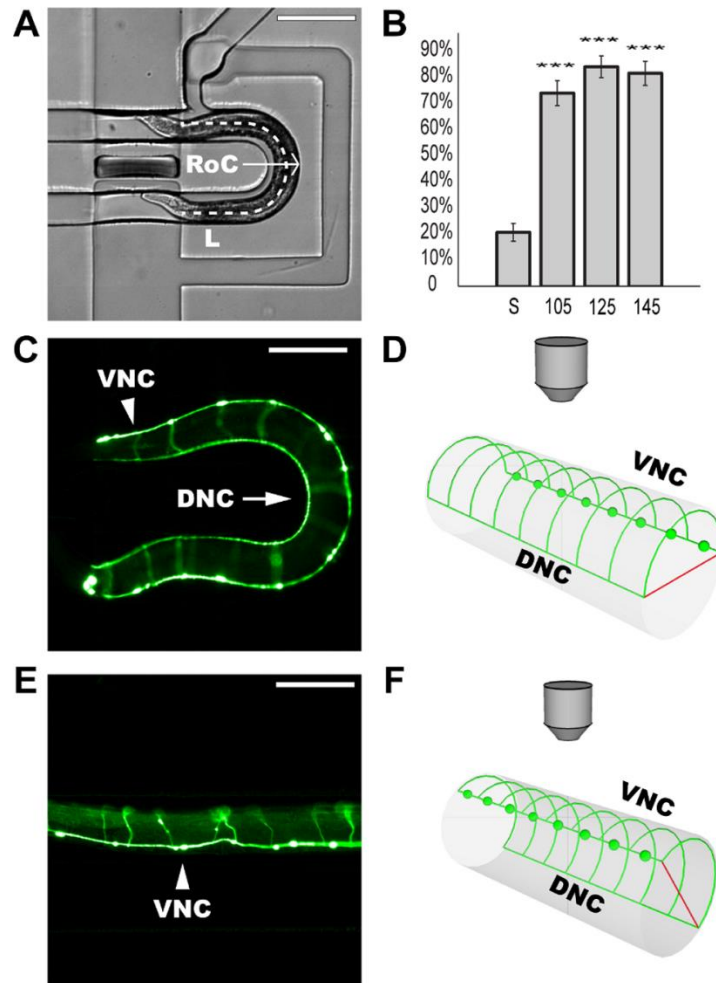


Figure 2. Effect of curved channel on animal orientation. (A) Zoomed in view of imaging area shown by dashed red box from Figure 1A. White arrow indicates device radius of curvature (RoC) from arc center to outer edge. Dashed line indicates length (L) between loading and imaging valves. Scale bar is 200 μm . **(B)** Frequency of lateral nematode orientation for various channel geometries with standard error of proportion. Triple asterisk indicates statistical significance compared to straight channel designs ($p < 0.001$ determined using chi-squared test). S represents straight channel, while remaining labels indicate the 105 μm , 125 μm , and 145 μm RoC devices respectively. L for all devices is 700 μm . **(C)** Nematode oriented laterally in curved channel device (both nerve cords visible). Commissures present on different focal plane are obscured. **(D)** 3-D model of animal body section and microscope objective (viewpoint reference) showing nerve cord placement for a laterally oriented animal. **(E)** Nematode in a non-lateral body orientation as observed when loading animals into straight channel devices; DNC not visible due to animal orientation. Animal is within the same field of view as seen in panel C. **(F)** 3-D model of animal body section and microscope objective (viewpoint reference) showing nerve cord placement for a non-laterally oriented animal.

Arrowheads for images (C) and (E) indicate ventral nerve cord (VNC) determined by placement of VD and DD motor neuron cell bodies. Arrow indicates dorsal nerve cord (DNC). Scale bars are 100 μ m. Transgene marker for all fluorescent images is *juIs76(Punc-25::GFP)*. (F) 3-D model of animal body section and microscope objective for non-lateral oriented animal. Model diagrams (D) and (F) not drawn to scale. Red lines illustrate dorso-ventral axis. Green spheres represent DD and VD neuron cell bodies.

To further characterize loading orientation bias in our curved channel device, we measured whether the worm's ventral or dorsal side faced the inside curve of the imaging area, along with whether the worm entered the imaging area head or tail first. We found that our curved device favors head entry of animals into the imaging area in $70\pm 6\%$ of instances compared to $30\pm 6\%$ for tail entry, (mean \pm standard error, $n = 69$, $p < 0.01$, chi-squared test). Additionally, the device also had a ventral bias of $59\pm 6\%$ versus a dorsal bias of $41\pm 6\%$ ($n = 69$, $p > 0.1$). When combined with our lateral orientation method, head-to-tail entry bias provides an opportunity to preferentially load animals into the device in known orientations, facilitating image acquisition and analysis of specific locations of the animal's body.

Our experiments suggest that curved channel geometries passively orient *C. elegans* with greater than 80% efficiency, while orientation within straight channel devices is random. Curved channels are therefore the best geometry to employ for examining *C. elegans* features aligned in the dorso-ventral plane, or along the lateral positions of the animals' body.

To verify compatibility of using our novel device for high-throughput animal handling and to estimate sorting efficiency, we performed a mock screen including animals expressing GFP in different neurons (mechanosensory neurons, *zDIs5* transgene) and with an elongated phenotype (*lon-3*). We successfully recovered 100% of *lon-3* (*zDIs5*) mutants ($n = 10$) from a population of $\sim 1,000$ wild-type (*juIs76*) animals with no false positives (i.e. no *juIs76* animals were sorted as *lon-3*; *zDIs5* animals). In addition, we also assessed whether on-chip manipulation altered animal viability or egg-laying in

wild-type worms 48 hours after chip operations. All animals survived after being sorted through the microfluidic device, and the total number of eggs laid per animal in the manipulated population, 195 ± 6 (mean \pm standard error, $n = 15$), had no statistical difference when compared to a control population, 188 ± 8 ($n = 14$, $p > 0.5$, Student's t -test). Thus, results of the device characterization experiments validate our method to orient animals within a microfluidic chip, and confirm its efficacy for high-throughput applications while having no adverse effects on animal viability or reproduction.

3.3.2 Identification of neurodegenerative and neurodevelopmental mutants using curved channel microfluidic devices

To demonstrate the utility of this simple and easy-to-use methodology, we performed a pilot screen to isolate novel mutants with neurodegenerative and neurodevelopment phenotypes in the D-type motor neurons. We analyzed approximately 10,000 F2 progeny on-chip (~ 1000 haploid genomes), at a consistent rate of 600 ± 45 animals per hour (mean \pm standard error). Throughput was calculated from two separate but identical devices over the course of four days of screening. In wild-type animals, 17 out of 19 of the D-type neurons, which belong to either the DD class (six cells) or the VD class (13 cells), send commissures along the right side of the animal's body (Figure 3A–C)⁹⁵. Therefore, strains expressing the *juIs76* transgene are best inspected when the right sides of animals are closest to the objective, with their dorso-ventral plane parallel to the cover-glass. Examining DD or VD commissures located on the opposite (left) side of the animal body is confounded due to optical artifacts (e.g. scattering by the animal's body tissue). Therefore, commissures were only evaluated for animals loaded into the device with the correct body orientation (right side of body closest to microscope objective). The DNC and VNC were evaluated in all animals positioned laterally, since both nerve cords are visible in this orientation. From this screen, we successfully isolated six independent

mutant alleles (*a070*, *a071*, *a073*, *a074*, *a077*, and *vd029*), which present abnormalities in their GFP-labeled neuronal processes and commissures.

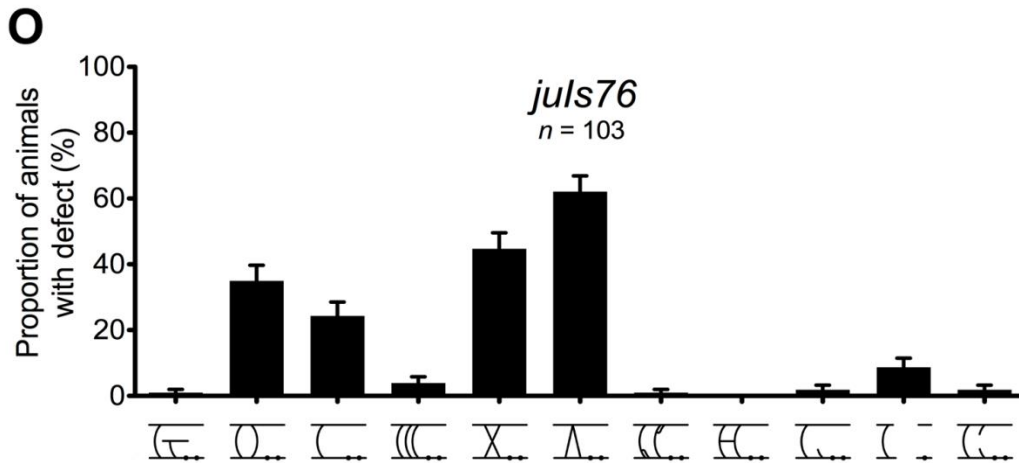
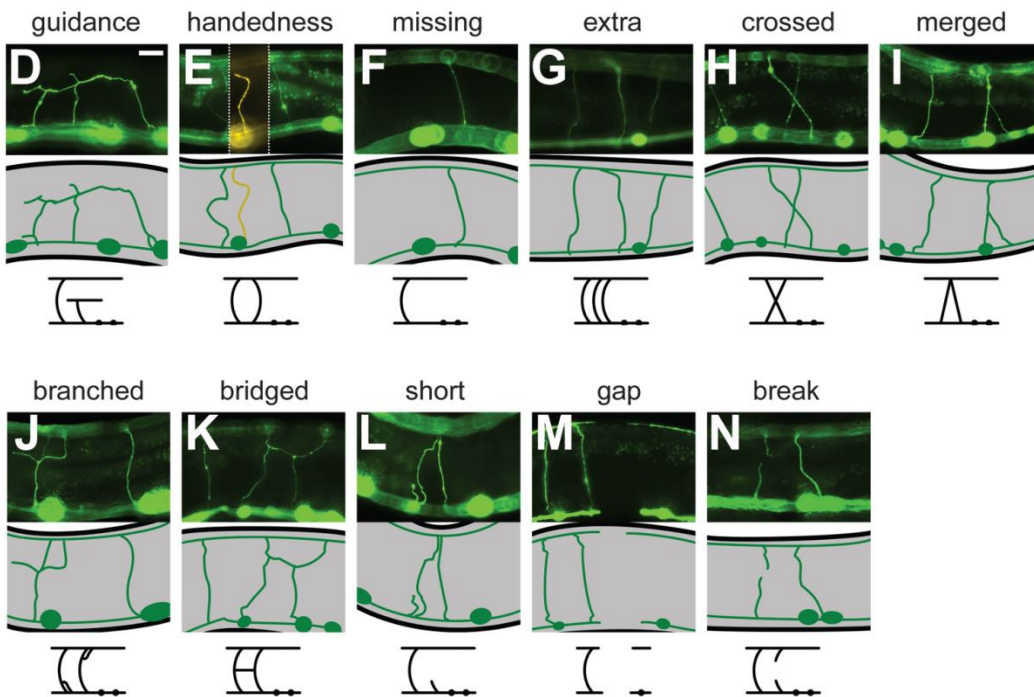
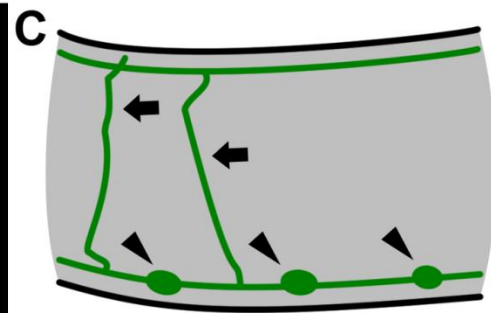
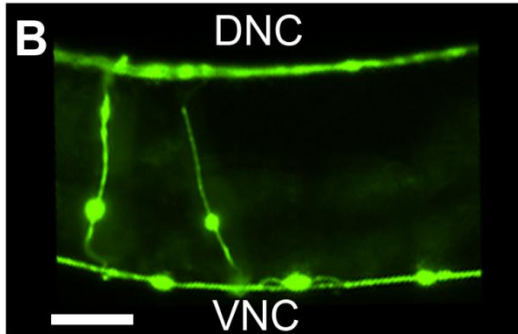


Figure 3. Morphology of wild-type and defective D-type motor neuron commissures. (A) Full body image of adult worm. Scale bar is 25 μ m. (B) Expanded view of area within dashed box in panel A. Ventral nerve cord (VNC) is distinguished by presence of neuronal cell bodies. Dorsal nerve cord labeled DNC. Scale bar is 25 μ m. (C) Representative image of panel B. Black arrows label neuronal commissures while black arrowheads identify neuronal cell bodies. Respective phenotypes characterized by: (D) commissure never reaching dorsal nerve cord; (E) commissure running along the opposite side of the animal's body (left, colored yellow); (F) absent commissure; (G) additional commissure present; (H) two commissures crossing over each other; (I) two commissures entering the dorsal nerve cord or leaving the ventral nerve cord together, they may also partially fasciculate; (J) bifurcating commissure; (K) neighboring commissures joined by a process; (L) neurite with length less than half nematode width; (M) an absence of GFP expression along either dorsal or ventral nerve cords; (N) break in GFP expression in a commissure. Scale bar is 25 μ m. Representative image of phenotype shown beneath each photo accompanied with illustrative phenotype symbol. (O) Proportion of animals in a population with at least one incidence of each independent defect. Error bars represent standard error of proportion.

3.3.3 Phenotype characterization of mutant animals

Following isolation, we further characterized the phenotypic defects of the mutant animals in relation to the commissures of the DD and VD motor neurons. Inspections of these neurons lead to the classification of defects into eleven categories (shown and described in Figure 3D–N), of which the main ones included misguided commissures (guidance), commissures travelling on the wrong side of the body (handedness), lack of commissure (missing), and visible interruptions in the nerve cords (gaps). The frequency of these phenotypes in animals of the wild-type *juIs76* strain is shown in Figure 3O, and data for our isolated mutants is shown in Figure 4 and Figure 27 in appendix A.1. Phenotypes were scored independently of each other, as most mutant animals presented more than one type of defect.

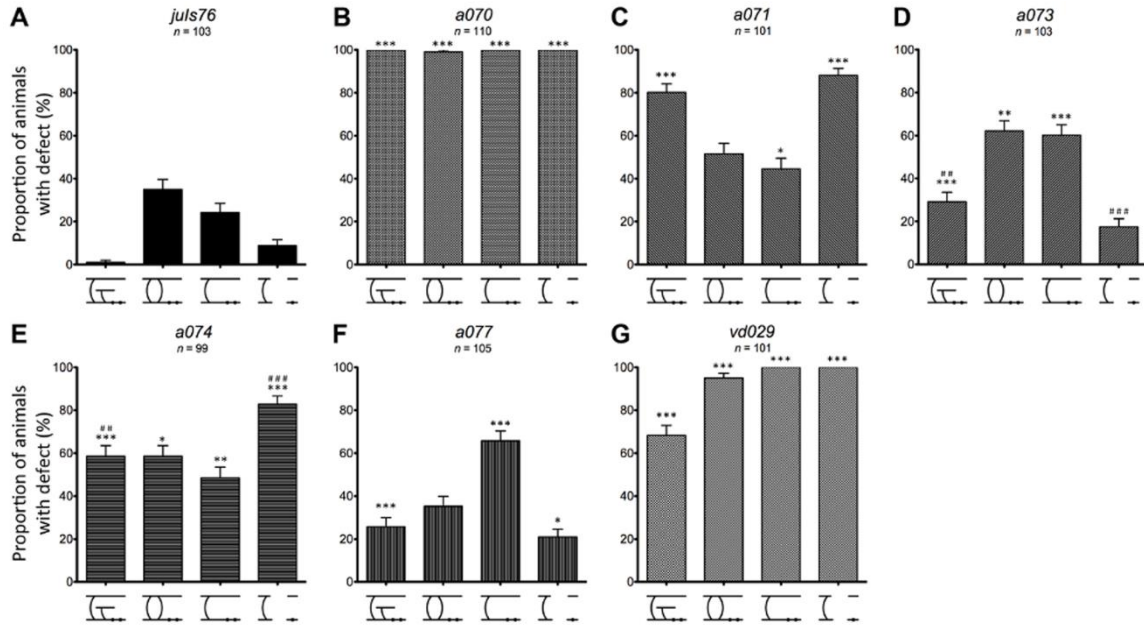


Figure 4. Adult phenotype characterization. (A–G) Proportion of animals in a population with at least one incidence of each of the independent defects: guidance, handedness, missing, and gap for wild-type (*juIs76*) and newly isolated mutants. Asterisks indicate statistical significance of phenotype compared to wild-type. Single, double, and triple asterisks indicate $p < 0.05$, $p < 0.01$, and $p < 0.001$, respectively. Pound signs indicate statistical significance of phenotype compared between *a073* and *a074*. Double and triple pound signs indicate $p < 0.01$ and $p < 0.001$, respectively. Statistical significance determined using chi-squared test. Number of animals examined for each allele labeled in graph. Error bars represent standard error of proportion.

To further characterize the mutants isolated during our visual screen, we investigated the developmental onset and cell-specificity of the observed morphology defects. At the L1 juvenile stage, only the six neurons of the DD class are present, as the remaining 13 VD neurons have not yet developed. This allows the precise identity of each defective DD neuron to be determined, and presents an opportunity to inspect whether the embryonically and post-embryonically developing cells are differently affected. The frequency with which defects occurred in populations of young L1 stage animals is shown in Figures 5 and Figure 28 in appendix A.1, and is assembled by individual cell identity in Figures 6 and Figure 29 in appendix A.1.

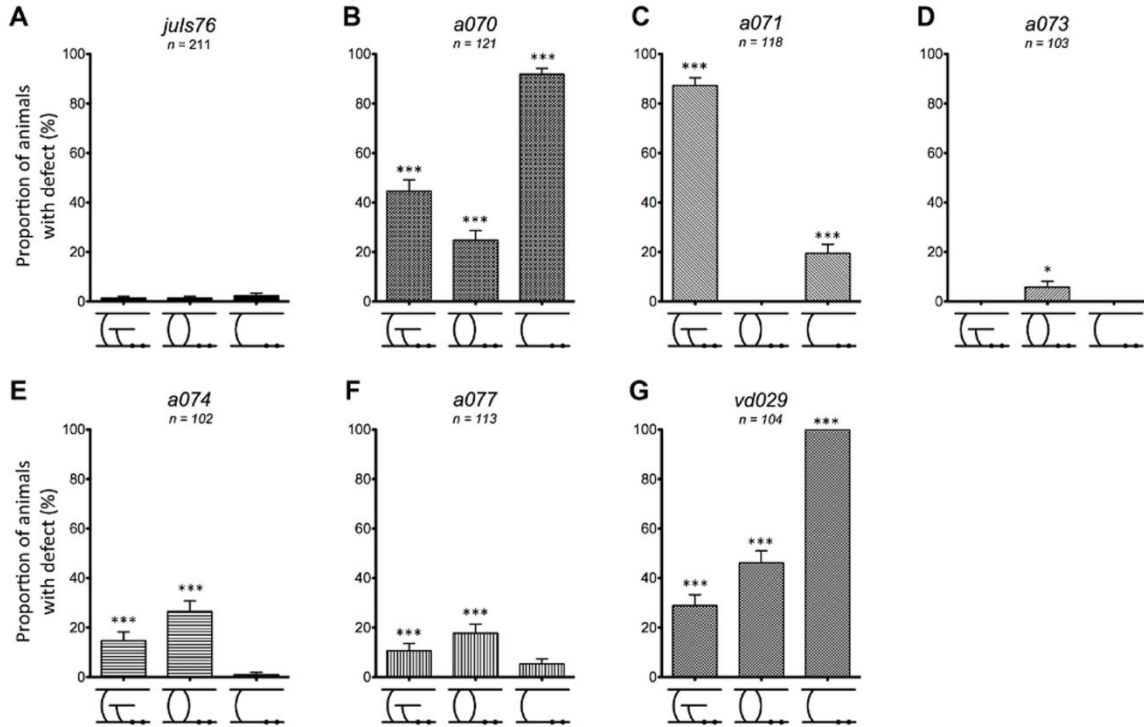


Figure 5. L1 phenotype characterization. (A–G) Proportion of animals in a population with at least one incidence of each of the independent defects: guidance, handedness, and missing defects seen for wild-type (*juIs76*) and newly isolated mutants. Asterisks indicate statistical significance of phenotype compared to wild-type. Single, double, and triple asterisks indicate $p < 0.05$, $p < 0.01$, and $p < 0.001$ respectively. Statistical significance determined using chi-squared test. Number of animals examined for each allele labeled in graph. Error bars represent standard error of proportion.

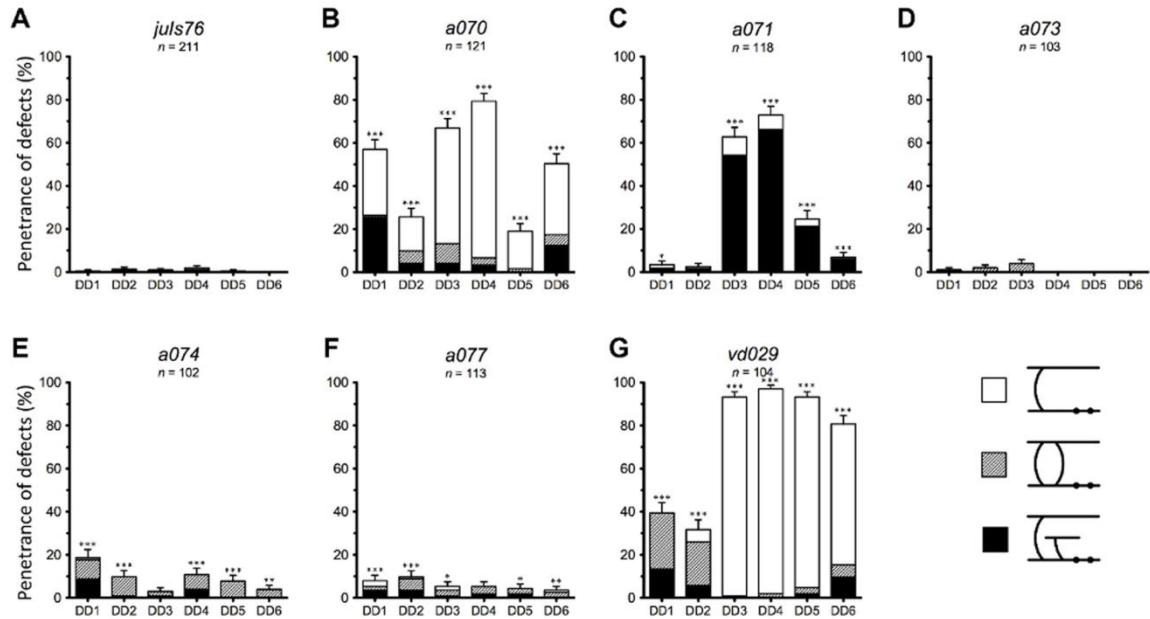


Figure 6. Cell specific characterization for L1 animals. (A–G) Penetrance of defects in each DD neuron for wild-type (*juIs76*) and isolated alleles. Asterisks indicate statistical significance of combined phenotypes per cell compared to wild-type. Single, double, and triple asterisks indicate $p < 0.05$, $p < 0.01$, and $p < 0.001$, respectively. Statistical significance determined using chi-squared test. Number of animals examined for each allele labeled in graph. Error bars represent standard error of proportion for sum of phenotypes per cell.

a070 and *vd029* are the most defective mutants, with a high occurrence of most of the phenotype scored (Figure 4B, Figure 4G, and Figure 27 in appendix A.1). Analysis of the six DD neurons at the L1 stage (Figure 5B, Figure 5G, and Figure 28 in appendix A.1) showed that in *a070* the left-right asymmetry (handedness) defect was strongly reduced (about 20%), indicating that the mutation mostly affected the VD neurons. On the contrary, the missing commissure defect for *a070* was already fully penetrant at this stage (90%), indicating that it affected all the D-type neurons, with the DD3 and DD4 neurons being particularly susceptible (Figure 6B and Figure 29 in appendix A.1). In *vd029*, there was a strong effect on the DD class, with these animals lacking the DD3–DD6 neurons (Figure 5G and Figure 6G), and DD1 and DD2 displaying both handedness and guidance defects.

In *a071* and *a074*, over 80% of the animals presented gaps in GFP expression on either the ventral or dorsal nerve cords (Figure 4C and Figure 4E). While this phenotype correlated with a strong guidance defect (80%) in *a071*, in *a074* the guidance defect was less penetrant. Interestingly, the guidance defect of *a071* was also highly penetrant in the L1 stage with the DD3–DD6 cells presenting this defect (Figure 5C and Figure 6C). On the contrary, L1 animals of the *a074* strain had very minor defects (Figure 5E and Figure 6E), indicating a much later onset and/or selective involvement of the VD neurons.

a077 and *a071* were isolated from the same pooled population of F2s; however, complementation analysis indicated they are not alleles of the same gene (Figure 27 in appendix A.1). Characterization of these two mutants indicated that while guidance and gap defects were both highly penetrant in *a071*, they were only minor in *a077*, which presented a high penetrance of missing commissures instead (Figure 4C and Figure 4F). Even more strikingly, at the L1 stage, the guidance defects in *a071* were at around 85% while only 10% in *a077* (Figure 5C, Figure 5F, Figure 6C, and Figure 6F).

Lastly, *a073* presented handedness and missing commissures phenotypes (Figure 4D), mostly caused by defects in the VD neurons as both these phenotypes were highly reduced in the L1 stage (Figure 5D, Figure 6D).

To confirm that our isolated mutants bred true, we outcrossed each of them with wild-type male animals carrying the *zdis5(Pmec-4::GFP)* transgene as a marker for crossed progeny. We were able to recover the original phenotypes in the F2 generation for all of our strains (Figure 27 in appendix A.1). Additionally, by examining the heterozygous F1 generation we determined that all of our mutations are recessive, with the exception of *a077*, which has a semi dominant effect (Figure 27 in appendix A.1).

3.4 Discussion

We present a microfluidic design capable of orienting *C. elegans* on-chip by using device geometry to position the nematode body into lateral orientations. This alignment

mimics the lateral orientations normally seen during standard analysis of *C. elegans* on agarose pads. The design is comparatively simple to fabricate, requires no extra systems other than pressure sources to operate valves, and can be easily altered to compensate for different body sizes and morphologies if the starting population requires so. We demonstrated the utility and advantages of our technology compared to standard straight channel designs with a high-throughput pilot screen by successfully isolating mutants involved in neuronal development and degeneration. This technology is beneficial to visual inspections of features along the antero-posterior or dorso-ventral body axes. This includes processes and commissures similar to those of the VD and DD neurons, such as in the DA, DB, and AS motor neurons, neuromuscular synapses along both the ventral and dorsal nerve cord, mechanosensory neurons, and other dorso-ventrally aligned body tissues⁹². Our device will thus extend the tools available in *C. elegans* to perform screens to identify genes involved in numerous phenotypes of interest.

The DD and VD motor neurons are ideal cells with which to measure the efficacy of orientation techniques, as their morphology is optimally displayed in laterally oriented worms (Figure 2C), which have commissures curving toward the imaging objective (Figure 2D and Figure 2F). In our curved channel design, GFP expressed in both the ventral and dorsal nerve cords can be seen along the curvature of the microchannel, indicating that the animal is in a lateral orientation, with the dorso-ventral plane parallel to the cover glass. The advantage of this orientation is that it allows for inspection of both the VNC and DNC, in addition to the DD and VD commissures, along the entire length of the animal, presenting multiple opportunities to observe defects in neuronal morphology. In contrast, GFP expression of morphological features of animals viewed in a straight channel device can be out of focus and obscured (Figure 2E and Figure 2F), resulting in concealed portions of connecting commissures, which ultimately makes phenotypic analysis time-consuming and difficult. Another advantage of the curved channel is that the design allows an animal's entire body to be inspected within a single

field of view, while a straight channel design would require multiple fields of view for proper inspection (Figure 2C and Figure 2E).

Analysis of animals during our pilot screen was performed by visually inspecting them on-chip for defects in neuronal morphology. During our screens, we estimate that device operation cycles at about seven seconds, taking into account the entire process of loading, inspecting, and sorting each individual animal. Typically, about two seconds are spent loading each animal into the imaging area, followed by a visual inspection period of up to five seconds. Once the phenotype is determined, the animal is sorted to its appropriate output in less than one second. Taken together, our estimated rate of operation of seven seconds per animal corresponds to a repeatable and measured throughput of over 500 animals per hour.

We isolated over 50 mutants in our pilot screen; however, strains that were sterile or less than 30% penetrant for defects when re-examined were discarded. Conversely, some mutants of interest may have been missed during our screen because they were not fully penetrant. Additionally, we may have discriminated against slow-growing mutants because the growth rate of mutagenized animals varies and we did not include all mutagenized worms in this screen. These artifacts, however, are also present in traditional screens and can be avoided by isolating the F1's and expanding the screened pool of animals⁹⁸.

Characterization of our newly isolated mutant strains revealed correlations between individual phenotypes, which may be indicative of specific biological significance. For example, the low penetrance of GFP interruptions in the dorsal or ventral cords (gap defects) in both *a073* and *a077* (Figure 4D and Figure 4F) suggests that these gaps are not strongly associated with either handedness or missing commissural defects. Furthermore, a comparison of strains *a073* and *a074* (Figure 4D and Figure 4E) show that while similar levels of both handedness and missing commissures defects are seen ($p>0.7$ and $p>0.2$ for each defect, respectively), the penetrance of gaps in GFP

expression along the nerve cords between the two alleles are significantly different ($p < 0.001$). Interestingly, the difference in penetrance of commissural guidance defects between these strains is also significant ($p < 0.01$), suggesting a possible association between highly penetrant commissural guidance defects and the gap phenotype seen in the nerve cords. Alleles *a070*, *a071*, *a074*, and *vd029* similarly display high penetrance of both commissural guidance defects and nerve cord gaps, reinforcing this association.

The phenotypic analysis of L1s allows differentiation between developmental and degeneration phenotypes. For example, alleles *a073*, *a074*, and *a077* demonstrate much lower penetrance of defects when analyzed as L1s than they do as adults. This suggests that while these mutations affect embryonic development, they have an enhanced phenotype at later stages, either due to additional defects that develop post-embryonically or because of aging effects. Secondly, cell specific data reveals the susceptibility of specific body sections to both guidance and missing commissure defects. The majority of highly penetrant defects present for our isolated alleles are concentrated in the animal mid-body or posterior (neurons DD3–DD6), as observed in strains *a070*, *a071*, and *vd029*. This may be indicative of a higher susceptibility to developmental or maintenance defects of these cells or of this entire region of the body.

Like all microfluidic techniques, certain considerations must be taken into account when using this device for specific applications. For example, while our design passively orients animals into lateral positions, our system cannot bias the position of the ventral or dorsal side. Another key point is recognizing that device throughput is ultimately dependent on the user's familiarity with, and the overall complexity of, the phenotype analysis, and to a certain extent user's familiarity with microfluidic devices. Additionally, while we tested animals with body morphology defects using slightly modified designs, extreme body shapes may present complications in device operation (i.e. problems in loading, orientating, and sorting). The advantage of our microfluidic device, however, is in streamlining screening preparation, and worm-handling as it does

not involve mounting animals on slides, waiting for anesthetics to take effect, transporting animals to a microscope for imaging, and careful rescue of the animals from slides, as conventional methods require. Comparatively, our device allows for a single manipulation to load, image, and sort the relevant mutants, requiring only an initial setup time of 20 to 30 minutes before screening.

Results presented here suggest that our microfluidic screening method allows discovery of mutants of interest by exploiting high-throughput techniques to examine large numbers of nematodes in pooled populations. We expect this type of design to be useful in other developmental and functional screens where animals are to be routed and imaged in particular orientations.

CHAPTER 4 AUTOMATED SCREENING OF *C. ELEGANS* NEURODEGENERATION MUTANTS ENABLED BY MICROFLUIDICS AND IMAGE ANALYSIS ALGORITHMS

The following work in this chapter was performed in collaboration with Daniel Porto and Josue Rodríguez-Cordero from the Lu Lab, and Ivan Gallotta, from Dr. Elia Di Schiavi's laboratory at the Consiglio Nazionale delle Ricerche, Italy.

4.1 Introduction

Neuronal degeneration is a fundamental biological phenomena and a characteristic attribute of neuromuscular diseases, which affect as many as 1 in every 3,000 people⁹⁹. One such disease is spinal muscular atrophy (SMA), an autosomal recessive neurodegenerative disorder that is one of the leading genetic causes of infant mortality^{16,100}. SMA results from a loss of function of survival motor neuron protein (SMN) due to mutations in the *SMN1* gene^{101,102}. The decreased SMN function causes specific motor neuron degeneration leading to muscular wasting, paralysis, and even death^{99,100,102}. Although the genetic bases of SMA have been shown to reside in the *Smn1* gene, the molecular mechanisms and pathogenesis leading to SMA remain poorly understood, and currently no effective treatments exist^{88,102}.

Caenorhabditis elegans is a soil dwelling nematode and is an important model used to elucidate the intricacies of complex cellular processes that underlie neurodegeneration. Previous research has used *C. elegans* to study molecular mechanisms behind devastating neuromuscular disorders such as amyotrophic lateral sclerosis, Huntington's, and Parkinson's disease¹⁶⁻¹⁹. The nematode, despite its low level of evolutionary complexity, is particularly well suited for neurobiology research because of the considerable number of conserved molecular pathways between worms and mammals, including major neurotransmitter systems^{1,16}. Furthermore, *C. elegans* have a mapped and comparatively simple nervous system of 302 neurons, unlike other model

organisms that contain thousands to millions of neurons, greatly simplifying analysis of neuronal circuits²⁰. The nematode is also uniquely fit for neurodegeneration research because it is transparent, allowing for the inspection of fluorescently labeled neurons within a living multicellular organism at all stages of development^{1,16,21}. *C. elegans* are also appealing for genetics research due to their ease of genetic manipulation, mapped genome, and large number of genetic homologs to vertebrates^{1,96,103}. For instance, the *C. elegans* genome is 60-80% homologous to human genetic disease genes, such as *smn-1*, a homolog of the human SMN protein^{1,104}. Additionally, the 19 D-type motor neurons along the nematode's ventral nerve cord provide multiple opportunities to study degenerative mutations in a localized area of the animal body.

Currently there are only two well characterized genetic modulators of human SMN, *SMN2* and *PLS3*¹⁰⁵⁻¹⁰⁸. Studies using *C. elegans* to discover additional modulators of SMN have utilized visual inspection to measure pharyngeal pumping rates, custom image analysis methods to measure motility, or the COPAS Biosorter to measure animal body length^{87,88,106,109,110}. These methods, however, either require manual analysis, are comparatively low-throughput, or provide indirect correlations of motor neuron degeneration. The limitations in these systems, therefore, bottleneck the discovery of SMN modulators and ultimately potential therapies for SMA.

Microfluidics can be used to overcome these limitations. By manipulating *C. elegans* in liquid environments in microfluidic chips, throughput gains up to two orders of magnitude are achieved when compared to manual methods of handling³². Additionally, screening of nematodes on-chip can be performed to take advantage of *C. elegans* low cost, rapid life cycle, and large number of progeny^{1,32,40-42,96,111}.

Here, for the first time, we present a fully automated system to identify modulators of neurodegenerative phenotypes using genetic screening techniques. The advantages of our system are threefold. First, our system is fully automated, reducing human bias and subjective analysis from visual screening practices. Second, phenotype

analysis is rapid, performed within 12 seconds per animal on average. Third, we directly inspect the animal nervous system, removing the need for behavioral analysis or indirect correlations to motor neuron degeneration. We demonstrate the utility of our system by performing an automated screen and isolating 21 mutants that rescue the neurodegenerative phenotype seen in *C. elegans* D-type motor neurons due to the absence of *smn-1*.

4.2 Materials and methods

4.2.1 Microfluidic device fabrication and operation

Microfluidic devices were fabricated using standard soft lithography methods to create single-layer chips made from the elastomer polydimethylsiloxane (PDMS, Dow Corning Sylgard 184)¹¹². Master molds were fabricated as in previously work using silicon wafers, SU-8 photoresist (Microchem), and treated with tridecafluoro-1,1,2,2-tetrahydrooctyl-1-trichlorosilane vapor (United Chemical Technologies) to reduce elastomer adhesion to the substrate^{32,40,111}. Likewise, thermal bonding between a thin (~0.5mm) 20:1 and a thicker (~3mm) 10:1 layer of PDMS was used during chip fabrication to facilitate valve flexibility, while maintaining overall rigidity⁴⁰. After cutting and preparing PDMS devices to interface with tubing and pins, chips were bonded to cover-glass using oxygen plasma.

Similar to our previous work, we used partially closed valves and pressure driven flow to route, image, and sort animals within the device^{42,111}. Channel and chip feature height for our presented design is approximately 60 μ m for all areas excluding the curved portion of the flow channel in the imaging area, which is approximately 40 μ m.

4.2.2 *C. elegans* culture, mutagenesis, and phenotype scoring

The *C. elegans* strains used in this study were *juIs76(Punc-25::GFP)* and *gbIs4[Punc-25::smn-1 RNAi sas; Pchs-2::GFP]*;

oxIs12[*Punc-47::GFP*; *lin-15(+)*]. Constructs for *smn-1* RNAi and *chs-2* were injected at concentration of 200 ng/μL and 10 ng/μL respectively for *gbIs4*. These strains were cultured between 15°C and 25°C using established protocols⁹⁶. A standard concentration of the chemical mutagen ethyl methanesulfonate (Sigma Aldrich) was used to mutagenize animals in order to perform a pooled F2 suppressor screen of *gbIs4*, the *smn-1* mutant¹⁰. Animals were screened when most animals reached gravid adulthood in terms of age.

Phenotype scoring of alleles isolated from the automated screen was performed on animals cultured at 20°C anesthetized with 5mM concentrations of sodium azide (Sigma Aldrich) on prepared agar slides⁹⁷. All animals were manually inspected under fluorescence for the presence of D-type motor neurons using 20x/0.4NA and 20x/0.5NA objectives on wide field inverted compound microscopes (Leica DM IRB/E and Leica DMI 6000B); fluorescently labeled DVB, RIS, AVL, and RME neurons were not counted in this analysis. Automated experiments and visual analysis of *C. elegans* were both performed when animals became gravid adults using the same objectives and microscope equipment as mentioned above.

Unless mentioned otherwise, all images are of *gbIs4*, the *smn-1* partial knockdown mutant strain.

4.2.3 Automated system operation

System automation describes the process of autonomously controlling all system components to execute animal loading, imaging, phenotype analysis, and sorting. System setup is similar to our previous work utilizing off-chip components such as pneumatic solenoids, a compound microscope, and a digital CCD camera to control on-chip valves; however, no cooling system was used for immobilization in this study^{32,34,40,42}. A diagram and detailed description of the system operation is shown in Supplementary Figure 1.

Animals were recorded using a 20x/0.5NA magnification objective in fluorescence mode on a wide field inverted compound microscope (Leica DM IRB/E).

Images were captured and analyzed using a using a digital CCD camera (Hamamatsu ORCA C4742-95-12). All image analysis in this work was programmed using MATLAB®.

The presence of animals within the microfluidic device was detected by computing the average pixel intensity of various regions. These regions were user-defined during each experiment and represented background (β), worm (ω), and correct position (ρ) areas within the camera field of view. These regions were selected after loading a worm into the device imaging area by manually operating the microfluidic chip. An animal was considered to have been successfully detected if the average intensity of the worm region satisfied equation 1 below, where α_1 represents an arbitrary weight based on empirical results.

$$\bar{\omega} \geq \alpha_1 \times \bar{\beta} \quad (3)$$

Similarly, after being detected, an animal was considered to be successfully loaded and ready for imaging if the average intensity of the correct position region satisfied equation 2 below, where α_2 represents an arbitrary weight based on empirical results, and $\bar{\rho}_{\text{worm}}$ represents the average intensity of the correct position when a worm was correctly loaded. Animals detected in the correct position region have either their head or tail in close proximity to the end of the imaging area, indicating that the nematode is fully loaded into the curved area of the device.

$$\bar{\rho} \geq \alpha_2 \times \bar{\rho}_{\text{worm}} \quad (4)$$

Loading an animal was performed by sending a command to off-chip solenoids to actuate the on-chip valve configuration and input flow required for positioning. Once an animal was detected in the imaging area of the device by software, it was given a period of four seconds to reach the correct region for image capture and analysis. The system began image acquisition if the nematode was detected in the correct position or if the allotted time had expired.

After image capture, animal phenotype was analyzed to determine the number of D-type motor neurons present using a four step process: (1) images were smoothed using an anisotropic diffusion filter; (2) the smoothed image was segmented for features of interest using global thresholds; (3) potential neurons were filtered by shape and size; and (4) a mean and size filter was utilized to remove objects falsely detected as neurons.

For this study, an animal was considered to be a suppressor of the *smn-1* neurodegenerative phenotype if 10 or more D-type motor neurons were detected within a specified analysis area.

Once image analysis and phenotype classification was complete, the nematode was sorted to the appropriate mutant or wild-type output using off-chip solenoids to actuate the appropriate on-chip valve configuration and activate fluid flow in both the input and flush channel. Once an animal was no longer detected, the entire process of loading, phenotype analysis, and sorting was repeated.

All time limits for system processes were set to values based off of empirical data. All animal detection and phenotype analysis was performed with the microscope in fluorescence mode. System operation and software decisions were executed by polling the status of worm detection software modules at a rate of 30Hz. All system automation software was programmed in MATLAB® in conjunction with Micro-Manager¹¹³.

4.3 Results and discussion

4.3.1 Microfluidic device performance

All genetic screening experiments were performed on-chip using the single-layer microfluidic device shown in Figure 7A. Previous work has shown the potential of microfluidics for vastly improving the throughput of imaging, sorting, and genetic screening studies involving *C. elegans*^{32,40,42,111}. The presented design was adapted from previous work using curved geometries to passively position animals into lateral

orientations for improved inspection and imaging¹¹¹. This orientation method is particularly advantageous when inspecting objects along the ventral nerve cord, such as the D-type motor neurons.

Our current design has two improvements from our previous work. First is the introduction of a partial immobilization method using compressive force from actuated valves (IMM in Figure 7A-B) to limit animal movement during image acquisition. This method allows for improved image quality while maintaining overall ease of device fabrication. Second is the use of a single-layer design which as shown in previous work, maintains compatibility with on-chip valves while greatly simplifying standard multi-layer fabrication techniques^{35,40}.

To ensure that animals were not obstructed by the use of partial immobilization valves (Figure 7C-F), we introduced a height decrease in the flow channel of the imaging area (Figure 7E-G). With this height difference, valve obstruction of animal body regions dropped significantly in frequency as animals were more likely to stay close to the cover glass (Figure 7D).

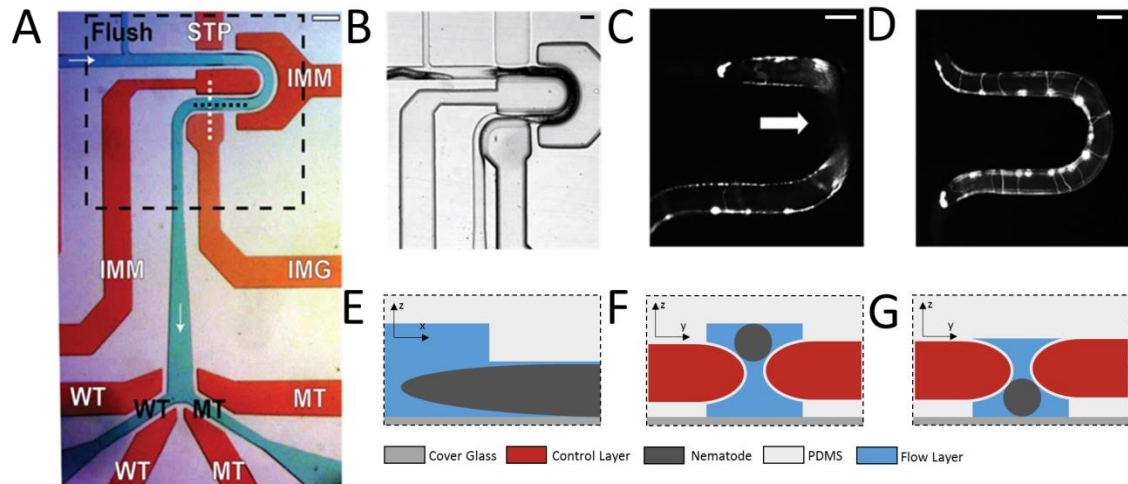


Figure 7. Single layer microfluidic device. (A) Device used for on-chip characterization and automated sorting of *C. elegans*. Flow layer is shown in green with black text, valve control layer shown in red with white text. Fluid flows from left to right, top to bottom, and is marked by white arrows. Flush channel, wild-type (WT), and mutant (MT) channels are all labelled. STP is the stop valve, IMM are

the immobilization valves, IMG is the imaging valve, and WT and MT are the wild-type and mutant valves. Imaging area shown with dashed black box. White and black dashed lines show locations of device cross sections shown in panels E-G. Scale bar is 200 μm . (B) Imaging area shown in panel A demonstrating valve expansion into flow layer. Actuating the valve control layer simultaneously routes fluid flow and obstructs animal passage during device operations such as loading (shown) and imaging. Scale bar is 70 μm . (C) Example image of an animal body obstructed by immobilization valves. Device used for this image does not have a height difference in the imaging area. White arrow indicates area obscured from camera. (D) Example image of an animal body not obstructed by immobilization valves. Device used for this image does include a height difference in the imaging area. Animals shown in panels B-D are *juIs76*. Scale bar for panels B-D is 70 μm . (E) Diagram illustrating the height decrease along the cross section of the black dashed line shown in panel A. (F-G) Illustrations of device cross sections along white dashed line in panel A without a height decrease in the fluid layer (F), and with a height decrease (G). Panel F demonstrates the case that without a height decrease, immobilization valves have a greater chance of obstructing the animal body during imaging. Panel G demonstrates that with a height difference, however, animals are more likely to stay closest to the cover glass, resulting in better image quality. Images (E-G) are not drawn to scale.

4.3.2 Manual screen for suppressor mutants

To verify our ability to find suppressors of the *smn-1* mutation, we performed a manual pilot screen of ~1,000 animals using our microfluidic system. To this end we used a strain in which the function of *smn-1* is selectively reduced in D-type GABA motor neurons (referred to as neurons henceforth) using a neuron-specific RNAi method (Figure 8A). The silencing of *smn-1* in these neurons induces their degeneration, detectable as the disappearance of GFP expression (Figure 8B). A mutated population of *smn-1* (Figure 8B-C) were loaded and visually inspected on-chip to search for animals with a high number of neurons. From this screen, we isolated allele *a205* (Figure 8D-E), which displayed a statistically significant difference in neuron number when compared to our *smn-1* partial knockdown mutant, 13.8 ± 2.7 versus 9.3 ± 2.8 for *a205* ($n=54$) and *gbIs4* ($n=60$) respectively (Figure 8F, population average \pm standard deviation, $p < 0.0001$, *t*-test). All animals were inspected as gravid adults as age-associated neurodegenerative diseases in humans demonstrate similar age dependence in many *C. elegans* transgenic models¹¹⁴.

While the average number of neurons provides some information about the differences between these populations, further insight can be obtained from analyzing the numerical distribution of neurons present for each allele. For example, inspecting the histogram data for *gbls4* and *a205* (Figure 8G) reveals the amount of phenotypic overlap between alleles, which can be masked when only considering mean and standard deviation values between populations. Thus, while it doesn't occur with high frequency, there are instances where *gbls4* expresses an *a205* phenotype, or vice versa, due to natural variations within the population.

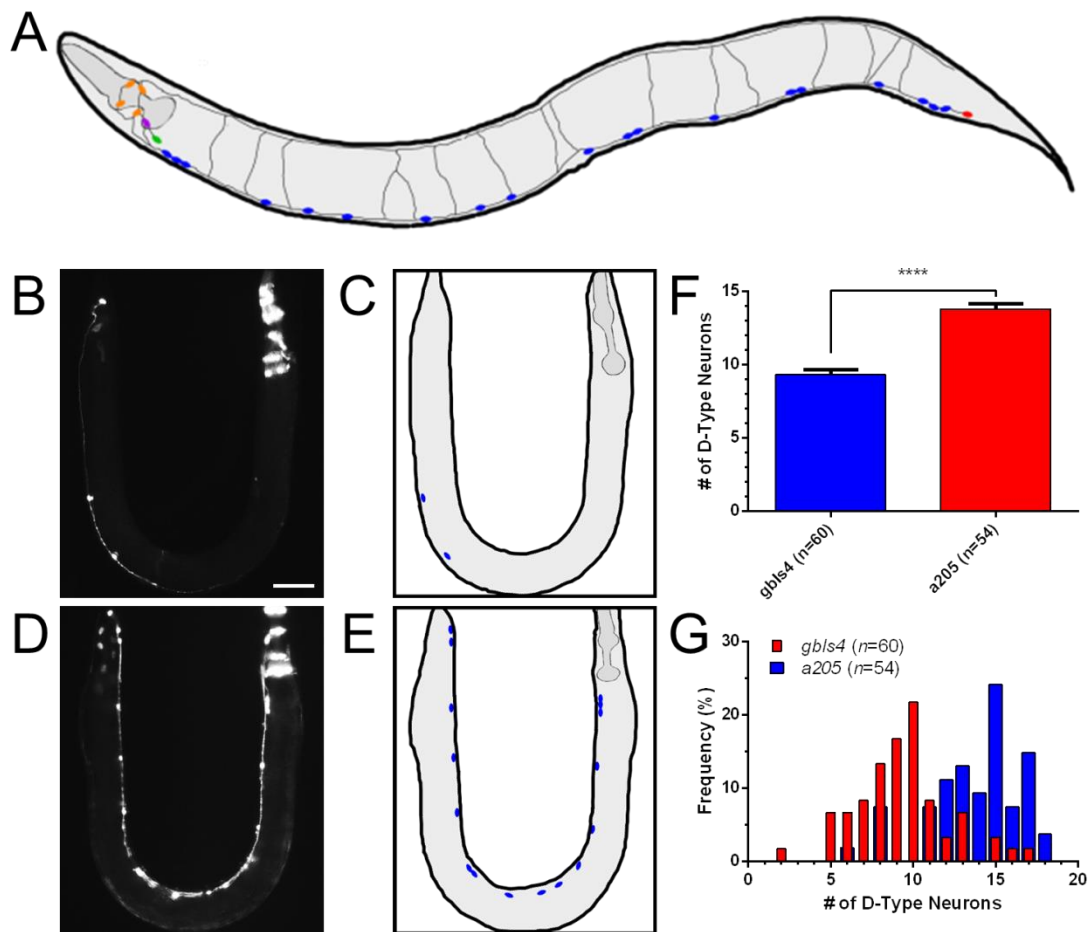


Figure 8. Suppressor of *smn-1* phenotype from manual pilot screen. (A) Representative image of adult worm and neurons labeled by *oxIs12* transgene. D-type motor neurons shown in blue. Image not to scale. (B) Image of *smn-1* mutant, *gbls4*, with 2 of 19 visible D-type motor neurons. (C) Diagram of image shown in panel B. (D) Image of allele *a205* with 16 of 19 visible D-type motor neurons. Scale bar for panels B and D is 70µm. Images B and D captured using microfluidic device

shown in Fig. 1A. (E) Diagram of animal shown in panel D. D-type motor neurons shown in blue for C and E, RME & DVB neurons not shown. (F) Average number of D-type motor neurons present in alleles *gbIs4* (n=60) and *a205* (n=54). Error bars represent standard error of mean. Asterisks indicate significance ($p < 0.0001$, t-test). (G) Histogram demonstrating differences between motor neuron distributions within the two allele populations.

4.3.3 Software design and validation

Upon the discovery of a suppressor mutant, allele *a205* was used for the creation of custom neuron detection software. Figure 9A demonstrates the background (β), worm (ω), and correct position (ρ) areas used for detecting an animal within the imaging area of the device. This method utilizes average intensity thresholds of each region to scan for the presence of nematodes and is described in further detail in the methods' system operation section. Figure 9B-3F displays the step by step process of discovering neurons while minimizing the detection of false positives such as miscellaneous image artifacts or fluorescent co-injection markers, present in both the head and tail of the animal. We verified the effectiveness of this method by hand-selecting neurons from a set of high quality images and compared them with our software results. Allele *a205* was used in place of *gbIs4* because we are interested in isolating similar phenotypes with a comparatively high number of neurons from suppressor screens (14 neurons on average for *a205* versus 9 for *gbIs4*).

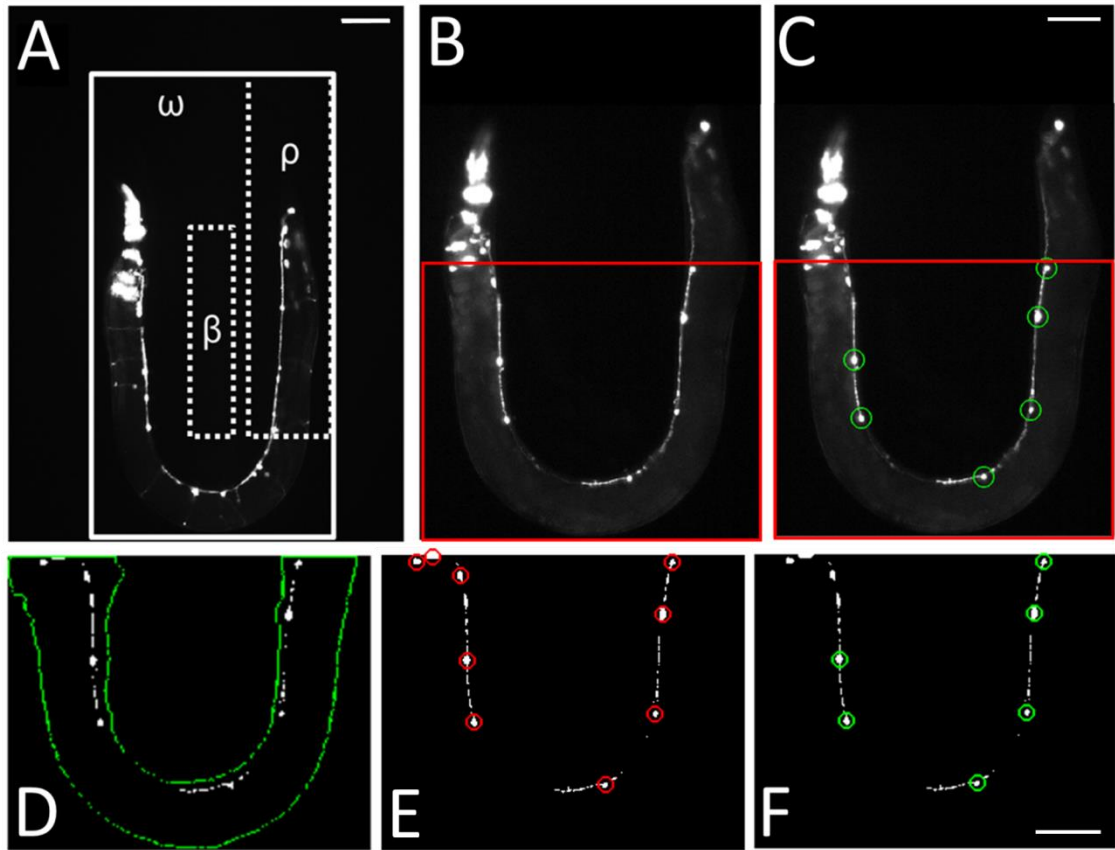


Figure 9. On-chip image analysis for system automation. (A) Image of animal taken on-chip with example background (β), worm imaging (ω), and correct position (ρ) regions marked. Solid line borders ω , while dashed boxes show β and ρ . The mean intensity for all pixel values within each region are calculated and used to determine status of system through equations (1-2). Scale bar is $70\mu\text{m}$. (B) Representative zoomed in image of ω in panel A. Different animal shown. (C) Results of image analysis. Detected D-type motor neurons circled in green. Red box in B-C marks analysis area. Only the analysis area is processed during system operation in order to reduce the number of false positive D-type motor neurons detected due to head and tail co-injection markers. Scale bar for B-C is $70\mu\text{m}$. (D) Segmentation of key features using empirically determined global thresholds. Worm body outline is shown in green while detected objects are shown in white. Objects detected outside of worm body are discarded. (E) Size and morphology filtering to isolate detected neurons. Segmentation results from D shown in white. Results from size and morphological filtering circled in red. (F) Mean filtering used to remove false positive detection of D-type neurons. Remaining objects after all image analysis processes shown circled in green. Scale bar for figures D-F is $70\mu\text{m}$.

Using these images, we found that our software algorithm was capable of correctly identifying 87% of fluorescently labelled motor neurons in our image library (448 correctly identified out of 513 determined visually, 56 total images). The amount of false positives, or objects detected by our program that were not actually neurons was 8% (39 of all 487 objects detected); while the amount of false negatives, or actual neurons that were not detected by our software, was 13% (65 of 513 visually determined neurons). The average number of false positives and false negatives per image were 0.7 ± 0.8 and 1.2 ± 1.3 respectively (mean \pm standard deviation, $n=56$).

Reviewing segmented neurons from our image library reveals that most false positives are due to mistaking puncta, RME or DVB neurons, or RNAi co-injection markers for D-type motor neurons. Size filters in our custom software reduce the number of puncta and RME neurons detected by removing objects too small or too large to be considered D-type neurons. However, a careful balance must be maintained when setting size thresholds as altering ranges to decrease false positives can simultaneously increase the number of false negatives, resulting in actual neurons not meeting requirements for detection. In this work, size thresholds were determined from empirical results and set to values to minimize the amount of both false positives and negatives.

To further decrease the number of false positives, we limited image analysis to the area labelled in red in Figure 9B in combination with a mean filter. Image analysis was reduced to the mentioned area due to the observation that curved device geometry places head and tail regions in the same image section. Therefore, removing these areas from analysis decreases the risk of detecting false positives in head and tail regions which contain RME and DVB neurons, as well as RNAi co-injection markers. To compensate for occurrences when the head area of the animal is within our analysis region, we use a mean filter to combine and remove any objects within close proximity of each other that are falsely detected as neurons. While the head region of animals are the most prone to detection of a high number of false positives (Figure 10A-B), this can also occur due to

animals with egg laying deficiencies (Figure 10C-D), or due to multiple animals within the analysis region (Figure 10E-F).

False negatives detected in our sample image library can be attributed to neurons not meeting minimum or maximum size threshold requirements. These instances occur when neurons are too small due to natural variation between animal expression and size, or too large due to diffused light from out of focus neurons. Images captured for analysis within our device are captured at a single focal plane in order to expedite analysis and keep device operation simple by not requiring an immobilization scheme.

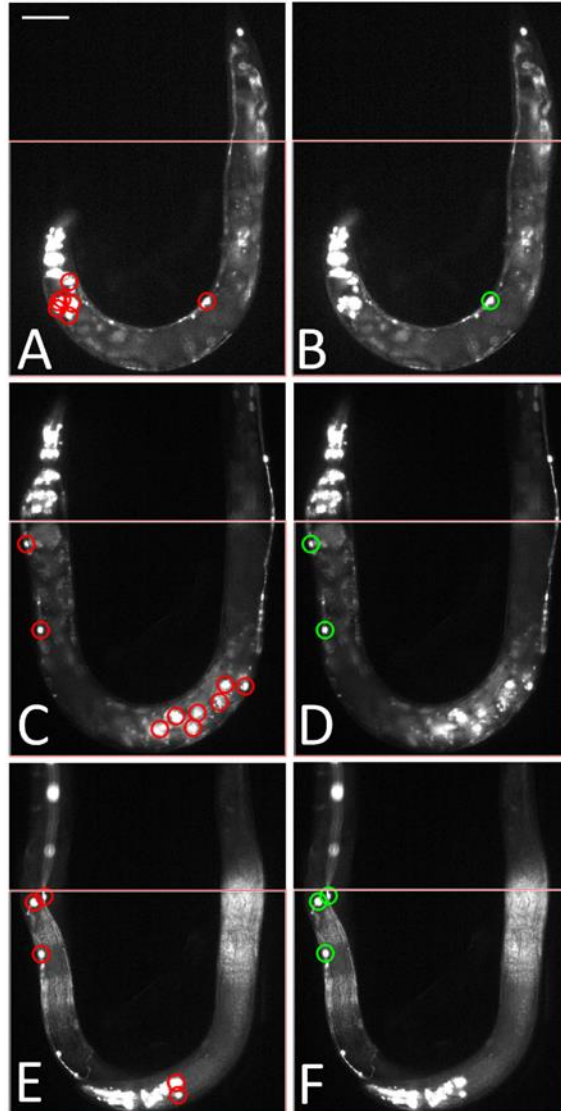


Figure 10. Application of mean-filter to remove false positives. (A) Image of randomly mutated *smn-1* animal loaded on-chip with the head region present in the analysis area. RNAi co-injection markers not removed by previous analysis steps are falsely detected as neurons, labelled in red. (B) Results of mean and size filter to remove false-positives from panel A. Objects that were previously detected in the head region have been removed. Remaining neurons shown in green. (C) Image of randomly mutated *smn-1* animal loaded on-chip demonstrating egg laying deficiency. Fluorescent markers of progeny within parent falsely detected as neurons and labeled in red. (D) Results of mean and size filter, objects previously detected within the animal body removed. Remaining neurons shown in green. (E) Example of multiple animals within the imaging area. Falsely detected neurons from the head one one animal are detected along with neurons from the other animal's body. All objects detected shown in red. (F) Results after applying mean and size filter

to remove RNAi co-injection markers seen in head of worm. Remaining neurons shown in green. Scale bar in panel A is 70µm.

4.3.4 Automated screen for suppressors of *smn-1* mutation

To test the ability of our system to successfully identify and sort suppressors of the *smn-1* phenotype (referred to as double mutants from this point forward), we performed an automated pilot screen of over 7,500 animals investigating a minimum of (~750 haploid genomes), isolating approximately 66 potential double mutants. Our average screening rate was approximately 300 animals per hour, calculated over 8 trials on different days, and utilizing multiple microfluidic devices of identical design. All animals were imaged and analyzed using a single focal plane on-chip, determined manually at the beginning of each screen. Similarly, analysis regions for automated worm detection were manually selected at the beginning of each automated screening experiment.

A threshold limit of 10 neurons was used during neuron detection to classify potential suppressors of *smn-1* phenotype. This threshold was determined in order to compensate for the removal of six neurons from the image when limiting detection to the analysis area (performed to decrease the number of false positives).

Of the double mutants detected and sorted by our automated system, 65% were visually verified as double mutants, containing 10 or more neurons within the analysis area ($n=26$ of 40 total). This analysis, however, takes into account animals sorted before the implementation of a mean filter to reduce the number of false positives in neuron detection. Analyzing all sorted animals with implementation of the mean filter increases the sorting accuracy of our system to approximately 85% ($n=56$ classified correctly of 66 total, including previous 40).

Many factors can lead to classification errors during automated phenotype analysis due to the random nature of forward genetic screens. Differences in body size (affecting head position), loading of multiple worms into the imaging area, or animals

with progeny that have hatched inside of them compound analysis, normally requiring individual software solutions specific for each circumstance. However, using a mean filter as the final step in neuron detection provided a single solution for these issues while increasing the sorting accuracy of our system 20%.

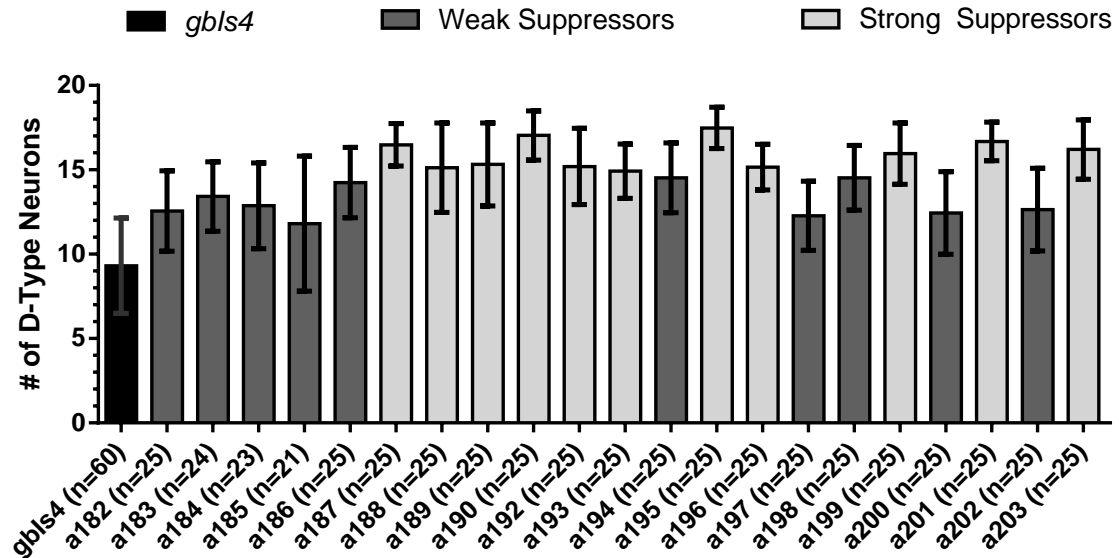


Figure 11. Average number of D-type motor neurons per allele. Error bars represent standard error of mean. *smn-1* single mutant shown in black, isolated alleles shown in grey. Lighter grey designates alleles considered to be strong suppressors of the *smn-1* corresponding to 95% confidence interval of allele *gbls4*. Only data from manual scoring, not image analysis, used for this figure. Error bars represent standard deviation.

4.3.5 Characterizing isolated alleles

From our potential pool of 66 double mutants, we visually inspected and scored each population lowering our final result to 21 suppressors of the *smn-1* phenotype (Figure 11), isolated from eight different pooled populations. A table of the number of neurons for each isolated allele is listed in Supplemental Table S1. All double mutants were found to be statistically different when compared to the *smn-1* single mutant *gbls4* ($p < 0.0001$ for all alleles except *a185*, which is $p < 0.001$, one-way ANOVA Dunnett's post-test).

For the purpose of this study, we considered strong suppressors of the *smn-1* phenotype to have an average of approximately 15 neurons for their respective

population. This number was chosen because it corresponds with the 95% confidence interval of allele *gbIs4* (mean + 1.96 × standard deviation). Using this measure, we find that 11 of the 21 isolated alleles are strong suppressors of the *smn-1* phenotype (*a187-a190, a192, a193, a195, a196, a199, a201, a203*). Allele *a195* is the strongest suppressor demonstrating a near perfect rescue of the neurodegenerative phenotype with 17.5 ± 1.2 neurons on average of the possible 19 (mean ± standard deviation).

Figure 12A demonstrates the cumulative distribution functions (CDF) for all isolated double mutants which can be used to visualize the differences in numerical distributions between alleles. Analyzing the CDF can provide a measure of how effective the allele is at suppressing the neurodegenerative phenotype of *gbIs4* in a whole population. The farther right shifted the distribution function is, the more effective the suppression. Visualizing data in this manner similarly provides further insight about alleles isolated from the same pooled population, revealing similarities and differences in phenotype between potential siblings.

The CDF for alleles *a194-a198* and *a202-a203* are shown in Figure 12B and display varying levels of *smn-1* rescue for strains isolated from the same pooled population. A histogram of three representative alleles from this group is shown in Figure 12C and reveals a comparatively small amount of overlap between each double mutant, demonstrating unique phenotypes among potential siblings. We present these comparisons to illustrate that our system is capable of capturing animals with varying levels of *smn-1* rescue, and not limited to only strong suppressors of the neurodegenerative mutation. Histograms for alleles isolated from the same pooled population that are not shown can be seen in Supplemental Figure 31-Figure 34.

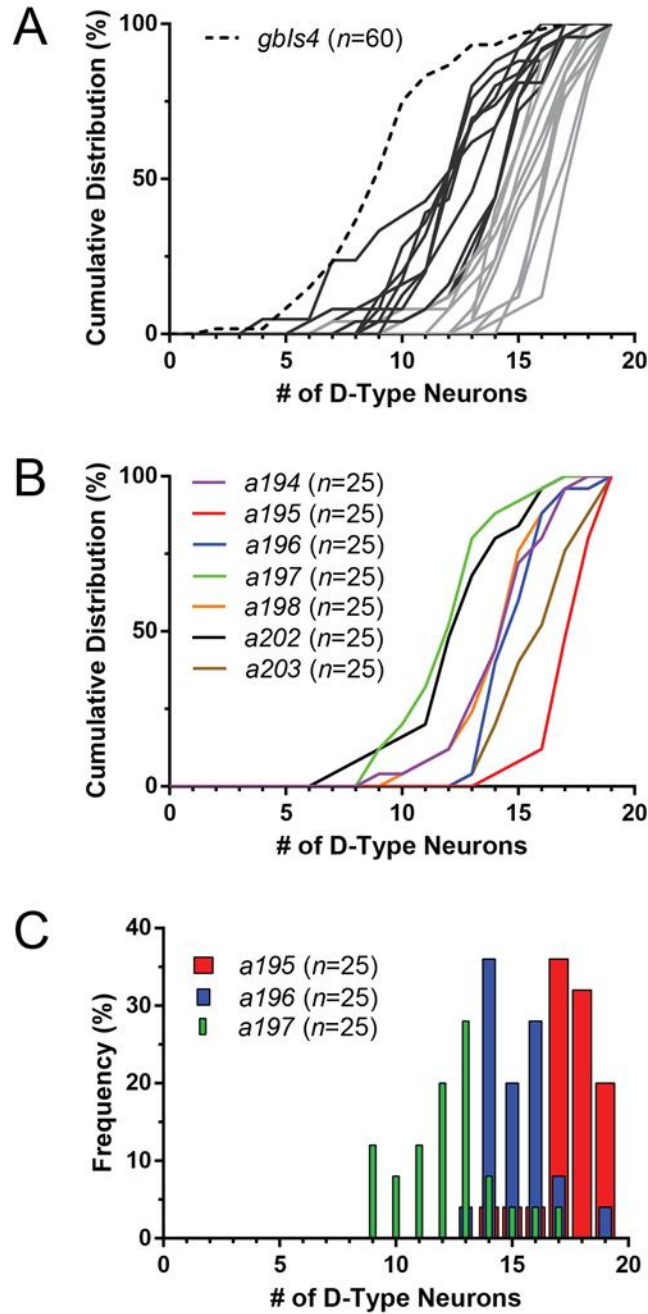


Figure 12. Characterization of isolated alleles. (A) Cumulative distribution functions (CDF) for isolated alleles from automated suppressor screen. *smn-1* mutant (*gbls4*) shown in dashed black line, double mutant alleles in grey. Lighter grey designates alleles considered to be strong suppressors of the *smn-1* phenotype. (B) CDFs for seven alleles isolated from same F1 parent population (possible siblings). (C) Histogram for alleles *a195*, *a196*, and *a197* shown in panel B. Only data from manual scoring, not image analysis, was used for this figure.

4.4 Conclusions

We present an automated system to perform suppressor screens aimed to identify novel modulators of *smn-1* neuronal degeneration. Using comparatively simple microfluidic designs and image analysis methods, we are capable of performing these screens at a consistent rate of 300 worms per hour, approximately 100 times faster than standard methods. Additionally, we provide a system capable of directly examining motor neurons within *C. elegans* to characterize degeneration. We demonstrate that our software analysis is selective by sorting approximately one percent of the 7,500 animals screened, and validate our classification algorithm accuracy of 85% through visual analysis of sorted double mutants.

Using our microfluidic system and software in concert, we successfully isolated 21 alleles suppressing the *smn-1* neurodegenerative phenotype. To our knowledge, this is the first implementation of an automated genetic screen for neurodegenerative mutants. Our system is versatile, using simple and widely available image analysis techniques, and can easily be adapted to search for neurodegenerative mutants instead of suppressors with minimal changes.

We therefore provide a method to saturate screens searching for genes that modulate neurodegeneration. By elucidating the molecular mechanisms and pathways that cause neurodegenerative diseases, we can potentially discover new treatments for various neurological and neuromuscular pathologies, not limited to genes that only influence *smn-1* or SMA.

CHAPTER 5 HIGH THROUGHPUT CHARACTERIZATION OF SPHERICAL OBJECTS USING MODIFIED GRANULOMETRY ALGORITHM FOR RAPID CHARACTERIZATION OF *C. ELEGANS* LIPIDS

The following work in this chapter was performed in collaboration with Maria Elena Casas and Daniel Porto from the Lu lab and Dr. Ho Yi Mak's laboratory at Stower's Institute for Medical Research and the Hong Kong University of Science and Technology, China.

5.1 Introduction

While performed instantaneously and effortlessly by people and animals alike, object recognition remains a highly complex computational problem. Variations in object shape and size, non-uniform intensity, low signal-to-noise ratio, and occlusion are all contributing factors to the complexity of the process⁶⁰. Images and instances requiring detection and analysis of a large number of objects compound these issues even further. In the field of biological image analysis, these circumstances are a frequent and common occurrence and are pivotal issues limiting large-scale screening, rapid analysis, and rapid characterization technologies.

Segmentation algorithms have been widely used in biological image analysis problems for applications in, but not limited to large-scale screening of cellular phenotypes, nuclei characterization, neuron detection and process tracing, real-time genetic screening, laser surgery, behavior analysis, disease detection, lineage tracking, and MRI analysis^{32,34,40,46,60,70,71,89,115-120}. Common methods include global and local thresholding, edge detection, watershed implementations, machine learning, template matching, active contour and snake algorithms, image transforms, and Gaussian mixture model techniques^{60,71,115,119,120}. Measurements of objects segmented using these methods,

however, are only as good as the precision of the segmentation method itself., Segmentation algorithms are becoming less relevant as the field of biological image processing moves toward high content applications as binarization of many objects is difficult due to size variation and high degrees of object occlusion.

Granulometry, a morphological processing algorithm, provides an opportunity to analyze and characterize images that are difficult for segmentation methods to process¹²¹. Morphological image processing uses structuring elements to filter or quantify images based on how structuring elements fit (or do not fit) with objects in the image⁸⁴. Granulometry algorithm is analogous to the repeated sieving of grains or particulate, where mesh shape and size corresponds to the structuring element used for the operation. As the mesh size is repeatedly increased, larger particles are removed until eventually nothing is left. Similarly, granulometry uses a series of morphological opening operations with structuring elements of increasing size to filter objects from an image. As objects are removed, the resulting loss in pixel intensity from the image is computed, allowing the algorithm to quantify information about various sized objects without the need to segment foreground from background pixels, and simultaneously mitigating the effect of occluded objects.

As explained throughout this thesis, the model organism *Caenorhabditis elegans* can be used to study complex biological problems. One of these problems is lipid metabolism and storage. Lipids that accumulate fat are stored in the intestinal and hypodermal cells of *C. elegans* and are commonly studied as they are essential components to fat storage with highly conserved genes and proteins that help make, metabolize, and transport fat^{122,123}. The lipid droplets take the shape of spheres and they are distributed in 3D, which makes the image processing, particularly the segmentation process, extremely difficult and inefficient. Current imaging and analysis methods for studying lipids requires many manual operations to annotate hundreds to over a thousand individual lipid droplets, making the current analysis standard low throughput, very labor

intensive, and prone to human error¹²⁴⁻¹²⁷. These issues stunt the potential for growth, exploration, and attainable knowledge in the research area.

In this work, we demonstrate a modified granulometry algorithm to estimate the size distribution of lipid droplets in *C. elegans*. The algorithm can be applied to various applications by adjusting the size and shape of structuring elements used during the process. Using this approach, we demonstrate computational accuracy by replicating literature results for known lipid size distributions and show that our method can be applied to low resolution images acquired from epi-fluorescent microscopes.

5.2 Materials and Methods

5.2.1 *C. elegans* culture, mutagenesis, imaging, and manual lipid characterization

The strains utilized in this study were: *hjsi56[vha-6p::3xFLAG-TEV-GFP::dgat-2::let-858 3'UTR]* IV;

hjsi224[vha-6p::dhs-3a cDNA::GFP-TEV-3xFLAG::let-858 3' UTR]; and *dhs-28;hjsi3(R01B10.6::GFP)*. Strains were cultured and maintained on agar plates grown at a temperature of 20°C using established protocols⁹⁶. A standard concentration of ethyl methanesulfonate (Sigma Aldrich) was used to chemically mutate *hjsi224* animals to perform a F2 suppressor screen of the atlastin lipid mutant, *a015*¹⁰.

Manual characterization of *C. elegans* lipids utilized the software program Imaris 6.2.1 for 3D reconstruction, lipid diameter measurements, and lipid intensity analysis. Lipid characterization was performed for Klemm *et al.* and was used in this work for comparison to results from custom software analysis. Imaging for manual lipid analysis was performed using a spinning disk confocal microscope (Ultraview, Perkin Elmer) and digital CCD camera Orca-R2, Hamamatsu) controlled through the Volocity software (PerkinElmer) as described in Klemm, *et al.*. Images of multiple focal planes were acquired during imaging using a step distance of 0.25µm for a total distance of 8µm.

On-chip imaging of animals for genetic screening was performed using a custom built epi-fluorescent compound microscope with a digital CCD camera (Luminera Xfinity-3) and a 100x/1.25NA Plan Achromatic objective (PA100X). Animals were anesthetized using a 35mM concentration of tetramisole which was also used as the buffer solution during device operation. Images were acquired on-chip using a step distance of 1 μ m for a total distance of 40 μ m.

All animals whether screened in device or imaged manually were inspected during their L4 stage of development.

5.2.2 Synthetic image creation and software validation

Synthetic images were created in MATLAB® using disk shaped structuring elements of two, five, and ten pixels. The number of objects for each size was determined so that the total area between all three object sizes was kept equal. Additionally, object location and intensity (where specified) was randomized in order to create a set of 100 unique images for our testing library. While random, location was constrained to prevent object overlap with one another. Similarly, intensity values for lipids were constrained between one and 255 and were kept uniform throughout each individual object. Object area was calculated using the total number of pixels contained in the respective structuring element used to create it.

Bead images were created by preparing standard microscope slides using varying concentrations of 1.019 \pm 0.032, 2.063 \pm 0.067, 4.358 \pm 0.113 μ m sized beads (Fluoresbrite® Fluorescent Microspheres, Polysciences, Inc.). Beads were fluorescently labeled with GFP. Bead sizes were measured by hand during software validation to determine true values for the quantity of lipids and lipid distribution profile respectively. Only sizes corresponding to relevant biological ranges were used for synthetic images or bead analysis.

5.2.3 Analysis of nematode lipid distribution

Lipid droplet analysis was performed off-chip and on-chip for confocal and epi-fluorescent microscope images respectively. Size distribution for images was determined using a four step process involving image stack conversion and preprocessing, granulometry, size analysis, and normalization. All structuring elements used for morphological operations in this study were flat and disk shaped; all image analysis software was programmed in MATLAB®.

Confocal nematode images analyzed in this study were identical to manually evaluated images used in Klemm, *et al.*.

5.2.3.1 Image stack conversion and preprocessing

Before preprocessing, acquired images stacks were converted to a single 2D image using the maximum intensity projection of captured focal planes. The converted image was then doubled in size using 2x2 bilinear interpolation and smoothed using an anisotropic diffusion filter (released in the public domain by David Lopes and available for download on MATLAB® Central File Exchange: <https://www.mathworks.com/matlabcentral/fileexchange/14995>). Following smoothing, the image was processed using both top-hat and bottom-hat morphological operations; the bottom-hat transformation was subtracted from the sum of the top-hat transformation and the smoothed image. Both operations were performed using a structuring element size of 30 pixels, determined from empirical results. Next, image intensity of the processed image was adjusted using contrast-limited adaptive histogram equalization. This result was contrast adjusted once again to saturate one percent of both low and high intensity values before filling in holes in the image. Holes in this instance refer to dark pixel regions surrounded by lighter pixels.

5.2.3.2 Granulometry algorithm

Granulometry is performed on preprocessed images using standard methods^{83,121,128}. The normalized size distribution, $\Phi(\kappa)$, follows equation (5) below

$$\Phi(\kappa) = \frac{v[I] - v[I \circ \lambda_\kappa]}{v[I]} \quad (5)$$

where I represents the preprocessed image, v denotes the area or volume computed by taking the sum of all pixel intensities, \circ is the morphological opening operation, λ is the disk structuring element used for morphological processing, and κ is the radius size of the structuring element ($\kappa \in [1, 2, \dots, 29]$). The normalized size density or pattern spectrum, $d\Phi(\kappa)$, is approximated from the difference of $\Phi(\kappa)$ for each λ_κ , and is seen in equation (6) and.

$$d\Phi(\kappa) \approx \Phi(\kappa + 1) - \Phi(\kappa) \quad (6)$$

An example image of the granulometry process is shown in Figure 13 below.

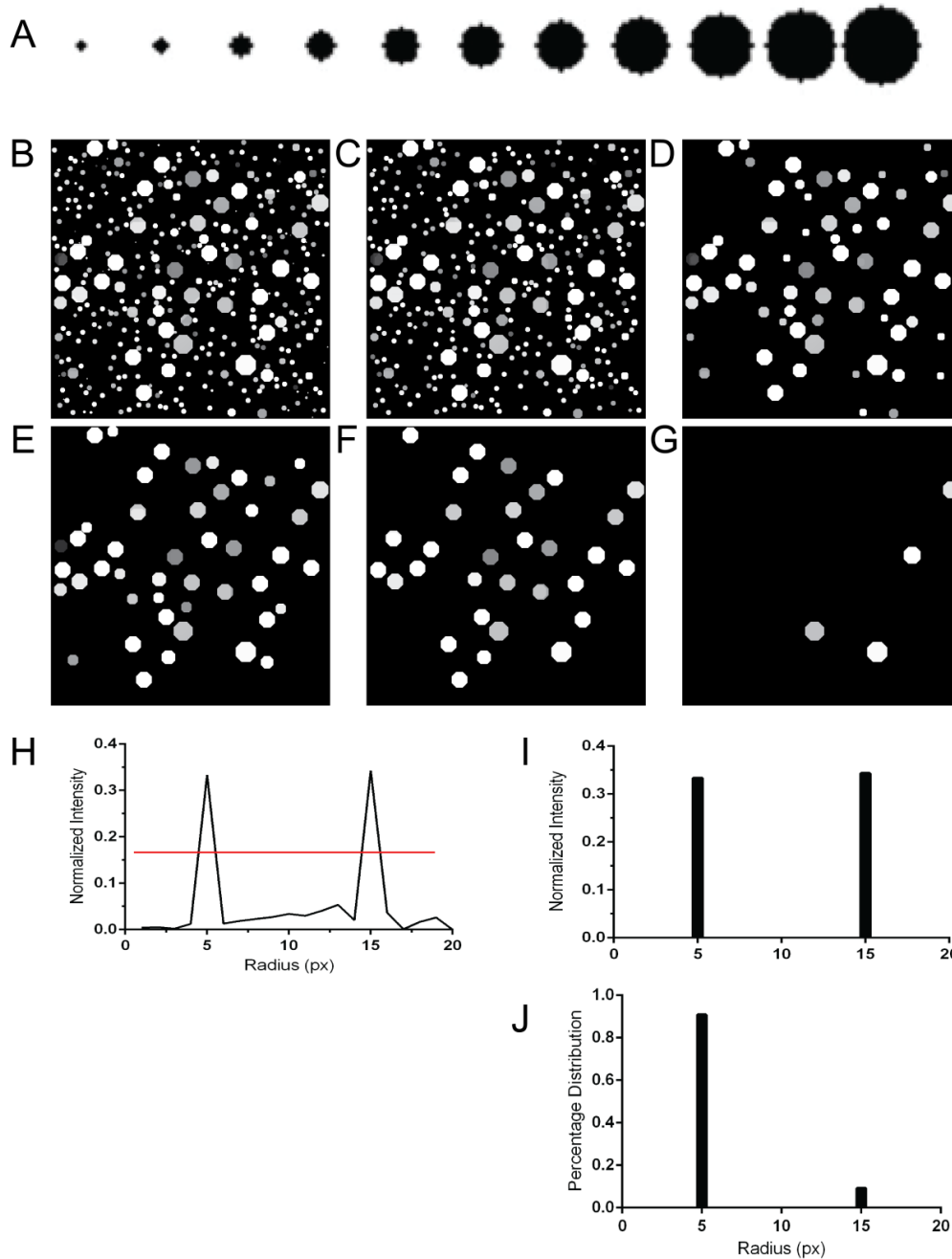


Figure 13. Granulometry process on example image. (A) Example of increasing structuring element shape and size for morphological opening operations. (B) Example image with objects of various sizes. Principal components of size 5 and 15. (C-G) Resulting image after performing morphological opening of size 3, 7, 9, 13, and 16 pixels respectively. (H) Normalized size density results series of morphological openings. Threshold to remove objects overlaid in red. (I) Resulting filtered size density. (J) Resulting object distribution profile.

5.2.3.3 Size analysis

Filtering and estimation of isolated lipids was performed in order to limit analysis to principle sizes. To isolate lipids of a specific size, morphological operations of the preprocessed image were subtracted from each other as in equation (7). Once isolated, a binary mask, $M(\kappa)$, was created from the resulting image to remove noise remaining after subtracting images processed by morphological operations of different sizes (Eq. (8)). This mask was then applied to isolated lipids to preserve pixel intensity information while removing imaging artifacts, denoted as the filtered lipid image $F(\kappa)$ (Eq. (9)).

$$L(k) = (I \circ \lambda_{\kappa}) - (I \circ \lambda_{\kappa+1}) \quad (7)$$

$$M(\kappa) = \text{BOOL} \{L(\kappa)\} \circ \lambda_{\kappa} \quad (8)$$

$$F(\kappa) = L(\kappa) \times M(\kappa) \quad (9)$$

Using the processed lipid images, a filtered size density, $G(\kappa)$ (Eq. (10)), was created by setting an empirical threshold (T) to one standard deviation over the mean of $d\Phi(\kappa)$ (Eq. (11) and Figure 13H). Values for $d\Phi(1)$ and $d\Phi(2)$ were ignored during threshold calculation and for $G(\kappa)$ as lipids in this range are non-existent according to smallest values observed in Klemm *et al.* (Figure 13I)¹²⁵.

$$G(k) = \begin{cases} 0, & d\Phi(\kappa) < T \\ v[F(\kappa)], & d\Phi(\kappa) \geq T \end{cases} \quad (10)$$

$$T = \overline{d\Phi} + \sigma_{d\Phi} \quad (11)$$

5.2.3.4 Data normalization

The last steps of lipid analysis normalize the filtered size density by structuring element area to estimate the quantity of lipids present, $\Lambda(\kappa)$, and by the sum of lipids detected during analysis to approximate the lipid distribution profile, $\Upsilon(\kappa)$ (Eq. (13) and Figure

13J). In equation (12 below, $\alpha(\kappa)$ represents the number of pixels present or area for each structuring element.

$$\Lambda(\kappa) = \frac{G(\kappa)}{\alpha(\kappa)} \quad (12)$$

$$Y(\kappa) = \frac{\Lambda(\kappa)}{\sum \Lambda(\kappa)} \quad (13)$$

5.3 Results and Discussion

5.3.1 Software Estimation of Object Population Percentage and Size Validated Using Synthetic and Bead Images

To establish the capability of our method, we created a synthetic image library populated with images densely packed with objects of various sizes and random intensity values. Using this library, we show that our modified granulometry process is capable of estimating object size and population percentage in synthetic images, created to be comparable to *C. elegans* lipid distributions in both spatial layout and pixel intensity. Figure 14A-F displays the granulometry process on an example image containing three populations of objects with equal total area for each assorted size (33.3% for all objects). Results of analysis show the similarity between algorithm results and known values demonstrating the ability of our algorithm to accurately estimate population percentage. Software results for objects of radius size two, five and ten pixels were $33.0 \pm 0.1\%$, $32.8 \pm 0.1\%$ and $33.2 \pm 0.2\%$ respectively compared to the true value of 33.3% (mean \pm standard deviation, Figure 14G). Summing the percent errors for each of the population results in a total cumulative error of less than 13%.

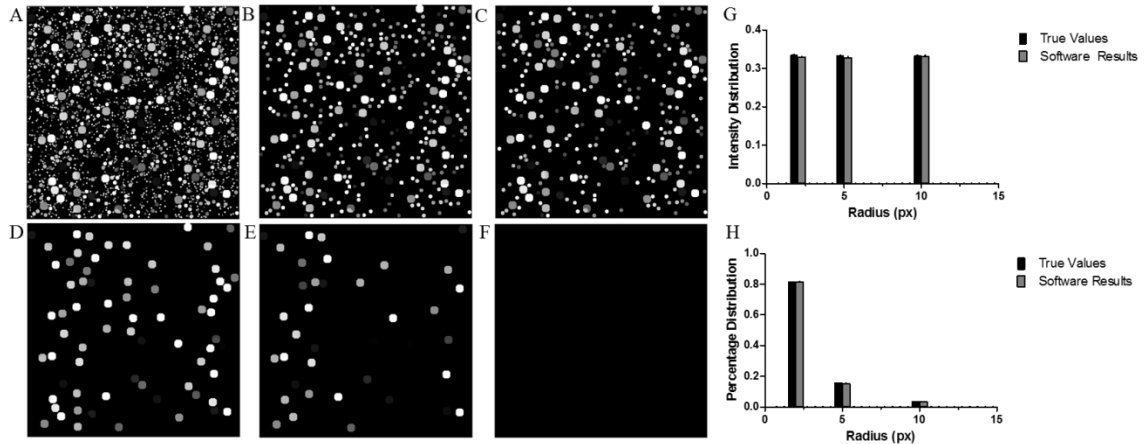


Figure 14. Size analysis of synthetic images. (A) Example image used for object size and quantity analysis. (B-F) Morphological opening of image in panel A using a disk shaped structuring element of radius 1, 2, 5, 9, and 10 pixels respectively. (G-H) True values and software results for filtered size density and object distribution profile, respectively, for a test library of synthetic images (n=30). Program results shown in gray. Known values shown in black. Total number and area for objects of a specific size was kept constant between each created image.

Discrepancies between results can be attributed to the close proximity and intensity mismatch between objects in synthetic images. While not overlapping, objects within close proximity of each other are sometimes considered a single object during analysis. To test this relationship, we created a set of synthetic images varying the distance between objects. As the distance between objects increased, the accuracy of our method also improved with the lowest cumulative error of 8.7% (for all three objects) occurring at a separation distance of 5 pixels (Figure 15). To test the effect of intensity variation on our method, we created a separate synthetic image library with all objects at equal pixel intensity, and with a separation distance of 5 pixels. By keeping pixel intensity uniform between objects, cumulative error for all three objects was reduced to 2.7%. Combined with our previous results, these findings suggest that pixel intensity and inter-object distance are two main sources of error for our proposed analysis method. Therefore, for the method to be useful, one needs assessment of the intensity distribution as well as ensuring a reasonable density of the objects to be analyzed.

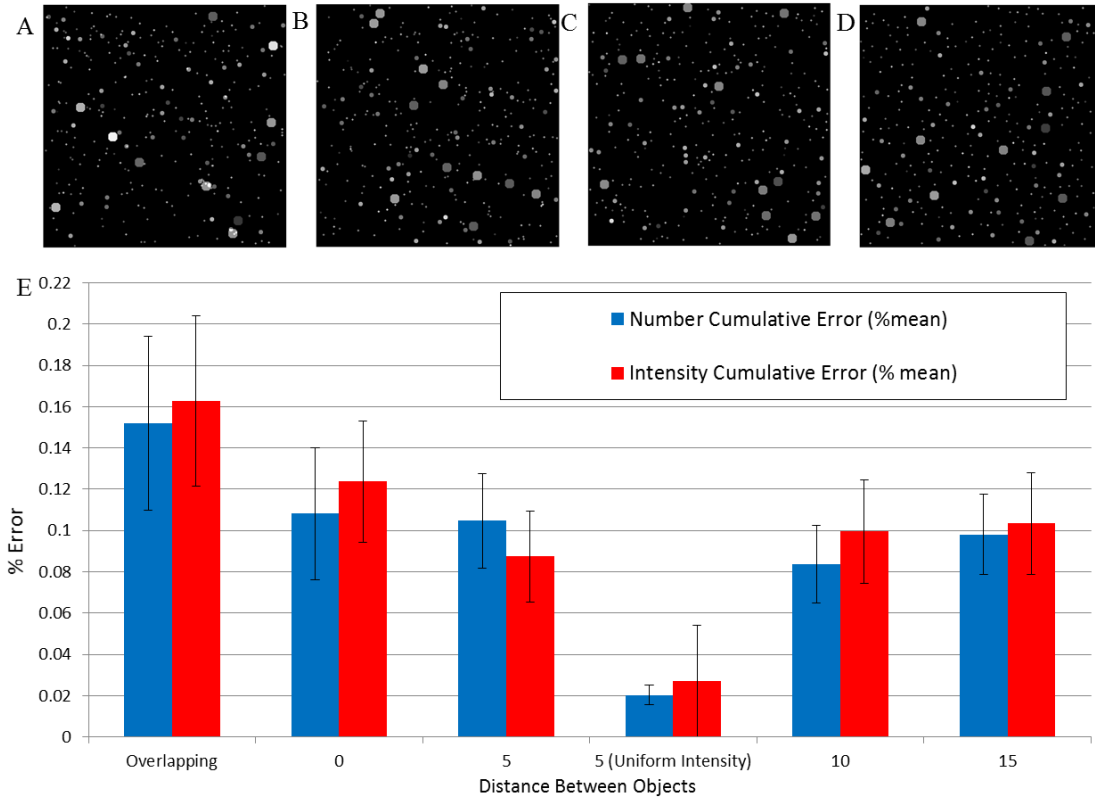


Figure 15. Effect of object proximity and intensity variation on software results. (A-D) Example images for overlapping objects and objects limited to a minimum distance apart of 0, 5, and 10 pixels respectively. Objects created with random intensities. (E) Average cumulative error for image library for proximity and intensity analysis. $n=30$ for each test. Error bars represent standard deviation.

Next, we used fluorescent beads of to test the ability of our method to characterize objects of known sizes using non-synthetic images. Figure 16A-F demonstrates the granulometry process on an example image of fluorescent beads of $1\mu\text{m}$, $2\mu\text{m}$, and $4.5\mu\text{m}$ diameters. Figure 16G displays the computed average object quantity for fluorescent bead images using our method next to hand measured values. Results from analysis show that our algorithm is capable of characterizing fluorescent objects of different sizes within a mixed population. Population percentage values returned for $1\mu\text{m}$, $2\mu\text{m}$, and $4.5\mu\text{m}$ diameter beads were 63%, 34%, and 3% respectively.

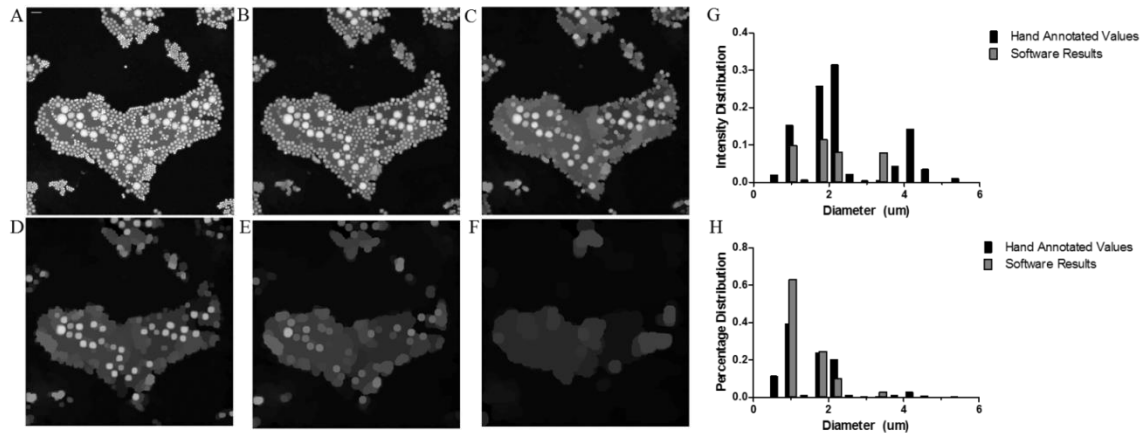


Figure 16. Size analysis of fluorescent beads. (A) Preprocessed image of fluorescent beads of various sizes. (B-F) Morphological opening operation on image shown in panel A using a disk shaped structuring element of radius, 2 μ m, 4 μ m, 5 μ m, and 8 μ m respectively. Scale bar is 5 μ m. (G-H) Respective filtered size density and lipid distribution profile for shown image. Software results shown in gray. Hand measured values shown in black.

As in synthetic image experiments, errors between computational analysis and manually measured values are attributed to the density and close proximity of objects (fluorescent beads). To characterize this effect, we created image libraries of specific diameters and assessed the accuracy of our analysis method. Figure 17 demonstrates the distributions returned for fluorescent beads of various diameters and is summarized in Table 1. Experimental results returned a disparity range from 0.1 μ m to 1.6 μ m for isolated bead experiments. Thus, even when analyzing images with objects limited to a specific size, results of granulometry based methods are still prone to report a false size distribution. Figure 16G displays this affect, with sizes reported for 1 μ m, 2 μ m, and 4.5 μ m.

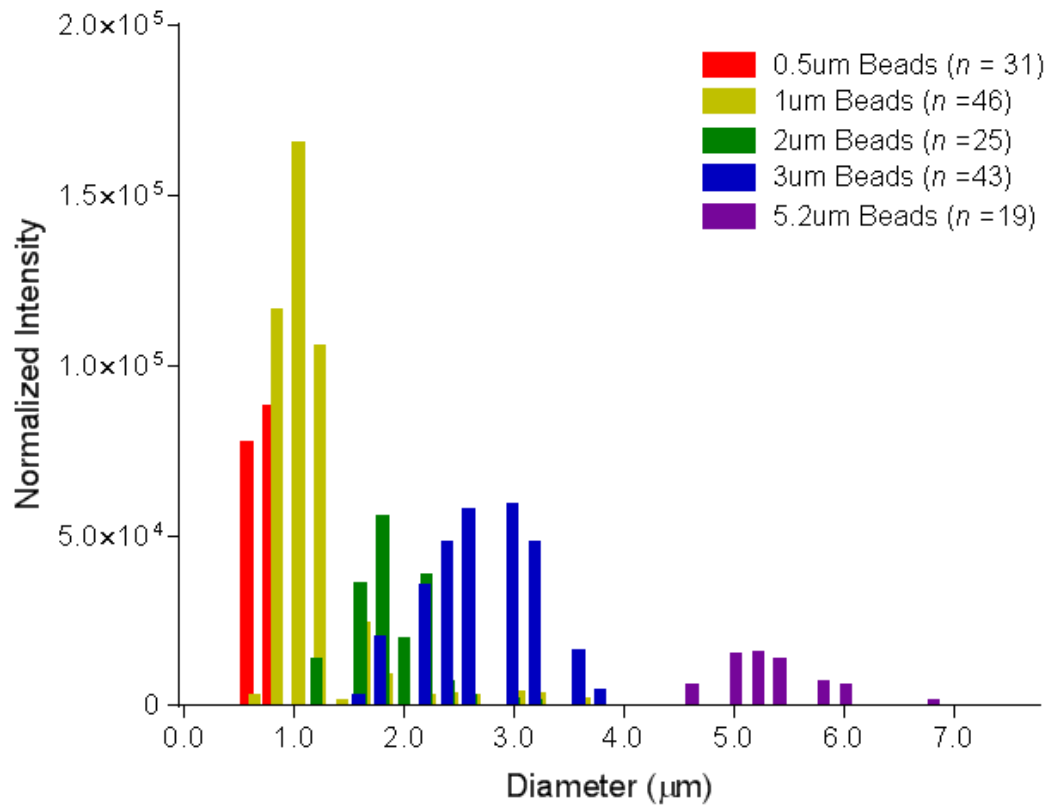


Figure 17. Software analysis of single-size population bead experiments. Sum of all image results instead of mean shown for this figure.

Table 1. Summary of software analysis of single-size population bead experiments.

Specified Bead Size (μm)	Mean (μm)	STD (μm)	N (# of images)	Range (μm)
0.5	0.71	0.1	31	0.6 – 0.8
1.0	1.1	0.4	46	0.6 – 3.6
2.0	1.9	0.3	25	1.2 – 3.2
3.0	2.7	0.5	43	1.6 – 3.8
5.2	5.3	0.4	19	4.6 – 6.8

5.3.2 Software Characterization of Wild-Type and Lipid Metabolism Mutant Populations Mimics Known Distributions

After validating our proposed method using objects of known sizes, we tested the ability of our algorithm to distinguish between *C. elegans* wild-type and *atln-1* mutant (allele *a015*) populations (Figure 18A-B). Alleles used in this study were previously described in Klemm, *et al.* and are known to exhibit different distributions of lipids ranging from $0.2\mu\text{m}$ to $4\mu\text{m}$ ¹²⁹.

Figure 18 displays the results of applying our method to characterize and discern differences between lipid distributions for both wild-type and atlastin mutant populations. Inspecting morphological operations between the two populations demonstrates the ability of granulometry to selectively remove objects of specific sizes from biologically relevant data (Figure 18C-F). Figure 18C-F demonstrate morphological openings of preprocessed images derived from panels A and B. Examination of the atlastin mutant image reveals that by approximately $0.5\mu\text{m}$, most lipids have been removed (Figure

18D), while lipids in the wild-type image are still present at $1\mu\text{m}$ (Figure 18E). These observations are reflected in the average filtered size density (Figure 18G) computed for both populations ($n=14$), demonstrating different lipid distributions for atlastin and wild-type populations. As seen in the morphological opening examples, most lipids are removed from the atlastin population images by $0.75\mu\text{m}$, while wild-type examples demonstrate characteristic lipids up until double that size at $1.5\mu\text{m}$.

Comparing computational results to manually measured data demonstrates the utility of our process to discern differences in lipid size between nematode populations. Our analysis method estimates a clear distinction in lipid size for atlastin and wild-type animals as seen in Klemm, *et al.*; however, size range returned from computational analysis is reduced when compared to manual measurements. This reduction is a consequence of filtering the returned size density of each animal to reduce noise while limiting results to principal lipid sizes. As such, the size range for the atlastin mutant population is reduced from $0.2\mu\text{m}$ - $1\mu\text{m}$ (manual) to $0.25\mu\text{m}$ - $0.7\mu\text{m}$ (computational), while the wild-type population shows a decrease from $0.4\mu\text{m}$ - $2\mu\text{m}$ (manual) to $0.77\mu\text{m}$ - $1.4\mu\text{m}$ (computational) ¹²⁹.

Another difference between our analysis and manual measurements is the concentration of lipid sizes observed per population. Klemm, *et al.* show through their analysis that lipids $0.4\mu\text{m}$ in diameter comprise approximately 30% of total lipids measured for atlastin mutant populations; our results indicate that the largest lipid concentration is at $0.25\mu\text{m}$ and 35% of total measured objects. Similarly Klemm *et al.* report that $1\mu\text{m}$ lipids comprise 25% of all measured lipid droplets for wild-type populations while our results estimate that the most frequent size is $0.77\mu\text{m}$ which makes up 13% of lipids.

Differences between lipid distribution profiles between computed and manually measured results are attributed to computational bias of our method for smaller diameter objects, non-uniform lipid intensity, and optical limitations due to imaging resolution.

During analysis, returned filtered size density is normalized by dividing results by the size of the structuring element used for its corresponding morphological opening. This is performed to compensate for larger opening operations whose results consist of more pixels. Reviewing the filtered size density results in Figure 18G demonstrates better adherence to previously reported results seen in Klemm, *et al.* than our estimated lipid distribution profile in Figure 18H. Results show peaks of normalized intensity at $0.38\mu\text{m}$ compared to $0.4\mu\text{m}$ (manual) for atlastin mutants, and $0.96\mu\text{m}$ compared to $1\mu\text{m}$ for wild-type. However, these results only report the normalized intensity of objects of specific sizes and do not include any information pertaining to quantity.

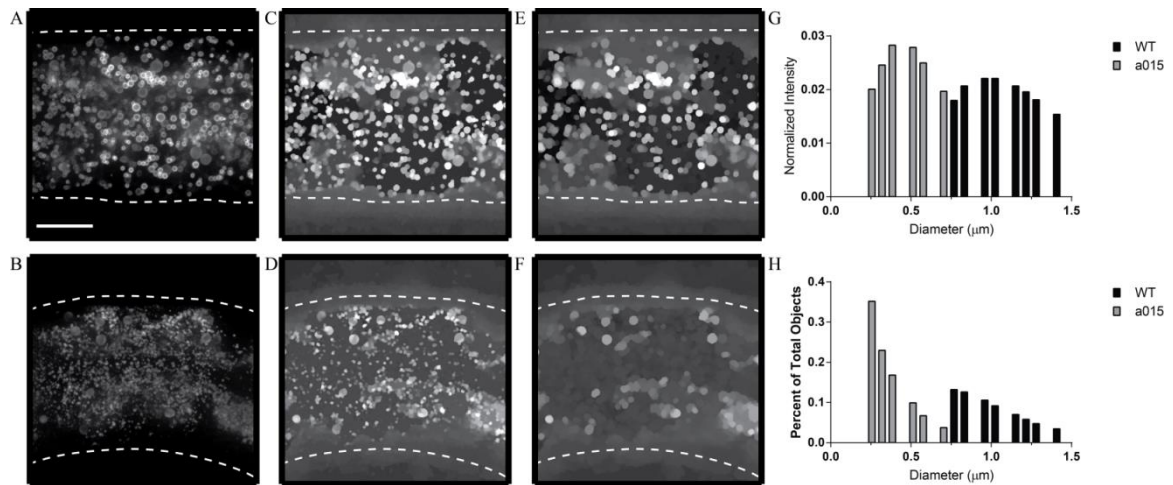


Figure 18. Lipid analysis of *C. elegans* images. (A-B) Maximum projection of example wild-type (WT) and atlastin mutant (*a015*) animals respectively. Body outline shown in white. Scale bar is $6\mu\text{m}$. Images brightness and contrast manually adjusted for better viewing of lipids. (C-D) Morphological opening corresponding to $0.5\mu\text{m}$ for respective preprocessed WT and *a015* images. (E-F) Morphological opening corresponding to $1\mu\text{m}$ for respective preprocessed WT and *a015* images. (G) Filtered size density results for WT and *a015* populations. (H) Lipid distribution profile for WT and *a015* populations. $n=14$ for both populations.

As seen during our previous experiments using synthetic images, non-uniformity of objects can lead to discrepancies between measured and computed quantities. To measure the extent of non-uniformity between images as well as nematode populations,

we measured the average intensity per lipid for four different wild-type and atlastin mutant images (Figure 19). Analysis demonstrates that intensity of lipid droplets does not vary according to size within each population (Figure 19B-D); however, comparison of the wild type and *atln-1* population reveals a much broader lipid intensity range for *atln-1* (Figure 19). While there is an intensity mismatch between both populations, every independent image for each population is normalized during analysis to mitigate the effect of intensity on granulometry results. While the mismatch does not appear to significantly bias results distinguishing the two populations, it may help to explain discrepancies between calculated and measured values.

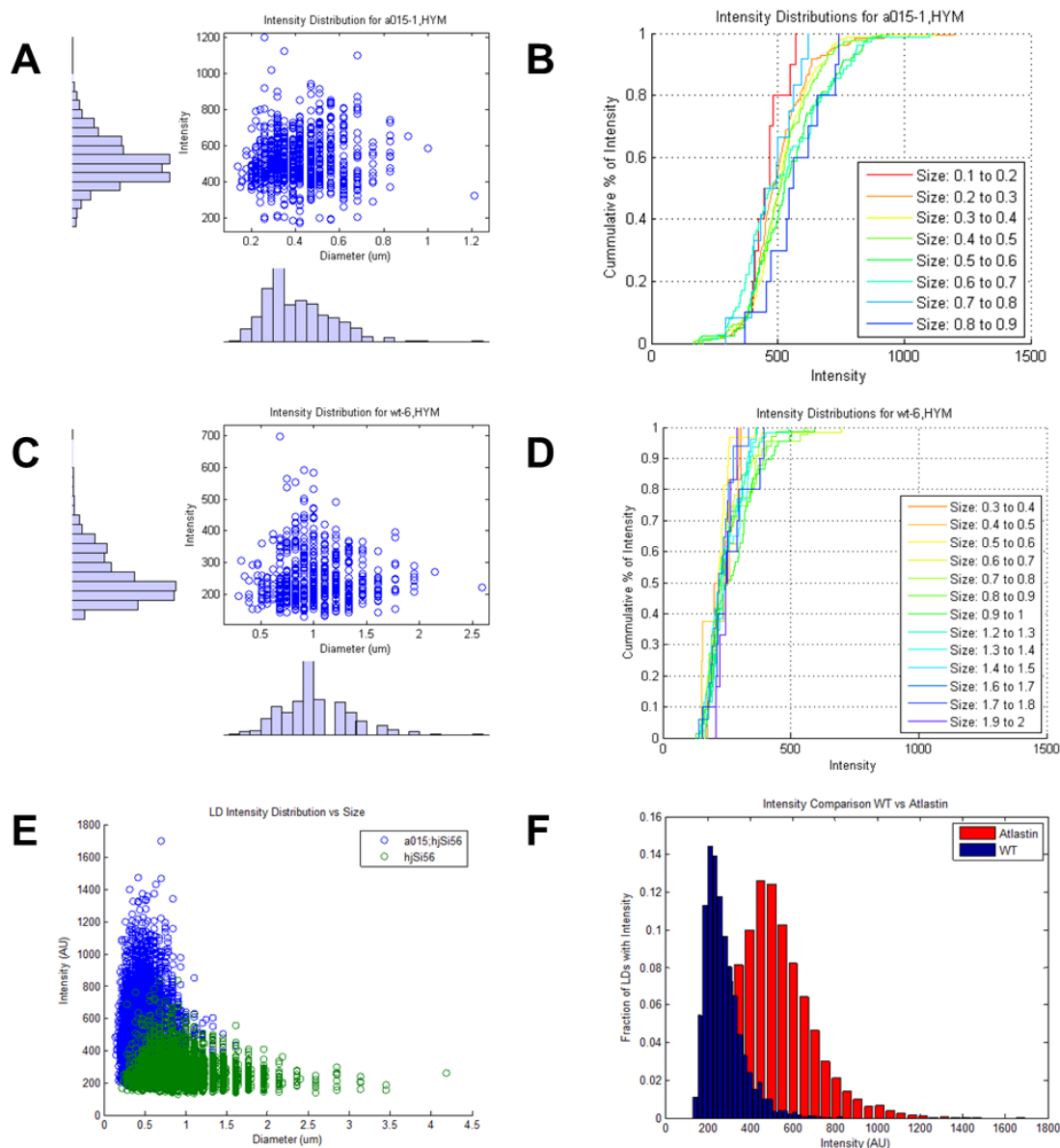


Figure 19. Intensity analysis of single lipids for wild-type and *atln-1* mutant populations.

Lipid droplet intensity distribution and cumulative distribution function for *atln-1* (A-B) and wild-type (C-D) example images. (E) Scatterplot of lipid droplet size for wild-type and *atln-1* population (n=4 for both populations). (F) Histogram comparison of images from panel E plotting intensity versus the fraction of lipid droplets.

Another potential source of error in analysis is limited by the resolution of the microscopy system for measuring alleles such as *a015* with lipids in the submicron range.

The resolving power of the confocal microscope utilized for imaging is approximately $0.2\mu\text{m}$, placing the smallest determined lipid droplets from the *atln-1* population under the optical resolution of the system ($0.1\mu\text{m}$ in diameter). Consequently, any objects smaller than this resolution captured in images using this system cannot be verified as true lipids. Therefore, while the size distribution of lipid droplets for the *atln-1* population is known to be smaller than that of the wild-type population, the exact distribution is unknown.

Results from our computational method illustrate the ability to discern between populations of *C. elegans* with different lipid distributions. Manual methods of analysis involve constructing 3D volumes of acquired images from various focal planes and require skilled users to manually measure and annotate often over a thousand individual lipids. As such, standard methods for lipid analysis are tedious and labor intensive, requiring many hours per animal to characterize lipid distribution. Here, for the first time to our knowledge, we present a method capable of performing similar analysis of lipid distribution in approximately 25 seconds on average per animal ($n=14$, computer specifications listed in methods). We provide a method that estimates lipid size through analysis of a complicated phenotype with overlapping objects. Using our modified granulometry approach, we perform this analysis without the use of image segmentation methods, and with the ability to determine a difference between populations of *C. elegans* whose lipids vary on the order of $0.5\mu\text{m}$ on average.

5.3.3 Software Method Capable of Characterizing Low Resolution Images for Characterization of Wilde-Type and Lipid Mutant Populations

The current standard for manually measuring the size of lipids involves annotating 3D reconstructions of acquired images, requiring high fidelity imaging, such as confocal microscopy, in order to accurately recreate a 3D image from various focal planes. Our proposed method, however, analyzes the maximum projection of an image stack,

eliminating the need for 3D reconstructions and high fidelity imaging along with it. To test the characterization ability of our granulometry approach using lower fidelity techniques, we analyzed the effect of diet on lipid size and evaluated images captured using an epi-fluorescent microscope. Images in this section were captured on a microfluidic device fabricated in the Lu laboratory, with a design out of the scope of this dissertation, and will not be discussed. Ultimately, the design of the device has little bearing on the presented work; however, it is worth noting for future applications that the images of animals obtained were captured on-chip, in a device capable of sorting animals into wild-type and mutant output channels as previous designs.

Zhang *et al.* have shown in previous work that feeding *C. elegans* different strains of bacteria ultimately affects lipid size of *dhs-28* animals¹²⁴. Animals deficient for *dhs-28*, a gene involved in peroxisomal β -oxidation used to break down fatty acids, show selective expansion of lipid droplets¹²⁴. We similarly tested this affect using the transgenic *dhs-28;hjSi3(R01B10.6::GFP)* strain fluorescently labeling seipen, a protein commonly found in the endoplasmic reticulum and associated with lipid droplets^{48,130}.

Using an altered version of our software method (specific to epi-fluorescent images and described in appendix section A.3.1), we were able to recreate trends seen in published data for *dhs-28* animals¹²⁴. Figure 20 displays results of our software analysis demonstrating the ability of our method to discern differences between populations that are quantitatively unique despite being similar in phenotypic appearance, and to analyze low resolution images and produce results similar to manual analysis on higher quality imaging systems. Comparing the fluorescent expression of *hjSi3* for HB101 and OP50 fed animals (Figure 20A-B respectively) demonstrates subtle differences in lipid size, with OP50 fed animals exhibiting larger size lipids on average; however, this phenotype is not strikingly apparent when performing visual analysis, and serves to demonstrate the difficulty in characterizing phenotypes involving the characterization of a multitude of objects. This can be also be seen when comparing morphological opening operations at

1.52 μm and 5 μm for example images of both HB101 and OP50 fed animals as they do not display any obvious differences at either point of analysis (**Figure 20C-F**).

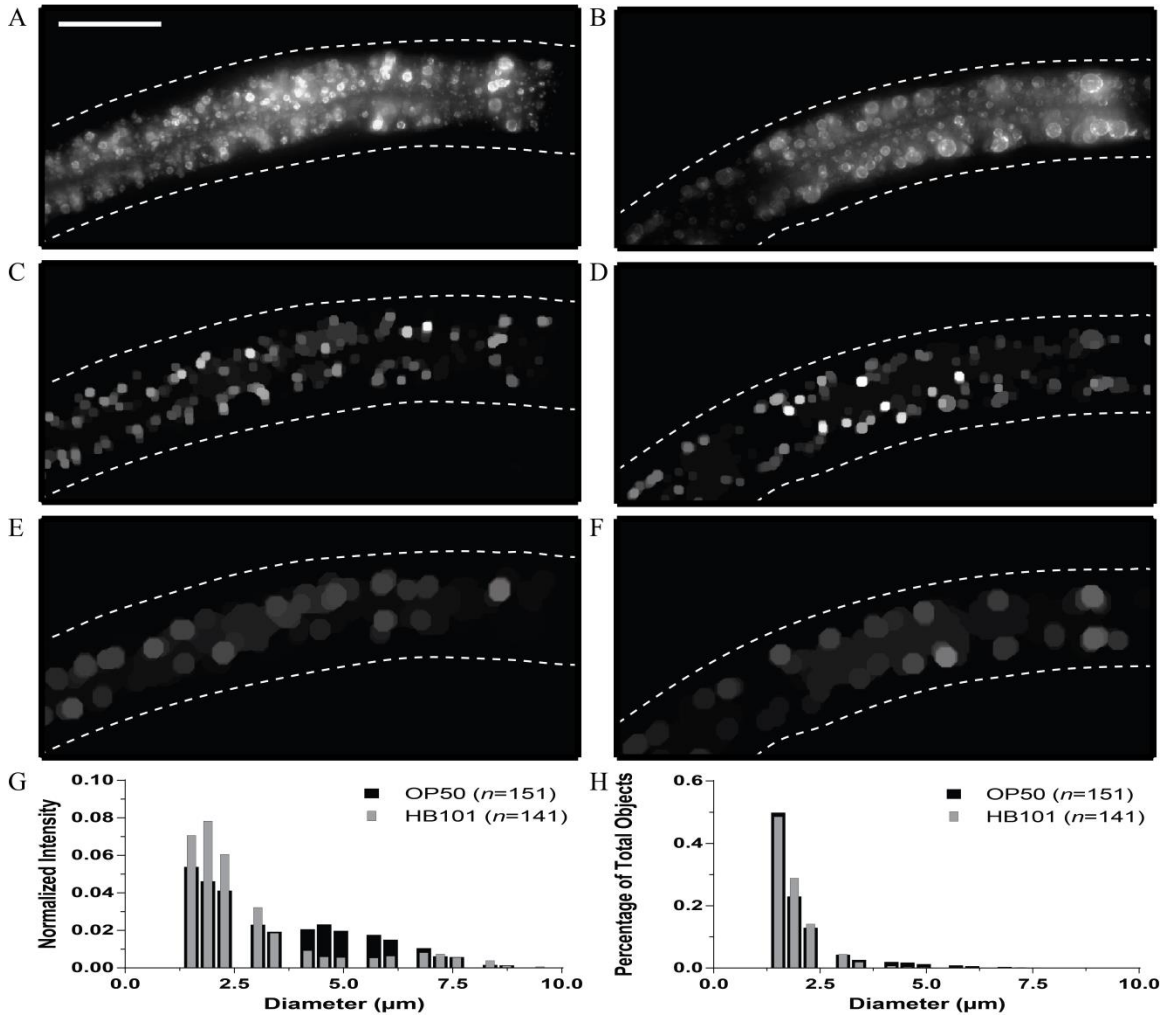


Figure 20. Software analysis of lipid size for epi-flourescent data. (A-B) Example maximum projection of *dhs-28;hjl3* animals fed HB101 and OP50 bacteria respectively. Body outline shown in white. Morphological openings corresponding to 1.5 μm (C-D) and 5 μm (E-F) for respective HB101 and OP50 fed images. (G) Filtered size density and lipid distribution results for respective HB101 and OP50 fed populations. Scale bar in panel A is 50 μm . Brightness and contrast manually adjusted for better viewing of lipids for all images.

Estimating the average lipid distribution for both populations, however, reveals different patterns between HB101 and OP50 fed populations (Figure 20G). Filtered size density results for both populations shows an increased average intensity (correlated to object number) for HB101 between 1.25 μm and 2.5 μm while OP50 displays the opposite

trend for increased intensity between 3.75 μm and 6.25 μm (Figure 20G). These results compare well to manual analysis seen in Zhang *et al.* which reflect a higher volume of lipids between 3 μm to 8 μm for OP50 populations¹²⁴. Increased levels of lipids in the lower range for HB101 are unique to our method and are not mirrored in manual analysis results¹²⁴. We attribute discrepancies between software and manual methods to low signal-to-noise ratios for epi-fluorescent images, due to diffuse light from various focal planes and low imaging resolution when compared to high quality systems. Figure 20H displays the lipid distribution profile for both populations. While overall phenotypic separation between HB101 and OP50 appears reduced, this analysis method produces results more similar to results seen in manual analysis. Evaluating the two populations by size-specific lipid percentage removes the large difference between the HB101 and OP50 populations in the 1.25 μm to 2.5 μm range while maintaining a small but discernible difference favoring OP50 in the 3.75 μm to 6.25 μm range (Figure 20H).

While software results may not exactly mirror manual analysis, we present a method for rapidly characterizing lipid distributions in low fidelity imaging systems. This characterization is rapid, performed in 5.4 \pm .03 seconds on average for all images evaluated ($n=292$, mean \pm standard deviation), and enables the characterization and classification of phenotypes on-chip, at a rate over 1000 times faster than manual methods. This technology therefore enables the ability to perform on-chip genetic screening of *C. elegans* lipid mutations, and using microscopy systems that are readily available in most laboratories, eliminating the need for costly confocal or advanced imaging systems. This work can be easily expanded to characterize other problems requiring the need for high-speed analysis of large quantities of objects of any shape or size.

5.4 Conclusions

Results of using our computational method reveal the ability to quickly characterize mixed populations of objects and accurately estimate the population percentage for each object group by size. We validated this technology characterizing *C. elegans* lipids and demonstrate results comparable to hand measured values. Here, for the first time to our knowledge, we present a method capable of performing lipid characterization in as fast as 5 seconds on average per animal. Using this approach, we increase throughput over standard methods by a factor over three orders of magnitude, enabling real-time and automated genetic screens of *C. elegans* in search of lipid mutations. Additionally, we demonstrate the capability to perform genetic screens on low fidelity images, circumventing the need for expensive confocal microscopy systems which are unavailable in every laboratory.

We provide a software method capable of estimating object size and proportional quantity on the order of seconds. Using this technology, we demonstrate the capability to saturate genetic screens in search of lipid mutations in *C. elegans*. Our software is flexible and easily modified to characterize objects of various sizes and shapes, making our algorithm applicable to other biological systems or processes. Using this method, we deliver a technological means to quickly characterize images densely packed with objects for real-time analysis.

CHAPTER 6 AUTOMATED CHARACTERIZATION OF NEURODEGENATIVE AND NEURODEVELOPMENT DEFECT MUTATIONS IN *C. ELEGANS*

The following work in this chapter was performed in collaboration with Dr. Massimo Hilliard's laboratory at the University of Queensland, Australia.

6.1 Introduction

Neurodegeneration is a naturally occurring process during neurodevelopment (pruning), but is more widely known for its role with various neural pathologies such as Alzheimer's, Parkinson's, and Huntington's disease. With the advancement of medical technologies and increased life spans, neurodegeneration has become a forefront of concern as it is closely related to many age-dependent diseases; however, elucidating the mechanisms of neurodegeneration is a difficult and a fundamental question in neuroscience. While many genes and proteins have been discovered that affect neurodegeneration (SOD, huntingtin, presenilin, β -amyloid, tau, α -synuclein, and LRRK2), the complex interactions between these networks are still not fully understood^{16,18,114,131,132}. Unraveling these mechanisms is paramount to identifying new genes and pathways that are critical for understanding neuronal repair, regeneration, and necessary to develop therapeutic techniques.

The nematode *C. elegans*, is an excellent model for studying the complex genetic mechanisms of neurodegeneration and neural development because of its sequenced genome and well-documented nervous system^{20,96,103}. The organism lends itself well to neuroscience studies because of its transparency and stereotypical neuronal connectivity; additionally, many biomolecular mechanisms are well conserved between the nematode and vertebrates, ranging from common guidance and polarity cues to major neurotransmitter systems^{11-15,114,133}. Previous research studying neurodegeneration has also been performed using *C. elegans*, with pathology models and studies performed to

elucidate the mechanisms behind disorders such as Alzheimer's, Parkinson's, amyotrophic lateral sclerosis, and Huntington's disease^{1,16-19}.

In *C. elegans*, the tail sensory neuron PQR provides an ideal opportunity to study neural development and degeneration because of its relatively long axon and bipolar structure. PQR along with the neurons AQR and URX, fluorescently labeled using transgene *kyIs417*[*Pgcy-36::GFP*, *Podr-1::dsRed*], are known to be involved in aerotaxis, social feeding, and bordering behavior^{50,133,134}. PQR can be used to study neurodegeneration on a comparatively long axon, providing multiple areas for degeneration to occur over a quarter length of the animal body, facilitating detection by software. The axonal process extends anterior and projects into the preanal ganglion, joins the ventral nerve cord, and terminates normally just posterior to the vulva⁶. Neuronal polarity is also easily distinguishable because of PQR's bipolar form. Opposite of its axon, PQR extends a dendritic process posterior into the tail where its ciliated sensory endings are exposed to the coelomic body fluid of the animal¹³⁴. Additionally, the PQR neuron can be used as a behavioral readout for neurodegenerative phenotypes due to its association with aggregation and bordering behaviors⁵⁰.

Currently, standard manual methods of investigating *C. elegans* are low-throughput and are bottlenecks to the discovery of new genes involved with neurodegeneration and neural development. Recently, systems have emerged that are capable of performing automated and high-throughput screens of adult nematodes^{34,39,91,135}; however, most of these technologies have not been applied to or optimized for quantitative screening of detailed neuronal characteristics. Instead, most of these methods search for the lack or presence of fluorescent expression in neurons or specific body locations. These methods are therefore impractical for studying neuronal morphology which requires complex analysis of neuronal structure. Typically, before any metric can be calculated for an object in an image, the pixels defining its structure and location have to be isolated from background. Image segmentation methods, widely used

in the field of computer vision, are normally employed for problems dealing with object identification and can be used to detect neurons and neuronal processes^{39,46,60,100}. However, even adaptive segmentation methods alone are ill equipped and poorly suited for morphology analysis due to highly variable pixel intensities for features of interest and low signal-to-noise ratio commonly seen during genetic screens.

To overcome these issues, we present a method combining adaptive segmentation algorithms with a mathematical connectivity model to accurately segment, join isolated neuronal fragments, and characterize neuronal processes for detection of neurodegenerative and developmental mutations. The premise of this work is similar to previous studies using tracing algorithms for neural process or curved structure detection¹³⁶⁻¹⁴¹. General advantages of using our system are threefold: First, phenotype analysis uses standard and comparatively simple algorithms that are widely available in image processing libraries and implementable in multiple programming languages; Second, our software analyzes multiple phenotypes, comparing various metrics of neuron morphology; Lastly, screening of neuron morphological phenotypes can be performed on-chip, requiring only seconds per animal, providing a high-throughput alternative to standard and laborious manual screening methods.

6.2 Materials and Methods

6.2.1 Microfluidic device fabrication, design, and operation

Microfluidic devices used in this study were fabricated using standard techniques discussed in chapters 3 and 4. Feature height for microfluidic chips in this work was 50 μm while channel widths were 70 μm (except for sorting outputs), designed to be slightly smaller than an adult worm to reduce movement during image. Devices were fabricated using a 10:1 ratio of elastomer to cross-linker with an overall device height of approximately 3mm. Serpentine channel within the device imaging area utilized a radius of curvature of 125 μm , measured from arc center to outer edge of channel.

Device operation utilized similar principles to previous genetic screening devices designed in the Lu laboratory, pressure driven flow and partially closed valves to control worm loading, imaging, and sorting^{32,34,40,42,111}. Partially closed valves were similarly loaded with a 58% glycerol solution to improve imaging of *C. elegans* within microfluidic chips by approximating and matching the refractive index of PDMS^{33,111}.

6.2.2 *C. elegans* strains, culture, mutagenesis, and imaging

C. elegans strain *kyIs417*[*Pgcy-36::GFP, Podr-1::dsRed*] was used in this study and was cultured between at 15°C, 20°C, or 25°C using established protocols⁹⁶. Animal phenotype scoring was performed off-chip on agar pads prepared using conventional methods using 5 mM sodium azide (Sigma Aldrich) as an anesthetic⁹.

Chemical mutagenesis of nematodes was performed using standard concentrations of the mutagen ethyl methanesulfonate (Sigma Aldrich) to perform pooled F2 screens of gravid adults¹⁰. Animals were visually inspected on-chip during genetic screening and were isolated if they expressed defects in dendrite or axon length, signs of neurodegeneration (beading or breaks in GFP expression), or gross morphological differences when compared to normal wild-type expression. Images captured on-chip for phenotype analysis recorded from multiple focal planes, 5µm apart for a total distance of 35µm, using 15 mM tetramisole (Sigma Aldrich) as an anesthetic.

C. elegans imaging performed in this study, whether off-chip or on-chip, utilized 20x/0.5NA or 40x/0.75NA objectives on either an upright (Leica DM4500) or inverted (Leica DMI6000 B) compound epi-flourescent microscope.

6.2.3 Probability model used for PQR characterization and analysis

PQR images were analyzed by custom software and were imaged using a 20x/0.5NA objective on either of the previously mentioned microscopes. All software written for analysis was programmed in MATLAB®.

Equations (14)-(17) below display the probability model used to join fragmented process segments:

$$P(x, \hat{\theta}, L) = \alpha P(x) + \beta P(\hat{\theta}) + \zeta P(L) \quad (14)$$

$$x = \sqrt{(x_{pt1} - x_{pt2})^2 + (y_{pt1} - y_{pt2})^2} \quad (15)$$

$$\hat{\theta} = |\theta - \overline{\theta_B}| \quad (16)$$

$$L = L_1 L_2 \quad (17)$$

where x is the euclidian distance between endpoints of fragments being considered for connection, $\hat{\theta}$ is the absolute difference for the angle of connection between the current points being evaluated for connection (θ) and the mean of all other angles of connection within the preferred direction bin ($\overline{\theta_B}$), and L is the combined length of the fragments (L_1 and L_2) being considered for connection. The variables α , β , and ζ are used to weight the importance of each of the individual probability functions for distance, angle, and length respectively with each function having a probability range of -1 to +1 (Eq. (18)-(20)). Points being connected together were limited to endpoints between the two objects that were within the closest proximity to each other.

To summarize, the probability of $P(x)$ will increase the closer that two fragments are to each other as long as the distance between fragments is below a maximum value set by $x_{\text{Threshold}}$. If the distance between fragments is above $x_{\text{Threshold}}$, than $P(x)$ will decrease as the distance between fragments approaches its maximum value. The maximum value for x will correspond to the distance between fragment endpoints in the image which are the furthest apart.

$$P(x) = \begin{cases} 1 - \frac{x}{x_{\text{Threshold}}}, & x \leq x_{\text{Threshold}} \\ \frac{-x}{\max(x)}, & x > x_{\text{Threshold}} \end{cases} \quad (18)$$

For $P(\hat{\theta})$, probability of connection will increase as the value of $\hat{\theta}$ decreases, suggesting that the current angle of connection is in the same direction as many other process fragments. This probability is also regulated by an angle difference threshold, ϕ . When $\hat{\theta}$ is less than the threshold, then the resulting probability value is positive. If $\hat{\theta}$ is greater than ϕ , then probability will decrease as $\hat{\theta}$ approaches its maximum value of 180 degrees.

$$P(\hat{\theta}) = \begin{cases} 1 - \frac{\hat{\theta}}{180}, & \hat{\theta} \leq |\phi| \\ \frac{-\hat{\theta}}{180}, & \hat{\theta} > |\phi| \end{cases} \quad (19)$$

Lastly, the probability of $P(L)$ will increase as L approaches its maximum value, the combination of the two longest segments in the image. This can only occur when L is greater than the square of $L_{\text{Threshold}}$, a value used to differentiate between actual process fragments and noise. If L is less than the square of $L_{\text{Threshold}}$, then $P(L)$ will correspondingly decrease the smaller that L is when compared to its maximum value.

Further software details about the probability model function and its equations can be found in the appendix A.4.2.

$$P(L) = \begin{cases} \frac{L}{\max(L)}, & L \geq L_{\text{Threshold}}^2 \\ \frac{L}{\max(L)} - 1, & L < L_{\text{Threshold}}^2 \end{cases} \quad (20)$$

6.2.4 Intensity profile peak detection for classification of neurodegenerative phenotypes

Classification of neurodegenerative phenotypes was performed by estimating characteristic peak profiles from pixels surrounding returned neuronal process trajectories from our probability model. To search for intensity peaks, a sample of 25 pixels using a line perpendicular to the image major axis was gathered. Coordinates of the returned neuronal process was used as a midpoint for each sample. Returned pixels values were then smoothed and an adaptive threshold was set to half of a standard deviation above the mean for the sampled intensity values. A local maximum function provided by MATLAB® was then used to search for intensity peaks for the pixels surrounding each coordinate of the returned neuronal process. If no peak was detected, the corresponding coordinate was considered to have a break in GFP expression. An animal was considered to exhibit a neurodegenerative phenotype if three or more coordinates returned no peaks for the mentioned intensity analysis method.

6.3 Results and Discussion

6.3.1 Microfluidic devices used for manual genetic screening

Genetic screening was performed on-chip using the devices shown in Figure 21. The “serpentine design” shown in Figure 21A-B was a precursor to the final “curved design” shown in Figure 1, used in previous work¹¹¹. Limiting animal movement is especially important in this work because PQR neuronal processes often span several focal planes, requiring manual adjustment of focus to properly analyze animal phenotype.

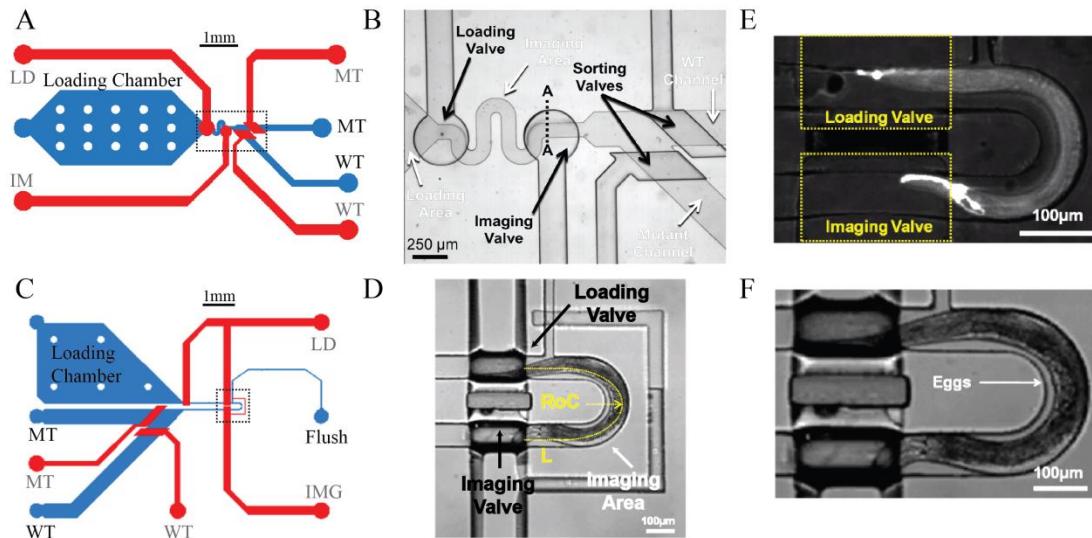


Figure 21. Devices used for manual genetic screening and nematode age compatibility. (A) Serpentine device design schematic. (B) Device image of dashed box shown in panel A. (C) Curved channel device design schematic. Black text in panels A and C represent fluid channels while gray text represents control layer valves. LD is loading valve; IMG is imaging valve; MT is mutant channel / valve; WT is wild-type channel / valve; Flush designates flush channel (Panel C only). (D) Device image of dashed box shown in panel C. Black text and arrows in panels B and D represent control layer valves while white text and arrows designate fluid channels. Radius of curvature (RoC) and length between valves (L) shown by yellow arrow and dashed arc respectively. (E) L3 to L4 animal loaded in device shown in panel C. Loading and imaging valve outlined in yellow dashed box. (F) Gravid adult loaded in device shown in panel C. Same animal shown as in panel D. White arrow designates eggs in animal.

While early device designs utilized a serpentine channel to restrict animal movement, curved areas impeded animal loading and exit from the imaging area. By reducing the number of curved sections, animal throughput increased from a previous maximum rate of 400 animals per hour to an average rate of 600 animals per hour (Figure 21A-D). In addition, a flush channel incorporated into the curved design improved overall device robustness, providing an additional pressure source to aid in animal exit without promoting additional loading of animals Figure 21C-D. This is accomplished by pressuring the loading valve of the device (labeled “LD” in Figure 21A), effectively cutting off flow into the imaging area, while leaving the imaging valve (labeled “IMG”)

and the desired sorting valve (labeled “MT” or “WT”) unpressurized to allow fluid flow from the flush channel input to a device exit.

These designs were utilized for this study because their ability to aid in animal immobilization and compatibility with animals of various sizes (Figure 21E-F). Preliminary experiments to characterize immobilization demonstrated the ability to acquire z-stacks of animals with little to no motion artifacts, maintaining partial immobilization for up to 10 seconds (Figure 22). Qualitative results suggest that devices with smaller RoC are able to maintain partial immobilization for longer durations and with more consistency between natural variations in animal size. Figure 22A demonstrates an animal within a device with the largest RoC exhibiting movement in the head and tail region over the course of 10 seconds. Animals within smaller RoC devices generally do not demonstrate as much head and tail movement. When compared to straight channel devices (Figure 22D), curved channel designs appear to limit sinusoidal body wave propagation while maintaining similar spacing between valves (L). We hypothesize that this locomotive impairment is due to a lack of adequate force to overcome channel geometry by animal body muscles.

By altering arc length (L) of the new design, we were also capable of examining animals at different stages of development while maintaining similar immobilization characteristics (Figure 21E-Figure 21F). Figure 21E depicts an animal in its 3rd or 4th stage of larval development (L3 or L4 respectively) within the device while Figure 21F depicts a gravid adult animal, easily identified because of the eggs present in the worms body. Screening animals at different stages of development allows animals to be examined for stage specific changes in phenotype in addition to searching for the early or late onset of neurodegenerative phenotypes.

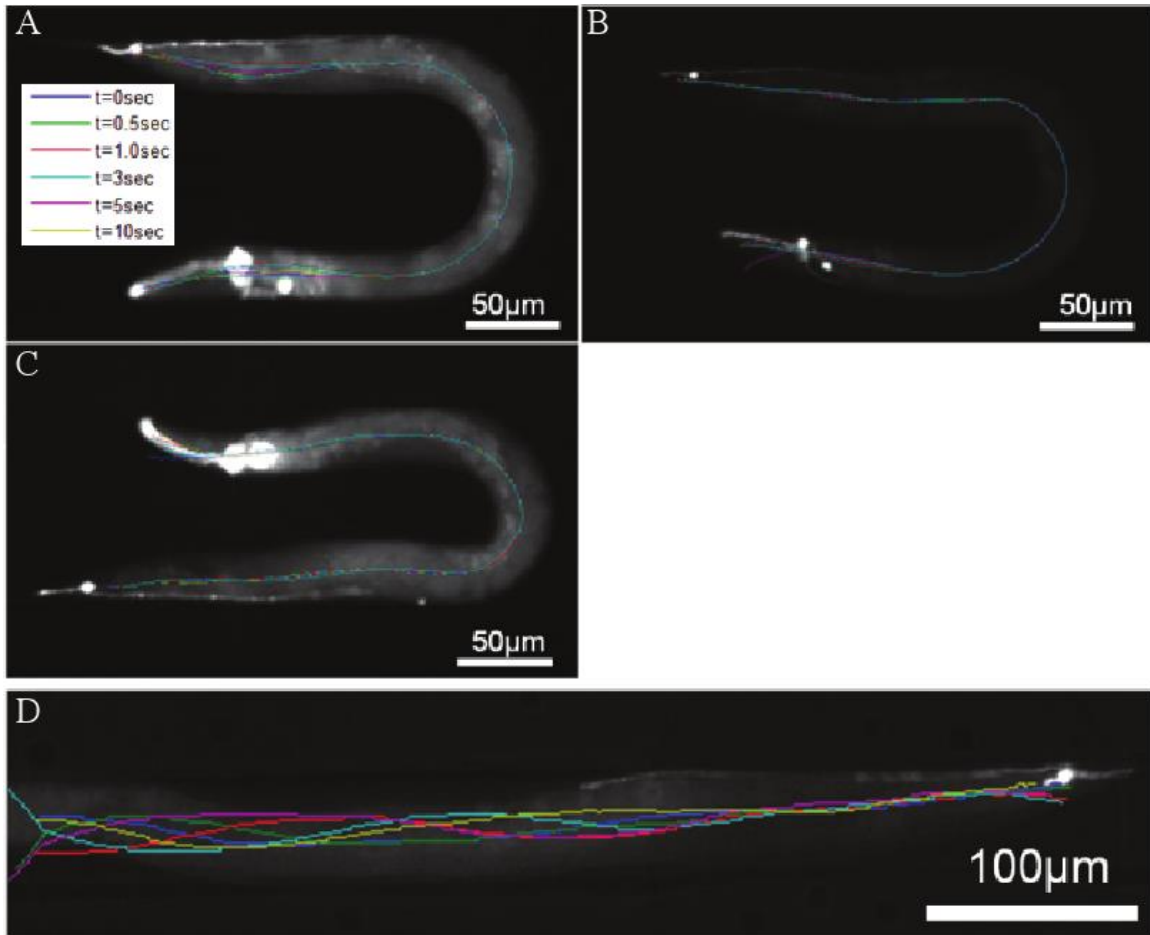


Figure 22. Movement of animals in curved and straight channel devices. (A)-(C) Animals loaded into curved channel devices with radius of curvature equal to $145\mu\text{m}$, $125\mu\text{m}$, and $105\mu\text{m}$ for panels A, B, and C respectively. (D) Animal loaded into straight channel design. Animal body midline estimated and overlaid for six different time points displayed in each image.

6.3.2 Manual screen to find mutants expressing neurodegeneration and neural developmental defects

A manual screen of over 20,000 animals was performed on-chip to discover neurodegeneration and neural development mutants; this serves also to use for software testing and validation. Using our microfluidic system, we successfully isolated 8 mutants (Figure 23) at a throughput of 400 and 600 worms per hour for serpentine and curved geometry designs respectively. Device throughput was measured over multiple experiments and devices.

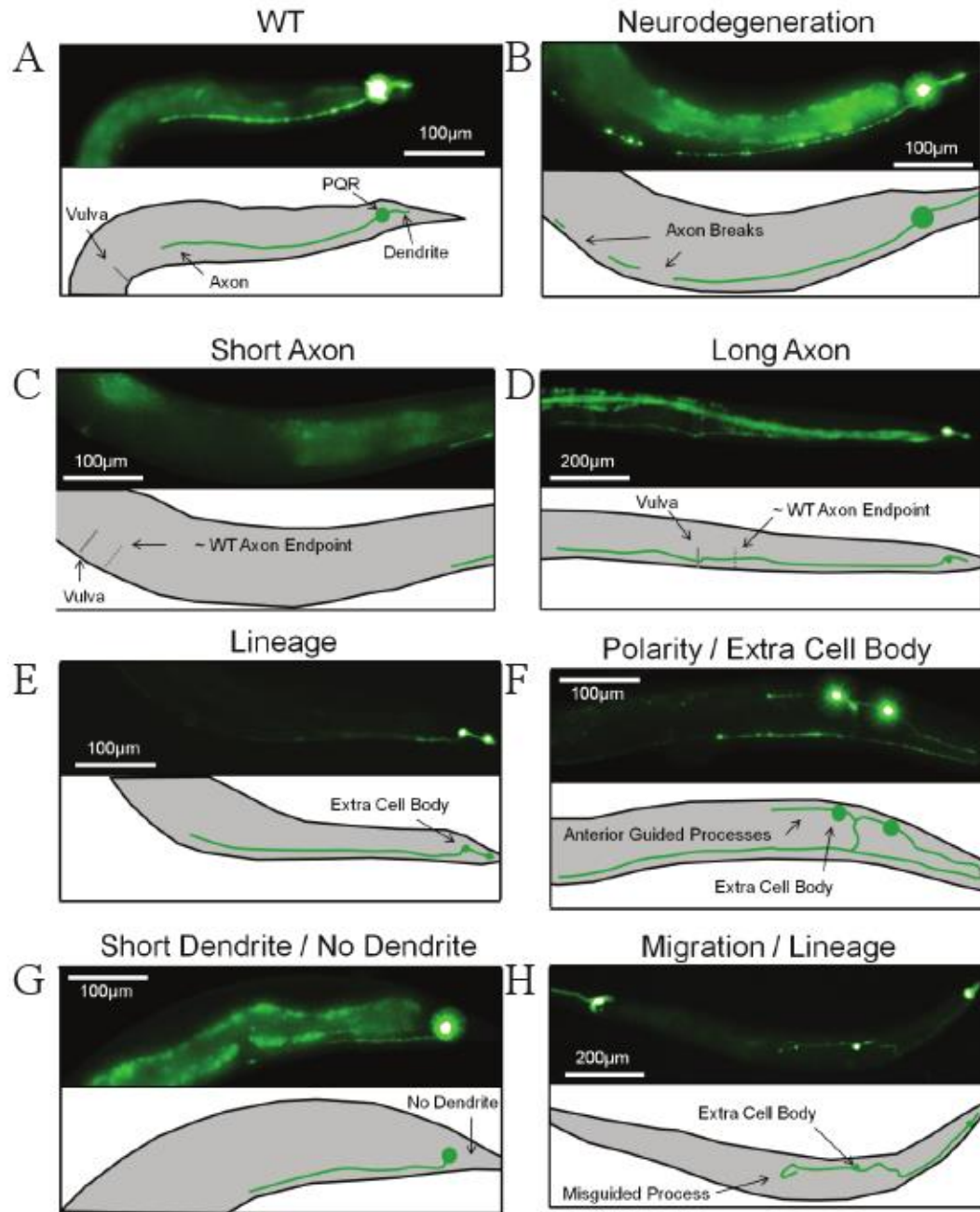


Figure 23. Example phenotypes of mutants isolated from pilot screen. All animals mutagenized from *kyIs417* shown in panel A. (A) Wild-type *kyIs417* phenotype. Arrows indicate PQR morphological segments and their relation to animal vulva. (B) Neurodegenerative phenotype of allele *a022*. Arrows indicate repeated breaks in GFP expression in axon. (C) Short axon phenotype of allele *a062*. (D) Long axon phenotype for allele *a052*. Approximate axon length for wild-type marked by arrow in diagram for panels C and D. (E) Lineage defect phenotype for allele *a053*. Arrow indicates presence of extra cell body. (F) Polarity in combination with extra cell body phenotype for allele *a060*. Anterior guided process and extra cell body marked

in diagram. (G) Short dendrite phenotype of allele *a061*. Arrow indicates lack of dendritic process. (H) Migration and lineage phenotype of allele *a051*. Arrows indicate extra cell body and a misguided process. Neurodegenerative phenotype allele *a173* not shown.

While various neurodegenerative and neural development mutants were discovered, only alleles *a173*, *a062*, and *a061* were utilized for software testing as they were the highest penetrant for neurodegenerative (24%, $n=145$), short axon (24%, $n=152$), and short dendrite (27%, $n=140$) phenotypes respectively. Figure 24 displays the penetrance of each allele compared to wild-type for their corresponding mutation. Penetrance for all mutants shown corresponds to the allele's dominant phenotype.

Alleles *a173*, *a062*, and *a061* were chosen as primary focuses for software development and characterization due to their relatively more robust phenotypes and potential role in degeneration. For example, while short axon phenotypes are often thought of as developmental defects, there is also the possibility that the neuronal process could be a remnant of an axon that has degenerated from its distal end, leaving behind what appears to be a shortened axon but is a neurodegenerative defect in actuality¹⁴². Similarly, short dendrite phenotypes may be indicative of degeneration occurring on the sensory rather than communicatory end of the neuron and also be of special interest¹⁰⁴.

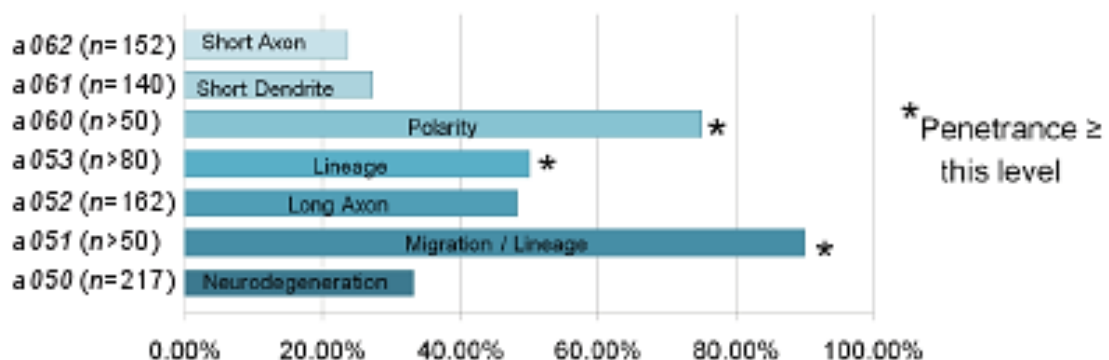


Figure 24. Penetrance of specific defects for isolated alleles. Neurodegenerative phenotype allele *a173* not shown.

6.3.3 Algorithm to detect and characterize neurodegenerative and neural development mutants

The software algorithm designed to characterize PQR neuron morphology utilizes a seven-step process involving image preprocessing, worm body detection, neuron segmentation, soma isolation, fragmented process joining, metric quantification, and phenotype classification. This computational method can be executed in real-time after a worm is loaded into the microfluidic device for imaging or off-chip at any time. Images are always acquired on-chip by capturing images from different focal planes (or acquiring a z-stack) in order to record all of the PQR neuron which typically spans multiple focal planes (as seen at magnifications of 20x or higher). After image acquisition, software characterization of the neuron is performed.

6.3.3.1 Image preprocessing, worm body detection, neuron segmentation, and soma isolation

To facilitate algorithm processing time, captured images are consolidated by taking the maximum projection along the z-axis, flattening 3D data into a 2D image³⁹. After image flattening, images are smoothed to help remove noise and facilitate binary segmentation. This is performed using an anisotropic diffusion filter to smooth image features while maintaining high contrast borders between foreground and background pixels (Figure 25A)¹⁴³.

Next, the worm body is estimated using a scaled Otsu's global threshold¹⁴⁴. Results from body segmentation are used for worm tail region separation and to limit results returned from future neuron segmentation methods to objects detected within the worm body. To detect which section of the returned worm body belongs to the tail, URX and AQR head neurons are located using Otsu's global threshold (Figure 25B). The

worm tail region is then assumed to be in opposite half of image from head neurons locations (Figure 25C).

Segmentation of the PQR neuron from background data is then performed by using the Sauvola adaptive thresholding algorithm to adjust for uneven expression of GFP and uneven illumination in images (Figure 25D)⁸⁰. The algorithm is similar to the popular Niblack segmentation algorithm, taking into account local mean and standard deviation of a region, but improves segmentation results by utilizing a hybrid global and local method to account for region class properties^{80,81}. While originally designed for text recognition and letter segmentation for documents, empirical results using the Sauvola algorithm on fluorescent images of PQR return more accurate results than global thresholding methods such as Otsu's algorithm or other local methods using adaptive algorithms^{80,144}.

Custom software using a combination of morphological openings and filters for intensity, area, and circularity are used in series to detect the PQR cell body, or soma. By altering the size and shape of structural elements passed to the function and tuning filter parameters, selective filtering of neural processes can be executed leaving only the cell body behind (Figure 25C). Animal examinations resulting in no soma detection are treated as exhibiting a wild-type phenotype, essentially discarding analysis. This is performed since dendrite and axon processes are determined by software utilizing the soma as a marker for the bipolar nature of the neuron, used to computationally separate dendritic and axonal processes. Additionally, animals with no PQR neuron, whether due to migration, lineage, or some other defect, do not fit the profile of the three degenerative and developmental phenotypes of interest.

6.3.3.2 Joining fragmented process segments

Segmentation of PQR neurons from fluorescent images is not perfect and often fails at detecting small sections of the neuron due to comparatively low signal-to-noise ratio.

Results therefore often return a fragmented process with expression mimicking a neurodegenerative phenotype (normal areas of PQR axon shown in Figure 25C-D). To correct for this issue, we implemented a probability model to estimate the connection strength between objects returned from neuron segmentation. The probability of connection between points is based on their distance to other detected objects, their angle of connection to other fragments, and their approximate length. Generally, objects which are closer together, following a direct path, and are long enough to not be considered noise (or fluorescent background structures) have the highest probability of connection (Figure 25D). A detailed explanation of the probability model can be found in subsection 6.2.3 of the materials and methods section.

6.3.3.3 Analysis of neuron morphology

After PQR has been joined together using our custom probability model, detected neuronal features are partitioned into different anatomical divisions for dendrite, soma, and axon (Figure 25E). Separating the detected process in this manner allows for each segment to contain its own distinct properties. Consequently, analysis of phenotypes can be accomplished with a greater resolution than existing systems.

6.3.3.3.1 *Quantifying neuronal process length*

Process length for PQR axon and dendrite are computed via a two-step procedure of creating an approximate spine for the process and then using this spine to calculate length. Lengths of neural processes are estimated by summing the number of pixels present in the object spine. This method is computationally faster but less precise than computing pixel distance, a method that is more accurate at estimating diagonal and curved paths; however, empirical results demonstrate similar results for both methods.

6.3.3.3.2 *Analyzing PQR fluorescent intensity to detect neurodegenerative phenotypes*

The probability model can be used to simultaneously correct for errors in segmentation, and also to analyze intensity along the PQR neuron. Once all process fragments have been analyzed and joined, neuron midlines from length measurements can be used to evaluate GFP expression by using regions of interest along each pixel of the process. While any region of interest can be used for this operation, our current method analyzes the intensity of a line aligned perpendicular to the major axis of the neuron skeleton for each pixel (Figure 25F).

6.3.3.4 Phenotype classification

Neurodegenerative phenotype classification is determined by comparing the intensity profile for the region of interest along the process. Intensity profiles for regions with normal GFP expression exhibit a characteristic peak intensity profile (Figure 25F). For regions where there is a gap, however, intensity profiles lack the typical peak shape and are prominently different (Figure 25F). For this work, an animal is considered to possess a neurodegenerative phenotype if no local maximum is detected in the intensity profile for three or more instances along the neuronal process. Details of this method are described in subsection 6.2.4 in the materials and methods section.

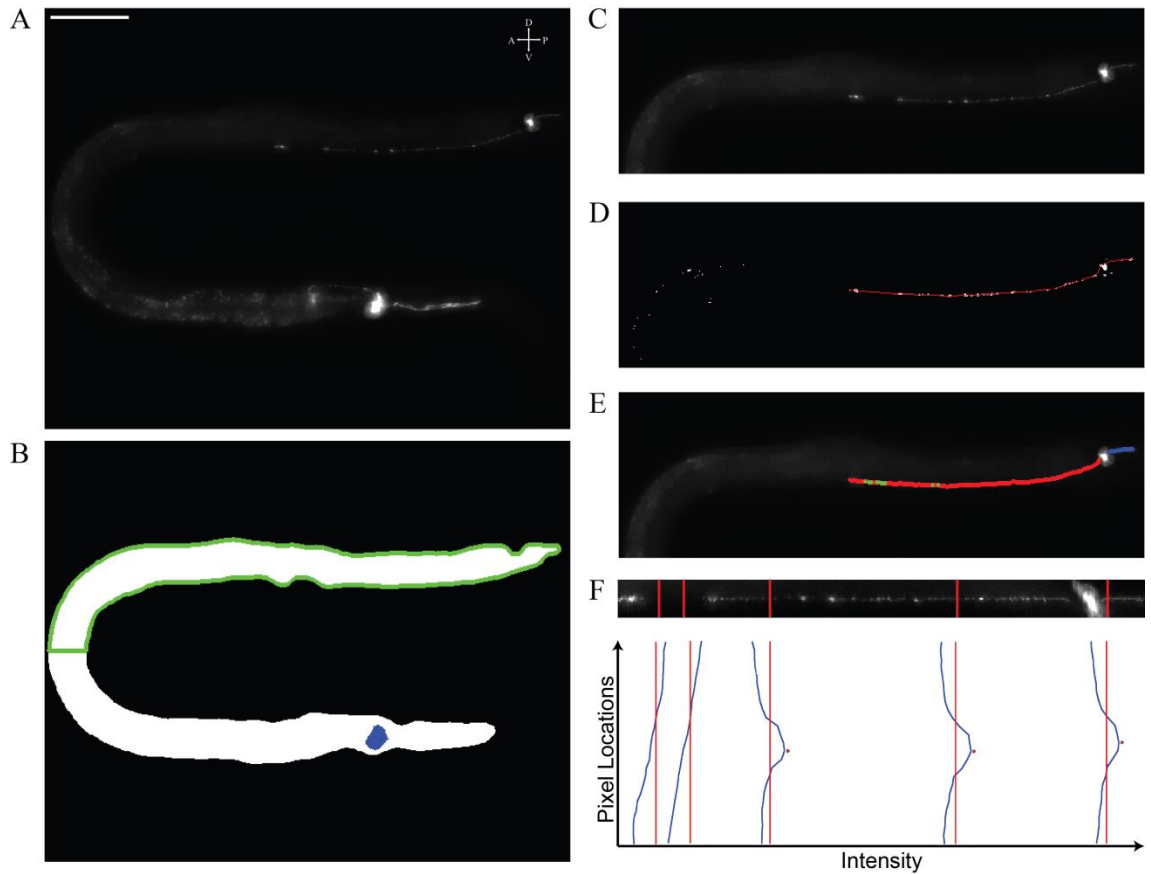


Figure 25. Software characterization of PQR neuron. (A) Smoothed maximum projection image of allele *a173* captured on-chip. Scale bar is 100 μ m. Marker designates directions for dorsal (D), ventral (V), anterior (A), and posterior (P). (B) Detected worm body by software. Head neurons (URX's) shown in blue. Body outline for determined tail region outlined in green. (C) Determined tail region of image from panel A. (D) Segmentation results of neuronal features and returned neuronal process from probability model evaluation. Segmentation results shown in white and limited to objects returned within the tail region of the animal (outlined in green in panel B). Red line shows returned connectivity between detected process fragments. (E) Results of anatomical division of PQR into axon and dendrite segments overlaid on image shown in panel C. Axon shown in red, detected breaks in GFP expression shown in green, and dendrite shown in blue. (F) Straightened neuronal process using probability model connection trajectory as process midpoint. Red lines indicate pixel measurement samples for smoothed intensity profiles shown below straightened image. Red line on intensity profile marks minimum threshold for peak detection and neurodegenerative phenotype characterization. Red dot marks peaks detected for three of five samples. All images contrast adjusted for easier viewing of neuron morphology.

6.3.4 Software validation using known phenotypes of isolated alleles

To validate the ability of our software to classify neurodegenerative phenotypes, we characterized a library of 84 images of allele *a173* captured using our microfluidic device. Every image within this library contained a neural process visually examined and confirmed to demonstrate at least one break in the PQR axonal process characterized by a gap in GFP expression, a characteristic attribute of a neurodegenerative phenotype. We qualitatively scored results of analysis based upon the performance of the probability model to correctly join segmented PQR process fragments. The three major categories were: perfect match – software results mirrored visual analysis; minor errors – software results captured most of the neuronal process, erring by detecting either too much or too little of the entire process; major errors – software results were significantly different than visual analysis. Examples of these three categories can be seen in Figure 26. Images of the allele were captured on-chip while analysis of phenotype was performed off-chip.

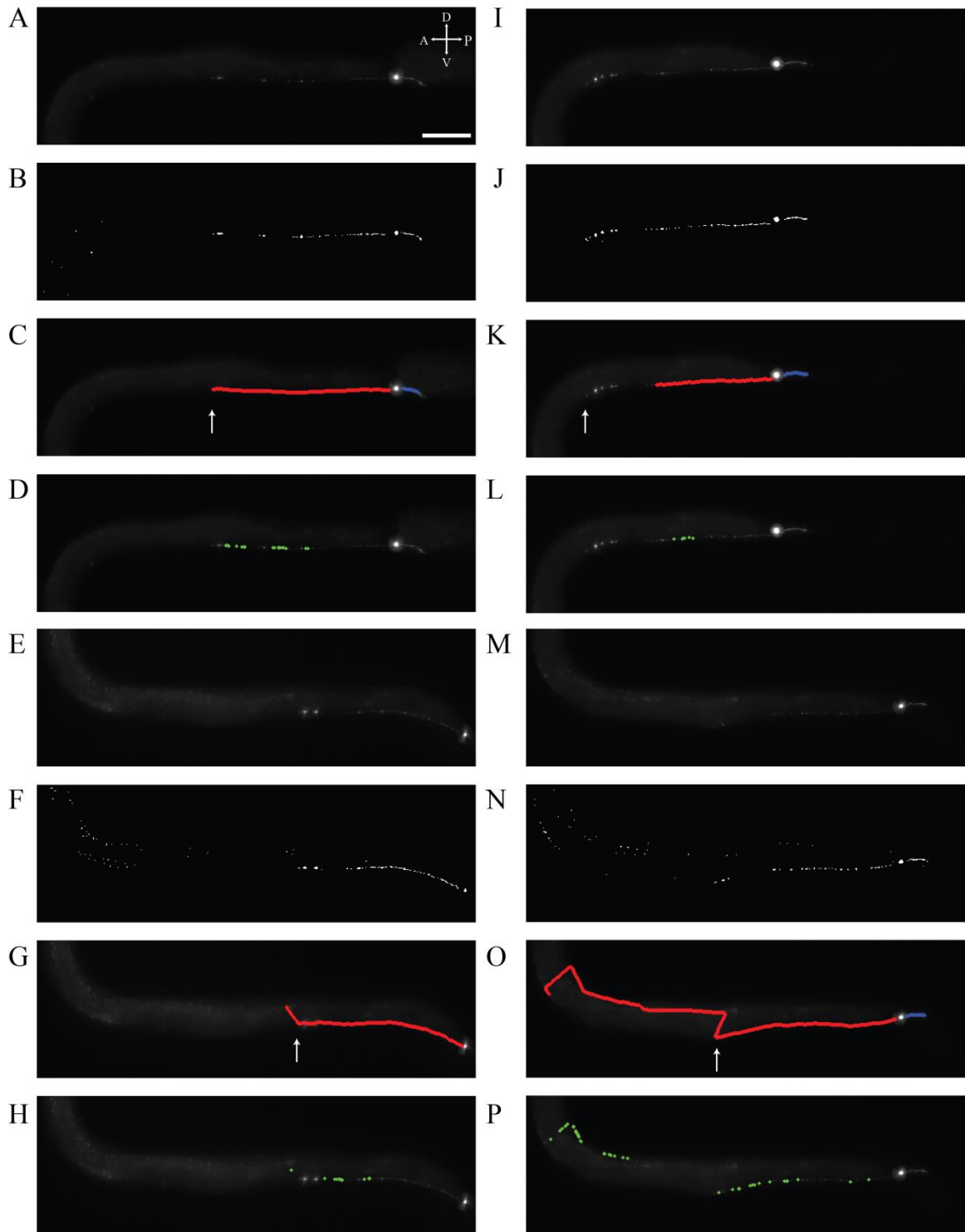


Figure 26. Qualitative accuracy examples. Representative examples for accuracy scoring: perfect match (A-D), minor error: detected too much (E-H), minor error: detected too little (I-L), or major error (M-P). First row shows the maximum projection result for each example. Second row displays binary segmentation results of respective images shown from first row. The third row shows results of using our

probability model method to join neuronal process fragments overlaid on the maximum projection image. Estimated axon and dendrite are shown in red and blue respectively. White arrow designates where neuronal process should have ended according to visual inspection. The final rows demonstrates regions along the estimated process detected to have breaks in GFP expression, overlaid on maximum projection image in green, using our intensity peak detection method. Scale bar in panel A is 100µm. Marker in panel A designates directions for dorsal (D), ventral (V), anterior (A), and posterior (P). All images contrast adjusted for easier viewing of neuron morphology.

While 84 images were in our library, 10 of these were examples of PQR neural processes that did not contain a cell body or soma in the image. These images served as negative control tests to make sure that our program did not analyze any images or detect any false positive cell bodies when no soma was present. All 10 of these images were correctly identified. Of the 74 images visually confirmed to contain a cell body, 70% of images returned results that were either a perfect match (27% or $n=20$) or with minor errors (43% or $n=32$) for PQR process detection. Low accuracy can be attributed to poor performance of software to detect PQR cell bodies. Software returned results for no soma detected for 10 images visually confirmed to contain a cell body (14% of $n=74$). Thus, joining of PQR process segments was not executed for these instances. Neglecting these 10 images and calculating accuracy for results where PQR soma was detected reveals an accuracy of 81% ($n=52$ of 64), demonstrating the utility of our method to correct for poor segmentation results using standard computer vision algorithms.

Next, accuracy of detecting neurodegenerative phenotypes was analyzed using our peak detection method for neural process intensity. Results from our image library show that our method is 75% accurate for images returned with perfect matches between PQR visual analyses and software joining of process segments ($n=15$ of 20). Results for neurodegenerative phenotype detection when taking into account perfect matches and images with minor connectivity errors drops accuracy down to 62% ($n=32$ of 52). However, this drop in accuracy can easily be explained when taking into account that scoring for minor errors includes images where not all of the neuronal process was

detected; in other words, areas with axonal breaks (characterized by a gap in GFP expression) may not have been analyzed for those images. Taking this factor into account and excluding minor errors in neuronal process connectivity where a less than the full neuronal process was detected increases accuracy back up to 75% ($n=27$ of 36). If calculating classifier performance including images where neural connectivity results returned major errors, accuracy decreases once again to 61% ($n=39$ of 64) and even down to 53% ($n=39$ of 74) if including images where no soma was detected but present; however, these results do not reflect the actual performance of the neurodegenerative classifier, as it relies heavily on the ability of the probability model to correctly join neural process segments together in order to function properly

Run times for probability model and neurodegenerative classifier execution are directly related to the complexity of analysis of fragmented process segments. The average execution time per image for PQR characterization was 9 ± 3.7 seconds (mean \pm standard deviation, $n=84$) with a maximum of 20.6 seconds required for one image within our library. Average run time for images where no soma was detected was 4.5 ± 0.5 seconds (mean \pm standard deviation, $n=20$). The average execution time for only instances where the probability model and neurodegenerative phenotype classifier were implemented did not significantly change when compared to results from all images, 10.4 ± 3.1 seconds ($n=64$).

6.4 Conclusions

As with any system, our microfluidic platform for rapid characterization and analysis of *C. elegans* neurodegenerative and neural developmental phenotypes is limited by several factors. First, overall classification accuracy of neurodegeneration is directly related to the performance of our probability model to correctly join neural processes together. Additionally, software ability to detect the PQR cell body is required for analysis of animal phenotype. These factors combined can have a great impact on overall

classification accuracy of our system, but can be compensated for by examining large numbers of animals to mitigate the effect of classification errors.

We provide a system capable of performing rapid neuron morphology analysis and classification of neurodegenerative phenotypes. With the ability to perform characterization of neuronal morphology in approximately 10 seconds, we can potentially use our method to perform automated screens for neurodegenerative and neural developmental phenotypes in real-time. This algorithm is highly parameterized and can easily be used to analyze other neurons with similar bipolar morphology and expanded for other model organisms or neuronal images with simple changes.

CHAPTER 7 CONCLUSIONS AND FUTURE DIRECTIONS

7.1 Research significance

The primary objective of this thesis was to create tools and methods to enable high-throughput screening and characterization of multiple *C. elegans* phenotypes in order to: (1) advance the state of art for automated screening technologies; and (2) use these methods to discover novel genes or cellular mechanisms responsible for various pathologies to develop potential new therapies. To accomplish these goals, I developed four approaches in microfabrication, system integration, and computer vision to solve current problems limiting small animal screening. First, I developed a passive method for animal positioning into lateral orientations within microfluidic devices by using curved geometries. Second, I used the device design coupled with computer vision algorithms to detect motor neurons and perform the first automated real-time screen for neurodegenerative *C. elegans* mutants. Third, I engineered a method to rapidly characterize animal phenotypes requiring inspection of large numbers of fluorescently labeled objects, on the order of seconds versus hours. Lastly, I devised a method to correct for segmentation defects in noisy, low-resolution environments and use this technique to classify neurodegenerative defects in neuronal processes. Specific contributions for each project are discussed further below.

The overall goal of my first project (chapter 3) was to enable rapid screening of *C. elegans* for phenotypes that required dorso-ventral orientations for inspection of fluorescently labeled phenotypes. In accomplishing this task, I designed and provided the first method for orienting *C. elegans* within microfluidic channels into specific dorso-ventral alignments. The ability to easily control worm orientation is significant because it enables high-throughput screening by providing a simple and robust method to facilitate inspection of lateral morphological features. This method provides a passive means to performing this task and can position animals into lateral orientations with up to 84%

efficiency, compared to 21% using existing methods. Using this method, we performed a pilot screen of approximately 10,000 animals and isolated six mutants with neuronal development or neurodegenerative defects, showing that our technology can be used for on-chip analysis and high-throughput visual screens. Our system accomplished this task using no anesthetics or true immobilization method, eliminating the need for additional systems, and utilized curved geometry to restrict animal movement. Even with no immobilization scheme, our system allowed visual analysis of complex neuronal morphology and complete inspection of the *C. elegans* motor nervous system consisting of 19 neurons, two nerve cords, and their interconnecting commissures between them. Additionally, this system was simple to use and was tested in the hands of biologists from Dr. Massimo Hilliard's laboratory at the University of Queensland. In the Hilliard lab, the device was further used to isolate a mutant allele independently, demonstrating the general utility of this tool to facilitate scientific discovery.

In the second project (chapter 4), I performed the first real-time screen for neurodegenerative mutants. The automated screen was performed at a rate of 300 worms per hour and resulted in the isolation of 21 alleles that suppressed a mutation in *smn-1*, a *C. elegans* homologue to the gene responsible for spinal muscular atrophy in humans. I performed this screen by combining computer vision techniques to detect neuronal cell bodies with an improved device design based on the last project. The new design simplified the fabrication process allowing for production of our devices by non-experts while maintaining passive orientation. The main intellectual contribution in this work, in contrast, was providing an automated screening platform to directly read out neural anatomy using a process over 100 times faster than existing neurodegenerative phenotype detection methods, to our knowledge, for *C. elegans*^{87,88}. While the pilot screen for this project inspected over 7,500 animals for suppression of the *smn-1* phenotype, our system provides an approach to saturate forward genetic screens that can be easily expanded to examine a multitude of phenotypes requiring fluorescent cell body detection. Thus, we

provide a widely applicable technique compatible with biological mechanisms that can be morphologically examined in *C. elegans*. Additionally, minor changes in software parameters allow for the inspection of circular objects in other applications in other model systems, i.e. not limited to *C. elegans* neurons.

For the third project (chapter 5), I modified a previous method (granulometry) to rapidly characterize large numbers of objects; this computational technique is analogous to the sieving of digital images for particles of various sizes. In this work, a morphological processing algorithm was used to rapidly characterize *C. elegans* lipid droplet distributions, an improvement in throughput of over three orders of magnitude when compared to standard manual methods of analysis. We validated this technique by recreating similar distributions to results measured by manual methods in published work between mutant and wild-type populations and for animals fed different diets^{124,125}. Additionally, we show that our method can be applied to low quality images captured using epifluorescent microscopes, mimicking published data captured from higher fidelity systems. Our presented method can analyze hundreds of objects on the order of seconds, enabling the use of this technology to perform automated screens for mutations that affect lipid storage. This process is extremely difficult to perform by standard methods, which is both time consuming and inaccurate. The scientific contribution here could potentially facilitate the discovery of genetic and molecular mechanisms for obesity and its relation to other diseases such as diabetes, coronary heart disease, and reduced life expectancy¹⁴⁵⁻¹⁴⁷.

The final contributions of the thesis were the implementation of a probabilistic model to correct for errors in computer vision segmentation techniques, and the accompanying method to classify neurodegenerative phenotypes (chapter 6). Using these techniques, I was able to correctly identify neuronal processes with up to an 80% accuracy for images where segmentation results returned incomplete and fragmented objects. Additionally, accuracy of neurodegenerative phenotype classification after

probability model implementation was 75% for correctly processed images. Like our previous technologies, run time for our software methods was rapid, averaging less than 10 seconds for model execution and phenotype classification combined. This would enable real-time decision-making for performing genetic screens. Our method is highly parameterized and can be adapted to other neurons with similar bipolar morphology, permitting the use of our software method for various applications.

In conclusion, the presented work in this dissertation provides methods to analyze various biological phenotypes generalized into three categories: detection of circular cell bodies in low numbers; characterization of circular objects in dense volumes with large amounts of occlusion; and segmentation of curved tubular structures. These shapes and conditions can be widely utilized in various fields of biomedical science and are not limited to *C. elegans* research. By combining computer vision analysis methods with microfluidic technology, we demonstrate the capability to characterize the aforementioned phenotypes, enabling automated screens requiring minimal human intervention, and the possibility to reach screen saturation in months versus years. Mapping these genetic mutations may one day help to elucidate the detailed mechanisms of how complex processes function in humans.

7.2 Future directions

The work presented in this dissertation presents technologies in their infancy in terms of impact and exposure. This thesis is a proof of concept demonstrating the potential of our hardware and software methods for specific applications. A discussion of future improvements follows below.

While the first project (chapter 3) provides a method for orienting *C. elegans* within microfluidic devices, positioning of nematodes is limited to a single orientation. This dorso-ventral orientation places animals on their side and is commonly seen during locomotion and when nematodes are examined on agar pads. While we provide a means

for consistent orientation, future work should focus on providing an orientation method for body positions not commonly seen, facilitating inspection of hard to examine phenotypes. Additionally, by placing animals on their ventral or dorsal body with their lateral sides against channel walls, symmetric body structures (most neurons are bilaterally symmetric) can be easily examined. Preliminary work in our lab has shown promising results of using channels with different steps in channel height to promote passive positioning of nematodes into this orientation, similar to using curved structures to encourage body bending. The long-term goal would be to create a device design that would passively orient *C. elegans* into both dorso-ventral and lateral orientations, allowing for inspection of the full animal body.

Future work for our second project (chapter 4) could focus on continuing with automated screens until saturation. To accomplish this goal, software should be revisited and optimized to lower false positive rates for both detection of motor neurons and suppressor mutant classification. Another method to lower these rates is to use a *smn-1* RNAi strain with a different transgenic marker. This has the potential to significantly improve software results as a large percentage of neuron detection and mutant classification error can be attributed to detection of fluorescent RNAi co-injection markers present in the head and tail of the animal. Furthermore, to expand upon potential discoveries for genes and pathways involved with *smn-1*, forward genetic screens for enhancer mutants along with mutants from screening mutagenized wild-type populations should be performed. The long-term goal of this project is to saturate multiple screens involved with *smn-1*, but can be expanded to other phenotypes requiring analysis of fluorescent cell bodies.

To utilize the full capability of our presented method, future work concerning the third project (chapter 5) should focus on performing on automated screen using an epifluorescent microscopy system. Performing this screen and isolating various alleles will validate our proposed technology and provide a means to continue forward with

automated experiments. Future work using this system and computational method should include further characterization of computational limitations of the modified granulometry algorithm to discover differences in lipid distributions from known mutants with subtle differences in size. Similar to the proposed work for the previous project, automated genetic screens should be performed for enhancers and suppressors of known mutations after saturating screens for mutants isolated from mutagenized wild-type populations. Should software fail to distinguish between subtle phenotypes using epifluorescent systems, genetic screening can be attempted using rapid, high-quality imaging systems such as spinning disk confocal setups.

Future work for the fourth project (chapter 6) should focus on optimizing software methods in multiple areas including neuronal cell body detection, joining of neuronal process fragments, and neurodegenerative phenotype classification. Ideal accuracy values to be obtained from each of these processes is approximately 95%, as neurodegenerative phenotype classification depends on both cell body detection and correct probability model execution for perfect analysis. Given a 95% accuracy for each process, final accuracy for detecting a neurodegenerative phenotype when present would be approximately 86%. Once optimized, an automated screen searching for neurodegenerative animals should be performed to validate the software process and presented methods. Like our previous work, the goal of this technology is to saturate screens to search for genes involved neurodegenerative processes, and accompanying suppressors and enhancer screens should be performed.

Ultimately, the presented research and methods are only as effective as the amount of use they receive. We strive to provide tools for research scientists to enable efficient and high throughput experimentation. Just like any other product, our equipment and methods should be tailored for our end users, with simplicity and ease of use at the forefront of concerns. With this end goal in mind, future work can attempt to further simplify microfluidic devices, both in setup and operation, and the integration of software

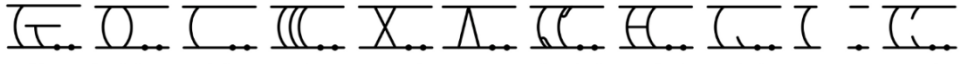
components into selectable modules of an analysis pipeline (as in software packages like CellProfiler). Device simplification should focus on reducing the amount of active components (pneumatic valves for fluid control) to decrease the number of potential failure points and external equipment required for operation. Additionally, optimizing graphical user interfaces to the levels of widely available and popular software packages by enabling drag and drop capabilities to provide methods for users to create a specific analysis pipelines, mobile operation and alerts, and standardized interfaces would significantly decrease software operation difficulty.

Lastly, the packaging and repeatability of device performance should be optimized for commercial use in order to provide deliverable products to end users. This can be accomplished by providing standard form factors for pin-to-device interfaces while using products that promote ease of connection between tubing and fluid inputs / outputs. Additionally, device stiffness can be measured to ascertain fluctuations in rigidity due to different PDMS manufacturing batches or device age to reduce the variability in device valve operation.

APPENDIX

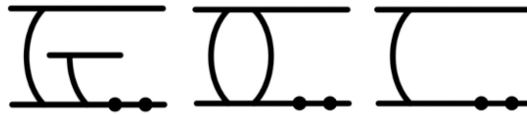
A.1. Laterally Orienting *C. Elegans* Using Geometry At Microscale For High-Throughput Visual Screens In Neurodegeneration And Neuronal Development Studies

Proportion of adult animals with defect (%)



Strain	guidance	handedness	missing	extra	crossed	merged	branched	bridged	short	gap	break	n scored
<i>juls76</i>	1.0	35.0	24.3	3.9	44.7	62.1	1.0	0	1.9	8.7	1.9	103
<i>a070</i>	100	99.1	100	not scored	not scored	not scored	not scored	not scored	not scored	100	not scored	110
<i>a071</i>	80.2	51.5	44.6	13.9	31.7	60.4	66.3	1.0	17.8	88.1	0	101
<i>a073</i>	29.1	62.1	60.2	3.9	27.2	53.4	0	2.9	0	17.5	0	103
<i>a074</i>	58.6	58.6	48.5	12.1	47.5	61.6	27.3	4.0	4.0	82.8	1.0	99
<i>a077</i>	25.7	35.2	65.7	1.0	50.5	52.4	0	0	0	21.0	1.9	105
<i>vd029</i>	68.3	95.0	100	0	25.7	16.8	2.0	8.9	5.9	100	0	101
<i>a070</i> outcrossed	86	90	100	0	14	18	4	4	2	98	2	50
<i>a071</i> outcrossed	88	52	56	12	42	60	28	4	4	94	0	50
<i>a073</i> outcrossed	41.8	52.7	61.8	1.8	21.8	61.8	12.7	0	0	12.7	0	55
<i>a074</i> outcrossed	45.1	54.9	60.8	7.8	41.2	68.6	5.9	9.8	0	80.4	3.9	51
<i>a077</i> outcrossed	12	44	42	8	54	68	4	0	2	30	2	50
<i>vd029</i> outcrossed	76	98	100	0	18	14	16	0	0	98	0	50
<i>a070</i> heterozygous	0	54	48	0	42	44	4	0	0	2	2	50
<i>a071</i> heterozygous	0	14	18	2	46	52	2	0	0	0	0	50
<i>a073</i> heterozygous	1	23	30	1	40	52	1	0	0	0	0	100
<i>a074</i> heterozygous	0	19	40	2	38	35	2	0	0	1	0	100
<i>a077</i> heterozygous	8	32.5	63	0.5	39	42.5	3	1.0	0.5	12	0.5	200
<i>vd029</i> heterozygous	0	28	50	0	36	36	4	0	0	4	0	50
<i>a071 a077</i> double heterozygous	9.1	36.4	29.5	0.0	54.5	52.3	11.4	0	0	18.2	0	44

Figure 27. Proportion of adult animals in a population with at least one incidence of each independent defect (%).



Strain	guidance	handedness	missing	<i>n</i> scored
<i>juls76</i>	1.4	1.4	2.4	211
<i>a070</i>	44.6	24.8	91.7	121
<i>a071</i>	87.3	0	19.5	118
<i>a073</i>	0	5.8	0	103
<i>a074</i>	14.7	26.5	1.0	102
<i>a077</i>	10.6	17.7	5.3	113
<i>vd029</i>	28.8	46.2	100	104

Figure 28. Proportion of L1 animals in a population with at least one incidence of each independent defect (%).

Strain	DD1			DD2			DD3			DD4			DD5			DD6		
	G	O	C	G	O	C	G	O	C	G	O	C	G	O	C	G	O	C
<i>juls76</i>	0.5	0	0	0	0.9	0.5	0	0.5	0.5	0.9	0	0.9	0	0	0.5	0	0	0
<i>a070</i>	25.6	0.8	30.6	4.1	5.8	15.7	4.1	9.1	53.7	3.3	3.3	72.7	0	1.7	17.4	12.4	5.0	33.1
<i>a071</i>	1.7	0	1.7	1.7	0	0.8	54.2	0	8.5	66.1	0	6.8	21.2	0	3.4	5.9	0	0.8
<i>a073</i>	0	1.0	0	0	1.9	0	0	3.9	0	0	0	0	0	0	0	0	0	0
<i>a074</i>	8.8	8.8	1.0	1.0	8.8	0	1.0	2.0	0	3.9	6.9	0	0	7.8	0	0	3.9	0
<i>a077</i>	3.5	1.8	2.7	3.5	5.3	0.9	0.9	2.7	1.8	1.8	3.5	0	1.8	2.7	0	0	2.7	0.9
<i>vd029</i>	13.5	26.0	0	5.8	20.2	5.8	0	1.0	92.3	0	1.9	95.2	1.9	2.9	88.5	9.6	5.8	65.4

Figure 29. Penetrance of defects per cell in L1 populations with at least one incidence of each independent defect (%).

A.2. Automated Screening Of *C. Elegans* Neurodegeneration Mutants Enabled By Microfluidics And Image Analysis Algorithms

A.2.1. Motor neuron segmentation

Cell bodies of motor neurons were segmented from live images using a four step process. First, images were smoothed using an anisotropic diffusion filter to facilitate neuron

segmentation by reducing noise while preserving edges¹⁴³. This filter was modified and released in the public domain by David Lopes and is available for download on MATLAB® Central File Exchange (<https://www.mathworks.com/matlabcentral/fileexchange/14995>). Second, the smoothed image was segmented for features of interest by applying two global image thresholds: the first threshold is used to segment the worm body, while the second is used to segment potential neuronal cell bodies. Potential neurons not within the segmented worm body area were discarded.

The third step of our process filtered out results thus far by shape and size. To filter by shape, a morphological filtering operation (using a disk shaped structuring element) was used to remove non-circular objects from the segmented image. Afterwards, all potential cell bodies were compared to minimum and maximum size thresholds. All objects comprised of too few or too many pixels were removed, leaving only potential cell bodies valid for our specified size range. The final step in our process was to use a mean filter to remove any RNAi co-injection markers or other objects falsely identified as motor neurons. The mean filter, which is typically used for smoothing images, was applied to the binary image of detected objects, combining objects within close proximity of each other, as is normally the case for RNAi co-injection markers in the head region. An additional size filter was then used to remove combined objects from the final output.

A.2.2. Automated system operation

To load an animal when none is detected, a command is sent to our off-chip valve control board to actuate the solenoid valve configuration and input flow required for worm loading. Once an animal is detected, it is given a period of two seconds (referred to as the loading time) to reach the correct position region. If the animal fails to reach this region within the allotted loading time, the flush and input flows are toggled on and off

respectively for a period of one second to reset flow within the device and aid the animal into the correct position for imaging. The system will begin image acquisition regardless of the animal's placement within the device if the animal has failed to reach the correct position region after a total of four seconds since detection (referred to as the moving time).

Once in the correct position or if the moving time for the animal has expired, a command is sent to the valve control board to actuate all valves and to stop all flow within the device. Briefly, the loading valve and flush channel flow are toggled off and on respectively to reverse fluid flow within the device towards the input to remove any extra animals present in the imaging region. Next, valves at the entrance and exit to the curved channel are toggled off and on for 50msec to reposition any part of the worm body that might be obstructed. Lastly, the system is given one second to provide time for all fluid flow to stop before an image of the animal is acquired.

After image capture, animal phenotype is analyzed using the previously described methods to determine the number of D-type motor neurons present. After classification, the animal is sorted to the mutant channel or wild-type channel output by sending the appropriate valve configuration to the valve control board and activating input and flush channel flow. Animals are given two seconds to exit the imaging area (referred to as the exit time) of the device during system sorting before the flush flow is toggled off and on to facilitate worm sorting. Once an animal is no longer detected, the entire process of loading, phenotype analysis, and sorting is repeated.

All time limits for system processes were set to values based off of empirical data. Our valve control board (Ultimarc PPACDSP+LU04) communicated with solenoid actuators (Asco Scientific 18800056) and pinch valves (Cole Parmer EW-98302-10) tuned for use with varying pressures controlled by four separate regulators (McMaster 43275K14).

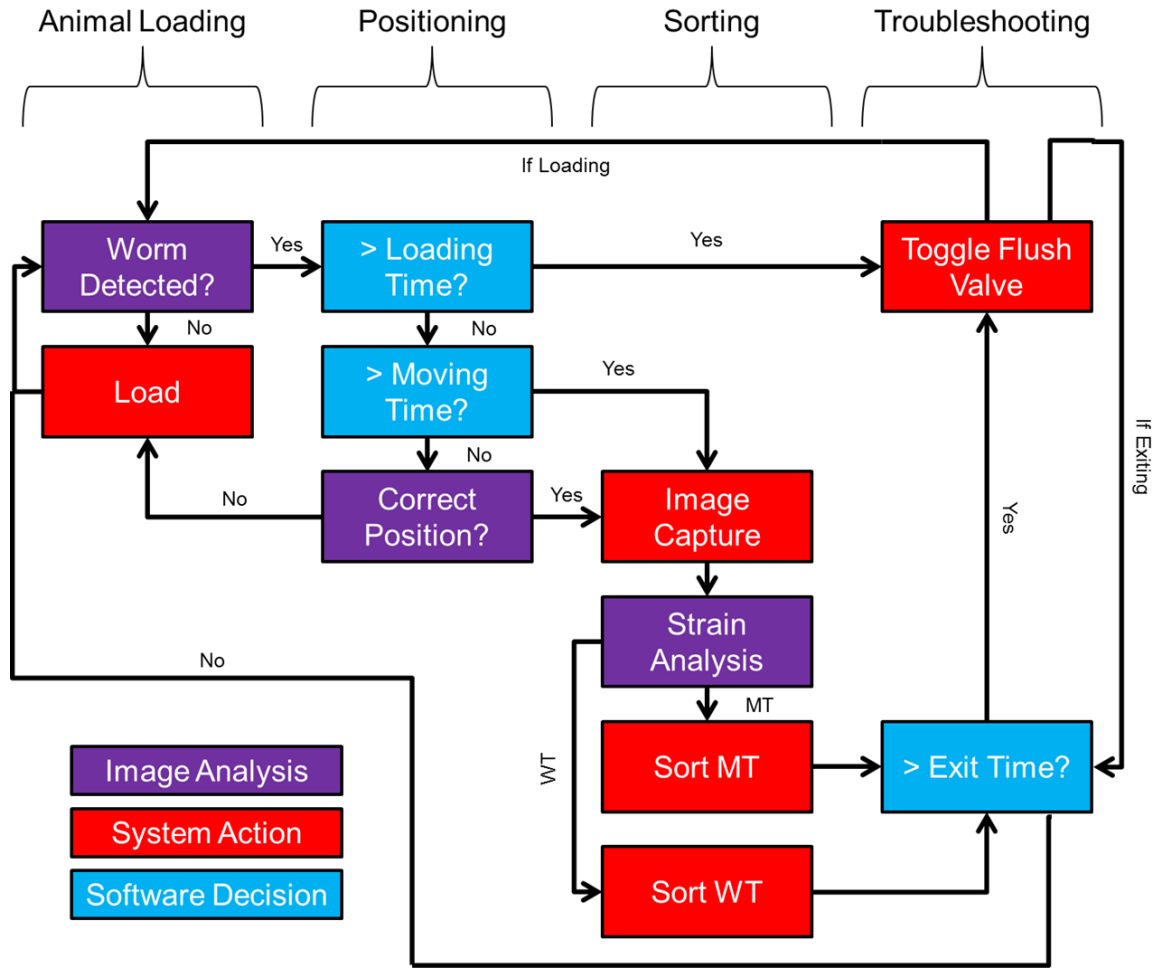


Figure 30. System level diagram of operation. System operation can be separated into three areas involving image analysis, system action, or software decisions based on timing. Each column represents a different state of system operation involving animal loading, positioning, and sorting. Troubleshooting column is specific only to toggling of the flush valve to aid with fluid handling and worm placement.

A.2.3. Neuron distribution for alleles isolated from same F1 population

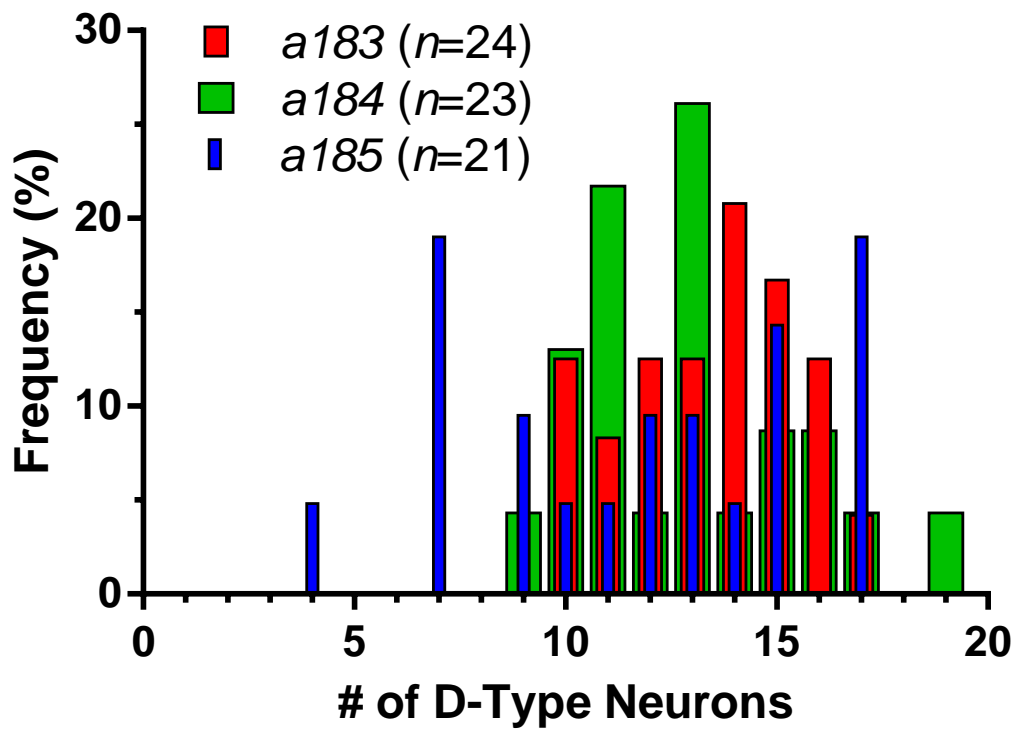


Figure 31. Histogram for alleles *a183*, *a184*, and *a185*. Only data from manual scoring, not image analysis, was used for this figure.

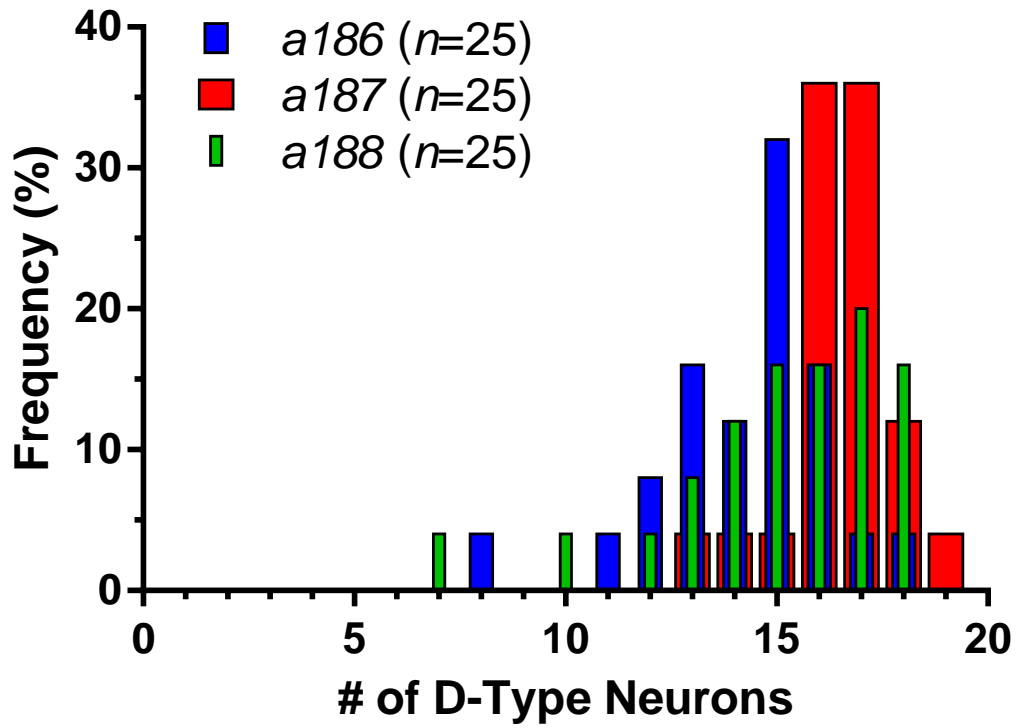


Figure 32. Histogram for alleles *a186*, *a187*, and *a188*. Only data from manual scoring, not image analysis, was used for this figure.

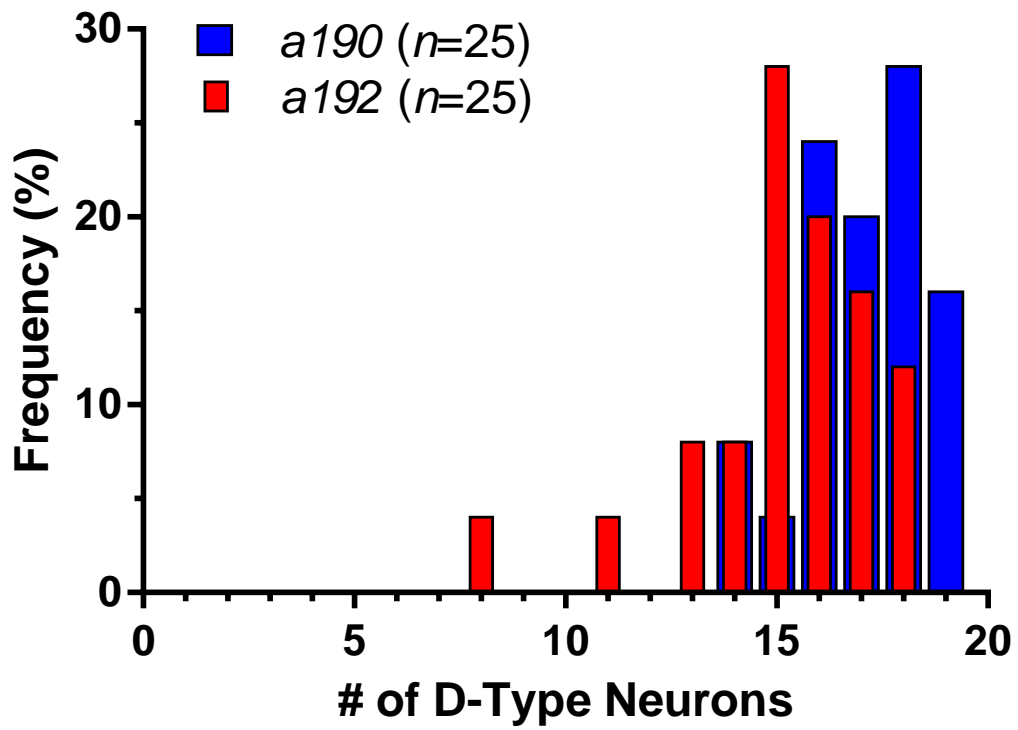


Figure 33. Histogram for alleles *a190* and *a192*. Only data from manual scoring, not image analysis, was used for this figure.

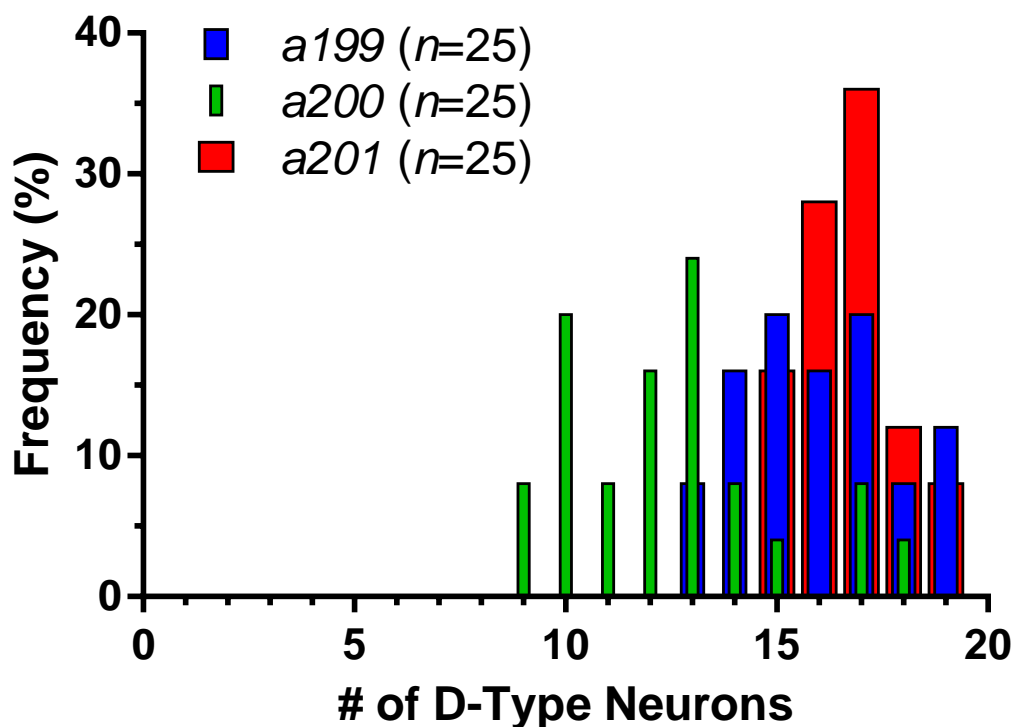


Figure 34. Histogram for alleles *a199*, *a200*, and *a201*. Only data from manual scoring, not image analysis, was used for this figure.

Table 2. Number of D-type motor neurons detected for all alleles. All animals cultured at 20°C until gravid adults.

D-Type Motor Neurons																					
#	a1	a1	a1	a1	a1	a1	a1	a1	a1	a1	a1	a1	a1	a1	a1	a1	a1	a2	a2	a2	a2
	82	83	84	85	86	87	88	89	90	92	93	94	95	96	97	98	99	00	01	02	03
1	12	12	11	12	15	18	16	16	15	17	16	15	18	15	13	16	15	10	18	12	13
2	12	10	13	17	15	16	15	17	16	18	14	15	18	16	13	15	19	11	19	10	15
3	7	11	10	7	13	16	12	14	17	13	12	14	18	15	17	14	16	18	17	13	16
4	11	14	17	13	14	16	7	10	16	11	12	15	19	15	12	15	13	10	15	11	18
5	12	12	11	9	14	15	16	13	17	16	13	16	17	14	14	12	19	13	17	7	16
6	13	15	10	17	11	17	16	16	17	16	15	17	18	14	13	16	17	17	16	12	19
7	15	14	13	17	15	18	18	18	16	15	15	15	17	13	12	15	17	14	18	12	17
8	12	13	14	11	16	16	10	17	19	17	17	14	19	15	13	15	18	13	17	14	17
9	16	15	11	10	15	17	14	16	16	16	17	9	18	14	10	17	16	12	17	13	14
10	12	10	16	7	15	18	17	17	18	15	15	15	19	14	11	15	15	15	18	12	14

11	12	14	9	15	12	16	18	11	18	13	16	13	17	16	9	15	14	10	17	17	14
12	12	13	13	13	15	17	15	17	14	16	16	18	17	14	12	19	15	13	16	13	19
13	13	13	12	15	16	17	17	18	18	8	13	15	19	17	13	17	13	10	17	12	15
14	15	14	19	17	15	17	14	15	17	15	13	13	15	15	13	11	17	14	16	14	19
15	15	15	11	12	8	16	17	12	17	17	17	12	17	14	11	13	18	12	16	16	15
16	12	10	13	14	13	17	15	18	16	15	13	13	18	14	11	14	17	13	17	12	18
17	11	14	13	15	18	14	18	14	18	15	17	14	17	19	15	14	15	11	17	9	17
18	13	16	11	4	17	16	13	13	19	17	17	17	17	16	12	10	14	13	15	15	17
19	14	12	15	9	12	16	16	15	19	14	15	17	19	16	16	14	17	12	15	16	18
20	16	17	10	7	16	19	17	15	14	15	14	14	14	16	9	13	14	9	19	13	17
21	11	16	16	7	14	13	18	16	19	16	15	13	17	17	10	13	16	12	16	16	15
22	15	11	13		16	16	13	19	18	18	16	11	18	14	14	15	14	9	15	13	14
23	6	15	15		13	17	17	19	16	18	15	17	17	14	13	15	19	17	16	14	16
24	13	16			13	17	14	15	18	14	14	16	18	16	12	14	16	10	17	8	17
25	14				15	17	15	12	18	15	16	15	16	16	9	16	15	13	16	12	15
A																					
V	12	13	12	11	14	16	15	15	17	15	14	14	17	15	12	14	16	12	16	12	16
G	.6	.4	.9	.8	.2	.5	.1	.3	.0	.2	.9	.5	.5	.2	.3	.5	.0	.4	.7	.6	.2
S																					
E	0.	0.	0.	0.	0.	0.	0.	0.	0.	0.	0.	0.	0.	0.	0.	0.	0.	0.	0.	0.	0.
M	09	08	11	19	08	05	10	10	06	09	06	08	05	05	08	08	07	10	04	10	07

A.3. High throughput characterization of spherical objects using modified granulometry algorithm for rapid characterization of *C. elegans* lipids

A.3.1. Specialized software method for epi-flourescent data

To compensate for images with high amounts of background and low signal-to-noise ratios (as seen in epiflourcent data), we implemented a specialized version of our algorithm to mitigate the effects of poor image quality. The first several deviations from our normal method occur during preprocessing. First, images are not doubled in size during epi-flourescent analysis as resolution of the imaging system is too low to detect small objects accurately; therefore, this step is avoided all together in order to increase the computational run time of our process. Second, morphological processing to remove

noise and enhance image contrast is performed using three different size structuring elements (SE, disk shaped of radius 10, 20, and 30 pixels) instead of using a single SE of size 30. This is performed as empirical results show that removing objects larger than what granulometry is processing during morphological opening operations improves results (i.e. openings for SE sizes one through nine return better results on a preprocessed image of radius size 10 than 20 or 30; openings for SE sizes 10 through 19 return better results for a preprocessed image of radius size 20 than 30, and so on).

The next difference is that granulometry is performed on each preprocessed image (three total, one of radius size 10, 20, and 30). SE's during morphological openings cannot exceed the size of SE used during preprocessing or all objects from the image will be removed (i.e. morphological opening of radius size 15 cannot be performed on a preprocessed image that used a radius size of 10). Thus, for the image preprocessed with a SE of size 10, granulometry is performed using SE's of size one through nine; for the image preprocessed with a SE of size 20, granulometry is performed using SE's of size 10 through 19, and so on.

Lastly, granulometry results for all three preprocessed images are compared, and the result with the largest normalized size distribution (Equation (5)) is used along with its corresponding preprocessed image for the remainder of analysis. In this manner, granulometry is optimized for the preprocessed image that returns the largest removal of objects when performing granulometry.

A.4. Automated characterization of neurodegenerative and neurodevelopment defect mutations in *C. elegans*

A.4.1. Image preprocessing, worm body detection, neuron segmentation, and cell body isolation

Acquired z-stacks were consolidated into 2D images using the maximum intensity projection of every pixel along the z-axis. After image flattening, an anisotropic filter was

used to smooth the flattened image. This filter was released in the public domain by David Lopes and is available for download on MATLAB® Central File Exchange (<https://www.mathworks.com/matlabcentral/fileexchange/14995>). Segmentation of the smoothed of image was then performed using the Otsu algorithm in order to detect the worm body, estimate URX and AQR head neuron locations, and determine the worm tail region¹⁴⁴. Different scales were used on the returned Otsu threshold for worm body and neuron detection. Additionally, a circular averaging filter was also used in order to smooth the returned animal body.

When segmenting neuronal features, the Sauvola algorithm was used in place of Otsu. The Sauvola algorithm uses an adaptive threshold (T) to determine a binary image (B) from the image I using the following equations

$$B(x, y) = \begin{cases} 1, & I(x, y) \geq T(x, y) \\ 0, & I(x, y) < T(x, y) \end{cases} \quad (21)$$

$$T(x, y) = m(x, y) + \left\{ 1 + k \times \left[\frac{s(x, y)}{R} - 1 \right] \right\} \quad (22)$$

where $m(x, y)$ and $s(x, y)$ are the mean and standard deviation respectively for the windowed region centered around pixel (x, y) , k is a positive scaling value, and R is the dynamic range of the standard deviation (set to the maximum value of $s(x, y)$ for all (x, y))⁸⁰. Window used for segmentation was disk shaped and set to a size determined by empirical results.

Following segmentation, PQR soma detection was accomplished by performing a morphological opening on the binary image $B(x, y)$ using a disk shaped structuring element approximately equal in size to PQR cell bodies. Results from the opening operation were then filtered by area to meet minimum and maximum thresholds. Lastly,

remaining objects were filtered by eccentricity, stated by MATLAB® as the ratio of the distance between the foci of an object and its major axis length. All thresholds for shape and size filters, including scaling variables, were determined from empirical data.

A.4.2. Connectivity model used for joining PQR segments

Once called upon, software for connecting PQR segments was repeated until either of the following conditions occurred:

1. the probability of connection for current points fell below a connection threshold
2. only one object remained in the image

While in this loop, software repeated a process involving:

- deleting “invalid” objects
- reassigning current evaluation points after object deletion
- estimating the probability of connection between the current evaluation point and all other points in the image
- connecting points together on the condition that the connection threshold is met

If either condition for loop termination was met, loop execution was terminated and software would return the largest object (determined by number of pixels), assumed to be the PQR neuron. All thresholds and weights for probability functions were set based on empirical data. Points with probabilities of connection greater than threshold values were connected using the integer-coordinate line drawing algorithm provided by MATLAB®.

A.4.3. Deleting invalid objects

An object was considered to be invalid primarily based upon the number of endpoints detected for the object. We expect the PQR neuron to be a single process extending from the sensory tip of its dendrite to the end of its axon, an ideal that possesses only two endpoints.

To correct for objects with many branched structures, we detected and deleted all branch points by removing a centered 3x3 neighborhood around each branch point location. Next, all objects below a minimum length threshold were removed and deemed to be unimportant. Then, the number of endpoints per each object was calculated, and any objects with more than a set threshold of endpoints were removed (performed as an assurance in the case branch points were missed during the previous step). Lastly, the current evaluation point being considered for connection was reassigned to a different pixel location if the object that it was a part of was removed by previous filtering operations. Points requiring adjustment were assigned to the closest valid endpoint of the current image.

A.4.4. Reassigning current evaluation points and dendrite process selection

After removing invalid objects, the location of the current evaluation point was relocated to the most anterior endpoint of the current object along the major axis. This was performed in order to keep connection of objects to proceed in an posterior to anterior direction.

A special case for point relocation is the first time the main probability function was executed. This is performed in order to best determine what object to use and consider as the PQR dendrite process. For this case, a circular area around the soma centroid was set and used as a search area, with all objects within this area considered as a possible dendrite process. To determine which object to use, the main probability loop was recursively executed for each potential dendrite option, temporarily storing each result. After all options had been evaluated, the returned result with the longest connected process (measured by the total number of pixels) was used as the dendrite object.

A.4.5. Estimating probability of connection

The probability of connection was calculated after computing the distance and angle of connection between the current point and all other end points in the image. The length of

each object in the image was also approximated prior to probability calculations. Probability equations for different metrics were arbitrarily decided upon using empirical data and based off of equations used for studying neuroanatomy¹⁴⁸.

Probabilities of connection for all points connecting to endpoints from the same object as well as themselves were set to -1. Distance and length probability functions are described in text and do not require further detailed explanation. Details about angle probability calculation can be found below.

A.4.6. Calculating angle probability of connection

Angle probability was determined by grouping end points into bins determined by the angle threshold. Preferred bin direction was decided upon by using the grouping of endpoints with the highest quantity of points within the threshold angle grouping range. All endpoints of an object were required to be within the specified angle range in order to be considered a valid object for evaluation within the bin. Average angle differences for all endpoints within the preferred bin direction were then used as $\overline{\theta_B}$ in equation 16. As all angles were grouped into bins with differences limited by the angle threshold, all probabilities calculated from equation 19 were positive.

REFERENCES

- 1 Kaletta, T. & Hengartner, M. O. Finding function in novel targets: C-elegans as a model organism. *Nature Reviews Drug Discovery* **5**, 387-398 (2006).
- 2 Hobert, O. in *WormBook* (ed The C. elegans Research Community) (WormBook, 2005).
- 3 Chalfie, M. & White, J. in *The Nematode Caenorhabditis Elegans* (ed William B. Wood) Ch. 11, 337-392 (Cold Spring Harbor Laboratory Press, 1988).
- 4 Hart (ed.), A. C. in *WormBook* (ed The C. elegans Research Community) (WormBook, 2006).
- 5 Fire, A. *et al.* Potent and specific genetic interference by double-stranded RNA in *Caenorhabditis elegans*. *Nature* **391**, 806-811 (1998).
- 6 Altun, Z. F. & Hall, D. H. *WormAtlas*, <<http://www.wormatlas.org>> (2002-2006).
- 7 C elegans Sequencing Consortium. Genome sequence of the nematode C-elegans: A platform for investigating biology. *Science* **282**, 2012-2018 (1998).
- 8 Nagy, A., Perrimon, N., Sandmeyer, S. & Plasterk, R. Tailoring the genome: the power of genetic approaches. *Nature Genetics* **33**, 276-284, doi:10.1038/ng1115 (2003).
- 9 Shaham (ed.), S. in *WormBook* (ed The C. elegans Research Community) (WormBook, 2006).
- 10 Jorgensen, E. M. & Mango, S. E. The art and design of genetic screens: *Caenorhabditis elegans*. *Nat Rev Genet* **3**, 356-369 (2002).
- 11 Hilliard, M. A. & Bargmann, C. I. Wnt signals and frizzled activity orient anterior-posterior axon outgrowth in C-elegans. *Developmental Cell* **10**, 379-390 (2006).
- 12 Antebi, A., Norris, C. R. & Hedgecock, E. M. in *C. Elegans II* (eds Donald L. Riddle, Thomas Blumenthal, Barbara J. Meyer, & James R. Priess) Ch. 21, 583-610 (Cold Spring Harbor Laboratory Press, 1997).
- 13 Arimura, N. & Kaibuchi, K. Neuronal polarity: from extracellular signals to intracellular mechanisms. *Nature Reviews Neuroscience* **8**, 194-205 (2007).
- 14 Adler, C. E., Fetter, R. D. & Bargmann, C. I. UNC-6/Netrin induces neuronal asymmetry and defines the site of axon formation. *Nature Neuroscience* **9**, 511-518 (2006).
- 15 Hao, J. C. *et al.* C-elegans slit acts in midline, dorsal-ventral, and anterior-posterior guidance via the SAX-3/Robo receptor. *Neuron* **32**, 25-38 (2001).
- 16 Dimitriadi, M. & Hart, A. C. Neurodegenerative disorders: Insights from the nematode *Caenorhabditis elegans*. *Neurobiology of Disease* **40**, 4-11, doi:10.1016/j.nbd.2010.05.012 (2010).
- 17 Wolozin, B., Gabel, C., Ferree, A., Guillily, M. & Ebata, A. in *Animal Models of Human Disease* Vol. 100 *Progress in Molecular Biology and Translational Science* 499-514 (2011).
- 18 Harrington, A. J., Hamamichi, S., Caldwell, G. A. & Caldwell, K. A. C. elegans as a Model Organism to Investigate Molecular Pathways Involved with Parkinson's Disease. *Developmental Dynamics* **239**, 1282-1295, doi:10.1002/dvdy.22231 (2010).

- 19 Bates, G. P. History of genetic disease - The molecular genetics of Huntington disease - a history. *Nature Reviews Genetics* **6**, 766-773, doi:10.1038/nrg1686 (2005).
- 20 White, J. G., Southgate, E., Thomson, J. N. & Brenner, S. The Structure of the Nervous-System of the Nematode *Caenorhabditis-Elegans*. *Philosophical Transactions of the Royal Society of London Series B-Biological Sciences* **314**, 1-340 (1986).
- 21 Chalfie, M., Tu, Y., Euskirchen, G., Ward, W. W. & Prasher, D. C. Green Fluorescent Protein as a Marker for Gene-Expression. *Science* **263**, 802-805 (1994).
- 22 Whitesides, G. M. The origins and the future of microfluidics. *Nature* **442**, 368-373, doi:10.1038/nature05058 (2006).
- 23 Beebe, D. J., Mensing, G. A. & Walker, G. M. Physics and applications of microfluidics in biology. *Annual Review of Biomedical Engineering* **4**, 261-286, doi:10.1146/annurev.bioeng.4.112601.125916 (2002).
- 24 Squires, T. M. & Quake, S. R. Microfluidics: Fluid physics at the nanoliter scale. *Reviews of Modern Physics* **77**, 977-1026 (2005).
- 25 Lucchetta, E. M., Lee, J. H., Fu, L. A., Patel, N. H. & Ismagilov, R. F. Dynamics of *Drosophila* embryonic patterning network perturbed in space and time using microfluidics. *Nature* **434**, 1134-1138, doi:10.1038/nature03509 (2005).
- 26 Chung, K., Cho, J. K., Park, E. S., Breedveld, V. & Lu, H. Three-Dimensional in Situ Temperature Measurement in Microsystems Using Brownian Motion of Nanoparticles. *Analytical Chemistry* **81**, 991-999, doi:10.1021/ac802031j (2009).
- 27 Bruin, G. J. M. Recent developments in electrokinetically driven analysis on microfabricated devices. *Electrophoresis* **21**, 3931-3951, doi:10.1002/1522-2683(200012)21:18<3931::aid-elps3931>3.0.co;2-m (2000).
- 28 Karnik, R. *et al.* Electrostatic control of ions and molecules in nanofluidic transistors. *Nano Letters* **5**, 943-948, doi:10.1021/nl050493b (2005).
- 29 Krajniak, J. & Lu, H. Long-term high-resolution imaging and culture of *C. elegans* in chip-gel hybrid microfluidic device for developmental studies. *Lab on a Chip* **10**, 1862-1868, doi:10.1039/c001986k (2010).
- 30 Cheng, S. & Wu, Z. G. Microfluidic electronics. *Lab on a Chip* **12**, 2782-2791, doi:10.1039/c2lc21176a (2012).
- 31 Teh, S. Y., Lin, R., Hung, L. H. & Lee, A. P. Droplet microfluidics. *Lab on a Chip* **8**, 198-220, doi:10.1039/b715524g (2008).
- 32 Chung, K. H., Crane, M. M. & Lu, H. Automated on-chip rapid microscopy, phenotyping and sorting of *C. elegans*. *Nature Methods* **5**, 637-643, doi:10.1038/nmeth.1227 (2008).
- 33 Stirman, J. N., Brauner, M., Gottschalk, A. & Lu, H. High-throughput study of synaptic transmission at the neuromuscular junction enabled by optogenetics and microfluidics. *Journal of Neuroscience Methods* **191**, 90-93, doi:10.1016/j.jneumeth.2010.05.019 (2010).
- 34 Crane, M. M. *et al.* Autonomous screening of *C-elegans* identifies genes implicated in synaptogenesis. *Nature Methods* **9**, 977-+ (2012).

- 35 Unger, M. A., Chou, H. P., Thorsen, T., Scherer, A. & Quake, S. R. Monolithic microfabricated valves and pumps by multilayer soft lithography. *Science* **288**, 113-116 (2000).
- 36 Duffy, D. C., McDonald, J. C., Schueller, O. J. A. & Whitesides, G. M. Rapid prototyping of microfluidic systems in poly(dimethylsiloxane). *Analytical Chemistry* **70**, 4974-4984 (1998).
- 37 Thorsen, T., Maerkl, S. J. & Quake, S. R. Microfluidic large-scale integration. *Science* **298**, 580-584 (2002).
- 38 Whitesides, G. M., Ostuni, E., Takayama, S., Jiang, X. Y. & Ingber, D. E. Soft lithography in biology and biochemistry. *Annual Review of Biomedical Engineering* **3**, 335-373 (2001).
- 39 Chung, K., Crane, M. M. & Lu, H. Automated on-chip rapid microscopy, phenotyping and sorting of *C. elegans*. *Nat Methods* **5**, 637-643, doi:nmeth.1227 [pii] 10.1038/nmeth.1227 [doi] (2008).
- 40 Lee, H., Crane, M. M., Zhang, Y. & Lu, H. Quantitative screening of genes regulating tryptophan hydroxylase transcription in *Caenorhabditis elegans* using microfluidics and an adaptive algorithm. *Integrative Biology* **5**, 372-380, doi:10.1039/c2ib20078c (2013).
- 41 Samara, C. *et al.* Large-scale in vivo femtosecond laser neurosurgery screen reveals small-molecule enhancer of regeneration. *Proceedings of the National Academy of Sciences of the United States of America* **107**, 18342-18347, doi:10.1073/pnas.1005372107 (2010).
- 42 Crane, M. M., Chung, K. & Lu, H. Computer-enhanced high-throughput genetic screens of *C. elegans* in a microfluidic system. *Lab on a Chip* **9**, 38-40, doi:10.1039/b813730g (2009).
- 43 Crane, M. M., Chung, K., Stirman, J. & Lu, H. Microfluidics-enabled phenotyping, imaging, and screening of multicellular organisms. *Lab on a Chip* **10**, 1509-1517, doi:10.1039/b927258e (2010).
- 44 Ben-Yakar, A., Chronis, N. & Lu, H. Microfluidics for the analysis of behavior, nerve regeneration, and neural cell biology in *C. elegans*. *Current Opinion in Neurobiology* **19**, 561-567, doi:10.1016/j.conb.2009.10.010 (2009).
- 45 Zeng, F., Rohde, C. B. & Yanik, M. F. Sub-cellular precision on-chip small-animal immobilization, multi-photon imaging and femtosecond-laser manipulation. *Lab on a Chip* **8**, 653-656, doi:10.1039/b804808h (2008).
- 46 Chung, K. & Lu, H. Automated high-throughput cell microsurgery on-chip. *Lab on a Chip* **9**, 2764-2766 (2009).
- 47 Allen, P. B. *et al.* Single-synapse ablation and long-term imaging in live *C. elegans*. *Journal of Neuroscience Methods* **173**, 20-26, doi:10.1016/j.jneumeth.2008.05.007 (2008).
- 48 Krajniak, J., Hao, Y., Mak, H. Y. & Lu, H. C.L.I.P.-continuous live imaging platform for direct observation of *C. elegans* physiological processes. *Lab on a Chip* **13**, 2963-2971, doi:10.1039/c3lc50300c (2013).
- 49 Chronis, N., Zimmer, M. & Bargmann, C. I. Microfluidics for in vivo imaging of neuronal and behavioral activity in *Caenorhabditis elegans*. *Nature Methods* **4**, 727-731 (2007).

- 50 Gray, J. M. *et al.* Oxygen sensation and social feeding mediated by a C-elegans guanylate cyclase homologue. *Nature* **430**, 317-322 (2004).
- 51 Zhang, Y., Lu, H. & Bargmann, C. I. Pathogenic bacteria induce aversive olfactory learning in *Caenorhabditis elegans*. *Nature* **438**, 179-184 (2005).
- 52 Lockery, S. R. *et al.* Artificial dirt: Microfluidic substrates for nematode neurobiology and behavior. *Journal of Neurophysiology* **99**, 3136-3143 (2008).
- 53 Park, S. *et al.* Enhanced *Caenorhabditis elegans* Locomotion in a Structured Microfluidic Environment. *Plos One* **3**, doi:e2550
10.1371/journal.pone.0002550 (2008).
- 54 Zimmer, M. *et al.* Neurons Detect Increases and Decreases in Oxygen Levels Using Distinct Guanylate Cyclases. *Neuron* **61**, 865-879 (2009).
- 55 Chokshi, T. V., Ben-Yakar, A. & Chronis, N. CO₂ and compressive immobilization of *C. elegans* on-chip. *Lab on a Chip* **9**, 151-157, doi:10.1039/b807345g (2009).
- 56 Hulme, S. E., Shevkopyas, S. S., Apfeld, J., Fontana, W. & Whitesides, G. M. A microfabricated array of clamps for immobilizing and imaging *C-elegans*. *Lab on a Chip* **7**, 1515-1523 (2007).
- 57 Hulme, S. E. *et al.* Lifespan-on-a-chip: microfluidic chambers for performing lifelong observation of *C. elegans*. *Lab on a Chip* **10**, 589-597 (2010).
- 58 Ben-Yakar, A. & Bourgeois, F. Ultrafast laser nanosurgery in microfluidics for genome-wide screenings. *Current Opinion in Biotechnology* **20**, 100-105, doi:10.1016/j.copbio.2009.01.008 (2009).
- 59 Smeulders, A. W. M., Worring, M., Santini, S., Gupta, A. & Jain, R. Content-based image retrieval at the end of the early years. *Ieee Transactions on Pattern Analysis and Machine Intelligence* **22**, 1349-1380 (2000).
- 60 Peng, H. C. Bioimage informatics: a new area of engineering biology. *Bioinformatics* **24**, 1827-1836, doi:10.1093/bioinformatics/btn346 (2008).
- 61 Jones, T. R. *et al.* Scoring diverse cellular morphologies in image-based screens with iterative feedback and machine learning. *Proceedings of the National Academy of Sciences of the United States of America* **106**, 1826-1831, doi:10.1073/pnas.0808843106 (2009).
- 62 Livet, J. *et al.* Transgenic strategies for combinatorial expression of fluorescent proteins in the nervous system. *Nature* **450**, 56+ (2007).
- 63 Betzig, E. *et al.* Imaging intracellular fluorescent proteins at nanometer resolution. *Science* **313**, 1642-1645 (2006).
- 64 Chung, K. & Deisseroth, K. CLARITY for mapping the nervous system. *Nature Methods* **10**, 508-513 (2013).
- 65 Sajda, P. Machine learning for detection and diagnosis of disease. *Annual Review of Biomedical Engineering* **8**, 537-565, doi:10.1146/annurev.bioeng.8.061505.095802 (2006).
- 66 Magoulas, G. & Prentza, A. in *Machine Learning and Its Applications* 300-307 (2001).
- 67 Kloppel, S. *et al.* Automatic classification of MR scans in Alzheimers disease. *Brain* **131**, 681-689 (2008).
- 68 Liu, T. M., Nie, J. X., Li, G., Gu, L. & Wong, S. T. C. in *2007 Ieee/Nih Life Science Systems and Applications Workshop* 59-62 (2007).

- 69 Liu, T. M., Nie, J. X., Li, G., Guo, L. & Wong, S. T. C. ZFIQ: a software package for zebrafish biology. *Bioinformatics* **24**, 438-439 (2008).
- 70 Bao, Z. R. *et al.* Automated cell lineage tracing in *Caenorhabditis elegans*. *Proceedings of the National Academy of Sciences of the United States of America* **103**, 2707-2712 (2006).
- 71 Carpenter, A. E. *et al.* CellProfiler: image analysis software for identifying and quantifying cell phenotypes. *Genome Biol.* **7** (2006).
- 72 Sieracki, M. E., Reichenbach, S. E. & Webb, K. L. Evaluation of Automated Threshold Selection Methods for Accurately Sizing Microscopic Fluorescent Cells by Image-Analysis. *Applied and Environmental Microbiology* **55**, 2762-2772 (1989).
- 73 Russ, J. C. & Russ, J. C. Automatic Discrimination of Features in Gray-Scale Images. *Journal of Microscopy-Oxford* **148**, 263-277 (1987).
- 74 Bhanu, B. Automatic Target Recognition - State-of-the-Art Survey. *Ieee Transactions on Aerospace and Electronic Systems* **22**, 364-379 (1986).
- 75 Trier, O. D. & Jain, A. K. Goal-Directed Evaluation of Binarization Methods. *Ieee Transactions on Pattern Analysis and Machine Intelligence* **17**, 1191-1201 (1995).
- 76 Kamel, M. & Zhao, A. Extraction of Binary Character Graphics Images from Grayscale Document Images. *Cvgip-Graphical Models and Image Processing* **55**, 203-217 (1993).
- 77 Sezgin, M. & Sankur, B. Survey over image thresholding techniques and quantitative performance evaluation. *Journal of Electronic Imaging* **13**, 146-168 (2004).
- 78 Abak, A. T., Baris, U. & Sankur, B. in *Proceedings of the Fourth International Conference on Document Analysis and Recognition, Vols 1 and 2* 697-700 (1997).
- 79 A Threshold Selection Method from Gray-Level Histograms. *Systems, Man and Cybernetics, IEEE Transactions on* **9**, 62-66, doi:10.1109/tsmc.1979.4310076 (1979).
- 80 Sauvola, J., Seppanen, T., Haapakoski, S. & Pietikainen, M. in *Proceedings of the Fourth International Conference on Document Analysis and Recognition, Vols 1 and 2* 147-152 (1997).
- 81 Niblack, W. *An Introduction to Image Processing*. (Prentice-Hall, 1986).
- 82 Wolf, C., Jolion, J. M. & Chassaing, F. in *16th International Conference on Pattern Recognition, Vol Ii, Proceedings International Conference on Pattern Recognition* 1037-1040 (2002).
- 83 Dougherty, E. R. & Lotufo, R. A. *Hands-on Morphological Image Processing*. (SPIE Press, 2003).
- 84 Rittner, R. A. L. L., Audigier, R., Machado, R. C. & Saúde, A. V. in *Biomedical Image Processing Biological and Medical Physics, Biomedical Engineering* (ed Thomas Martin Deserno) Ch. 4, 107-129 (Springer Berlin Heidelberg, 2011).
- 85 Stirman, J. N. *et al.* Real-time multimodal optical control of neurons and muscles in freely behaving *Caenorhabditis elegans*. *Nat Meth* **8**, 153-158, doi:http://www.nature.com/nmeth/journal/v8/n2/abs/nmeth.1555.html#supplementary-information (2011).

- 86 Chung, K. *et al.* Microfluidic chamber arrays for whole-organism behavior-based chemical screening. *Lab on a Chip* **11**, 3689-3697, doi:10.1039/c1lc20400a (2011).
- 87 Buckingham, S. D. & Sattelle, D. B. Fast, automated measurement of nematode swimming (thrashing) without morphometry. *Bmc Neuroscience* **10** (2009).
- 88 Sleight, J. N. *et al.* A novel *Caenorhabditis elegans* allele, *smn-1(cb131)*, mimicking a mild form of spinal muscular atrophy, provides a convenient drug screening platform highlighting new and pre-approved compounds. *Human Molecular Genetics* **20**, 245-260 (2011).
- 89 Husson, S. J., Costa¹, W. S., Schmitt, C. & Gottschalk, A. in *WormBook* (ed The *C. elegans* Research Community) (WormBook).
- 90 Leifer, A. M., Fang-Yen, C., Gershow, M., Alkema, M. J. & Samuel, A. D. T. Optogenetic manipulation of neural activity in freely moving *Caenorhabditis elegans*. *Nat Meth* **8**, 147-152, doi:http://www.nature.com/nmeth/journal/v8/n2/abs/nmeth.1554.html#supplementary-information (2011).
- 91 Rohde, C. B., Zeng, F., Gonzalez-Rubio, R., Angel, M. & Yanik, M. F. Microfluidic system for on-chip high-throughput whole-animal sorting and screening at subcellular resolution. *Proceedings of the National Academy of Sciences of the United States of America* **104**, 13891-13895 (2007).
- 92 Altun, Z. F. & Hall, D. H. *Handbook of C. elegans Anatomy*. In *WormAtlas*, <http://www.wormatlas.org/hermaphrodite/hermaphroditehomepage.htm> (2008).
- 93 Hobert, O. in *WormBook* (ed The *C. elegans* Research Community) (WormBook).
- 94 Chokshi, T. V., Bazopoulou, D. & Chronis, N. An automated microfluidic platform for calcium imaging of chemosensory neurons in *Caenorhabditis elegans*. *Lab on a Chip* **10**, 2758-2763, doi:10.1039/c004658b (2010).
- 95 Huang, X., Cheng, H. J., Tessier-Lavigne, M. & Jin, Y. S. MAX-1, a novel PH/MyTH4/FERM domain cytoplasmic protein implicated in netrin-mediated axon repulsion. *Neuron* **34**, 563-576 (2002).
- 96 Brenner, S. GENETICS OF CAENORHABDITIS-ELEGANS. *Genetics* **77**, 71-94 (1974).
- 97 Shaham (ed.), S. in *WormBook* (ed The *C. elegans* Research Community) (WormBook).
- 98 Shaham, S. Counting Mutagenized Genomes and Optimizing Genetic Screens in *Caenorhabditis elegans*. *PLoS One* **2** (2007).
- 99 Sleight, J. N. & Sattelle, D. B. C. ELEGANS MODELS OF NEUROMUSCULAR DISEASES EXPEDITE TRANSLATIONAL RESEARCH. *Translational Neuroscience* **1**, 214-227, doi:10.2478/v10134-010-0032-9 (2010).
- 100 Donohue, D. E. & Ascoli, G. A. Automated reconstruction of neuronal morphology: An overview. *Brain Research Reviews* **67**, 94-102, doi:http://dx.doi.org/10.1016/j.brainresrev.2010.11.003 (2011).
- 101 Gennarelli, M. *et al.* Survival Motor-Neuron Gene Transcript Analysis in Muscles from Spinal Muscular-Atrophy Patients. *Biochemical and Biophysical Research Communications* **213**, 342-348 (1995).

- 102 Lefebvre, S. *et al.* Identification and Characterization of a Spinal Muscular
Atrophy-Determining Gene. *Cell* **80**, 155-165 (1995).
- 103 Consortium, T. C. e. S. Genome Sequence of the Nematode *C. elegans*: A
Platform for Investigating Biology. *Science* **282**, 2012-2018,
doi:10.1126/science.282.5396.2012 (1998).
- 104 Yang, Y., Coleman, M., Zhang, L., Zheng, X. & Yue, Z. Autophagy in axonal and
dendritic degeneration. *Trends in Neurosciences* **36**, 418-428,
doi:http://dx.doi.org/10.1016/j.tins.2013.04.001 (2013).
- 105 Lefebvre, S. *et al.* Correlation between severity and SMN protein level in spinal
muscular atrophy. *Nature Genetics* **16**, 265-269 (1997).
- 106 Dimitriadi, M. *et al.* Conserved Genes Act as Modifiers of Invertebrate SMN
Loss of Function Defects. *Plos Genetics* **6** (2010).
- 107 Oprea, G. E. *et al.* Platin 3 is a protective modifier of autosomal recessive spinal
muscular atrophy. *Science* **320**, 524-527 (2008).
- 108 Monani, U. R. *et al.* A single nucleotide difference that alters splicing patterns
distinguishes the SMA gene SMN1 from the copy gene SMN2. *Human Molecular
Genetics* **8**, 1177-1183 (1999).
- 109 Pulak, R. in *Methods in Molecular Biology* Vol. 351 *Methods in Molecular
Biology* 275-286 (2006).
- 110 Briese, M. *et al.* Deletion of *smn-1*, the *Caenorhabditis elegans* ortholog of the
spinal muscular atrophy gene, results in locomotor dysfunction and reduced
lifespan. *Human Molecular Genetics* **18**, 97-104, doi:10.1093/hmg/ddn320
(2009).
- 111 Caceres, I. D., Valmas, N., Hilliard, M. A. & Lu, H. Laterally Orienting *C.*
elegans Using Geometry at Microscale for High-Throughput Visual Screens in
Neurodegeneration and Neuronal Development Studies. *Plos One* **7**,
doi:10.1371/journal.pone.0035037 (2012).
- 112 Xia, Y. N. & Whitesides, G. M. Soft lithography. *Annual Review of Materials
Science* **28**, 153-184 (1998).
- 113 Edelstein, A., Amodaj, N., Hoover, K., Vale, R. & Stuurman, N. - Computer
Control of Microscopes Using μ Manager. (2010).
- 114 Teschendorf, D. & Link, C. D. What have worm models told us about the
mechanisms of neuronal dysfunction in human neurodegenerative diseases?
Molecular Neurodegeneration **4**, doi:10.1186/1750-1326-4-38 (2009).
- 115 Cong, G. & Parvin, B. Model-based segmentation of nuclei. *Pattern Recognition*
33, 1383-1393 (2000).
- 116 Li, G. *et al.* 3D cell nuclei segmentation based on gradient flow tracking. *Bmc
Cell Biology* **8** (2007).
- 117 Branson, K., Robie, A. A., Bender, J., Perona, P. & Dickinson, M. H. High-
throughput ethomics in large groups of *Drosophila*. *Nature Methods* **6**, 451-U477,
doi:10.1038/nmeth.1328 (2009).
- 118 Dankert, H., Wang, L. M., Hoopfer, E. D., Anderson, D. J. & Perona, P.
Automated monitoring and analysis of social behavior in *Drosophila*. *Nature
Methods* **6**, 297-303, doi:10.1038/nmeth.1310 (2009).
- 119 Clarke, L. P. *et al.* Mri Segmentation - Methods and Applications. *Magnetic
Resonance Imaging* **13**, 343-368 (1995).

- 120 Dehmelt, L., Poplawski, G., Hwang, E. & Halpain, S. NeuriteQuant: An open source toolkit for high content screens of neuronal Morphogenesis. *Bmc Neuroscience* **12** (2011).
- 121 Matheron, G. *Random sets and integral geometry*. 1-288 (Wiley, 1975).
- 122 Jones, K. T. & Ashrafi, K. Caenorhabditis elegans as an emerging model for studying the basic biology of obesity. *Disease Models & Mechanisms* **2**, 224-229, doi:10.1242/dmm.001933 (2009).
- 123 Ashrafi, K. in *WormBook* (ed The C. elegans Research Community) (WormBook).
- 124 Zhang, S. O. *et al.* Genetic and dietary regulation of lipid droplet expansion in Caenorhabditis elegans. *Proceedings of the National Academy of Sciences* **107**, 4640-4645, doi:10.1073/pnas.0912308107 (2010).
- 125 Klemm, Robin W. *et al.* A Conserved Role for Atlantin GTPases in Regulating Lipid Droplet Size. *Cell Reports* **3**, 1465-1475 (2013).
- 126 Elle, I. C., Olsen, L. C. B., Pultz, D., Rødkær, S. V. & Færgeman, N. J. Something worth dyeing for: Molecular tools for the dissection of lipid metabolism in Caenorhabditis elegans. *FEBS Letters* **584**, 2183-2193, doi:10.1016/j.febslet.2010.03.046 (2010).
- 127 Kinkel, A. D. *et al.* Oil red-O stains non-adipogenic cells: a precautionary note. *Cytotechnology* **46**, 49-56, doi:10.1007/s10616-004-3903-4 (2004).
- 128 Serra, J. *Image analysis and mathematical morphology.*, 318-372 (Academic Press Ltd, 1982).
- 129 Robin W. Klemm, J. P. N., Ronald A. Cole, Chen S. Li, Seong H. Park, Matthew M. Crane, Liying Li, Diana Jin, Alexandra Boye-Doe, Tina Y. Liu, Yoko Shibata, Hang Lu, Tom A. Rapoport, Robert V. Farese, Craig Blackstone, Yi Guo, Ho Yi Mak. A Conserved Role for Atlantin GTPases in Regulating Lipid Droplet Size. *Cell Reports* **3**, 1465 - 1475 (2013).
- 130 *WormBase web site.* , <<http://www.wormbase.org>> (2013).
- 131 Wolozin, B., Gabel, C., Ferree, A., Guillily, M. & Ebata, A. Watching Worms Whither: Modeling Neurodegeneration in C. elegans. *Animal Models of Human Disease* **100**, 499-514, doi:10.1016/b978-0-12-384878-9.00015-7 (2011).
- 132 van Ham, T. J., Breitling, R., Swertz, M. A. & Nollen, E. A. A. Neurodegenerative diseases: Lessons from genome-wide screens in small model organisms. *Embo Molecular Medicine* **1**, 360-370, doi:10.1002/emmm.200900051 (2009).
- 133 Bargmann, C. I. in *C. Elegans II* (eds Donald L. Riddle, Thomas Blumenthal, Barbara J. Meyer, & James R. Priess) Ch. 25, 717-738 (Cold Spring Harbor Laboratory Press, 1997).
- 134 Bargmann, C. I. in *WormBook* (ed The C. elegans Research Community) (WormBook, 2006).
- 135 Dupuy, D. *et al.* Genome-scale analysis of in vivo spatiotemporal promoter activity in Caenorhabditis elegans. *Nature Biotechnology* **25**, 663-668 (2007).
- 136 Zhang, Y. *et al.* A novel tracing algorithm for high throughput imaging - Screening of neuron-based assays. *Journal of Neuroscience Methods* **160**, 149-162, doi:10.1016/j.jneumeth.2006.07.028 (2007).

- 137 Can, A., Hong, S., Turner, J. N., Tanenbaum, H. L. & Roysam, B. Rapid automated tracing and feature extraction from retinal fundus images using direct exploratory algorithms. *Information Technology in Biomedicine, IEEE Transactions on* **3**, 125-138, doi:10.1109/4233.767088 (1999).
- 138 Xiao, L., Yuan, X., Galbreath, Z. & Roysam, B. in *Life System Modeling and Intelligent Computing* Vol. 6330 *Lecture Notes in Computer Science* (eds Kang Li *et al.*) Ch. 13, 100-112 (Springer Berlin Heidelberg, 2010).
- 139 Xie, J., Zhao, T., Lee, T. M., Myers, E. & Peng, H. C. Automatic Neuron Tracing in Volumetric Microscopy Images with Anisotropic Path Searching. *Medical Image Computing and Computer-Assisted Intervention - Miccai 2010, Pt Ii* **6362**, 472-479 (2010).
- 140 Peng, H. C., Long, F. H. & Myers, G. Automatic 3D neuron tracing using all-path pruning. *Bioinformatics* **27**, I239-I247, doi:10.1093/bioinformatics/btr237 (2011).
- 141 Al-Kofahi, K. A. *et al.* Rapid automated three-dimensional tracing of neurons from confocal image stacks. *Ieee Transactions on Information Technology in Biomedicine* **6**, 171-187, doi:10.1109/titb.2002.1006304 (2002).
- 142 Hilliard, M. A. Axonal degeneration and regeneration: a mechanistic tug-of-war. *Journal of Neurochemistry* **108**, 23-32 (2009).
- 143 Perona, P. & Malik, J. Scale-Space and Edge-Detection Using Anisotropic Diffusion. *Ieee Transactions on Pattern Analysis and Machine Intelligence* **12**, 629-639 (1990).
- 144 Otsu, N. Threshold Selection Method from Gray-Level Histograms. *IEEE Trans. Syst. Man Cybern.* **9**, 62-66 (1979).
- 145 Shah, N. R. & Braverman, E. R. Measuring Adiposity in Patients: The Utility of Body Mass Index (BMI), Percent Body Fat, and Leptin. *PLoS ONE* **7**, e33308, doi:10.1371/journal.pone.0033308 (2012).
- 146 Flegal, K. M., Carroll, M. D., Ogden, C. L. & Curtin, L. R. Prevalence and Trends in Obesity Among US Adults, 1999-2008. *JAMA: The Journal of the American Medical Association* **303**, 235-241, doi:10.1001/jama.2009.2014 (2010).
- 147 Farooqi, I. S. & O'Rahilly, S. Genetic factors in human obesity. *Obesity Reviews* **8**, 37-40, doi:10.1111/j.1467-789X.2007.00315.x (2007).
- 148 Capowski, J. J. *Computer Techniques in Neuroanatomy*. (Springer US, 1989).